PHOTOPRODUCTION OF NEUTRAL KAONS ON DEUTERIUM

A dissertation submitted to

Kent State University in partial

fulfillment of the requirements for the

degree of Doctor of Philosophy

by

Kabi R. Bantawa

December, 2009

Dissertation written by

Kabi R. Bantawa

M. Sc. Tribhuvan University, Nepal, 1992

Ph. D. Kent State University, 2009

Approved by

Dr. D. Mark Manley	Chair, Doctoral Dissertation Committee
Dr. Spiros Margetis	Member, Doctoral Dissertation Committee
Dr. Elizabeth Mann	Member, Doctoral Dissertation Committee
Dr. Alexander Seed	Member, Doctoral Dissertation Committee
Dr. Michael Tubergen	Member, Doctoral Dissertation Committee

Accepted by

Dr. Bryan Anderson	Chair, Department of Physics
Dr. John R. D. Stalvey	Dean, College of Arts and Sciences

Table of Contents

List of Figures viii

List of Tables xix

Acknowledgements xxi

1 **Introduction** 1

1.1 Quark model 1

1.1.1 Mesons in the quark model 3

1.1.2 Neutral kaons 4

1.1.3 CP-Violation in neutral kaons 6

1.1.4 Baryons in the quark model 7

1.2 Quantum Chromodynamics (QCD) 8

1.3 Nucleon resonances 9

1.4 Physics motivation 13

1.5 Outline of Current Work 13

2 **Theory, Kinematics, and Previous Experiments** 15

2.1 Kaon photoproduction process 15

2.1.1 Kinematics 17

2.1.2 Kaon center-of-mass angle ($\Theta_{\mathrm{CM}}^{K^0}$) 20

2.2 Theory of kaon photoproduction 21

2.2.1 Kaon-MAID model 22

2.2.2 SLA model 23

2.3 Previous experiments 25

2.3.1 ^{12}C target . . . 25
2.3.2 Liquid deuterium target . . . 27

3 **Experimental Setup** . . . 30
3.1 Mainz Microtron (MAMI) . . . 31
3.2 The Glasgow Photon Tagger . . . 33
3.3 The Crystal Ball . . . 37
3.4 Particle Identification Detector (PID) . . . 39
3.5 Multiwire proportional chambers (MWPCs) . . . 42
3.6 The TAPS detector . . . 42
3.7 The target system . . . 46
3.8 Electronics . . . 48
3.8.1 Tagger electronics . . . 48
3.8.2 CB electronics . . . 49
3.8.3 TAPS electronics . . . 49
3.8.4 Event triggering . . . 52
3.9 Overview of data taking . . . 54

4 **Data Analysis** . . . 55
4.1 Analysis software (AcquRoot) . . . 55
4.2 Energy calibration process . . . 57
4.2.1 Tagger energy calibration . . . 57
4.2.2 TAPS energy calibration . . . 57
4.2.3 Crystal ball energy calibration . . . 58
4.3 TAPS particle identification . . . 59
4.4 Tagger random subtraction . . . 59
4.5 Cluster algorithm . . . 63

4.6 Kinematic fit . . . 66
4.6.1 Introduction . . . 66
4.6.2 The pull function . . . 68
4.6.3 Confidence level (CL) . . . 69
4.6.4 Number of degrees of freedom (NDF) . . . 73
4.7 Event selection . . . 74
4.7.1 Particle identification in $\gamma n \to K^0_S \Lambda \to (\pi^0\pi^0)(\pi^0 n) \to 6\gamma n$ . . . 75
4.7.2 Identification of K^0_S and Λ . . . 75
4.7.3 Identification of a neutron by missing mass . . . 78
4.7.4 Best pion combination of the four photons from K^0_S . . . 79
4.8 Monte Carlo simulation . . . 80
4.9 Estimation of background . . . 82
4.9.1 Background from $\gamma p \to K^0\Sigma^+$ . . . 83
4.9.2 Background from $\gamma n \to K^0\Sigma^0$ . . . 85
4.9.3 Background from $\gamma N \to \eta N$ . . . 86
4.9.4 Background from $\gamma N \to 3\pi^0 N$ . . . 86
4.10 Some methods for background subtraction . . . 87
4.10.1 Selection of the highest probability among all reaction channels . . . 87
4.10.2 Final background subtraction method . . . 87
4.11 Secondary vertex and decay correction for K^0_S and Λ . . . 88
4.12 Acceptance and efficiency determination . . . 89
4.13 Photon flux determination . . . 92
4.14 Empty target background subtraction . . . 95

5 **Result and Discussions** . . . 98
5.1 Calculation of differential cross section . . . 98
5.1.1 Legendre polynomial fitting . . . 100

5.2 Background subtractions . . . 101
5.3 Differential cross section for $\gamma n \to K^0\Lambda$ . . . 103
5.3.1 Comparison with model predictions . . . 103
5.3.2 Legendre fitting coefficients . . . 107
5.4 Total cross section for $\gamma n \to K^0\Lambda$ . . . 108
5.5 Uncertainties in $d\sigma/d\Omega$ . . . 111

6 **Summary and Conclusions** . . . 114

Bibliography . . . 118

A **Analysis of $\gamma p \to K^0\Sigma^+$** . . . 121
A.1 Tagger random subtraction . . . 121
A.2 Confidence level and the number of degrees of freedom (NDF) . . . 121
A.3 Event selection . . . 124
A.4 Background subtraction . . . 126
A.5 Secondary vertex and decay correction for K^0_S and Σ^+ . . . 131
A.6 Acceptance and efficiency determination . . . 132
A.7 Result of background subtraction . . . 136
A.8 The differential cross section for $\gamma p \to K^0\Sigma^+$ . . . 137
A.8.1 Comparison with prior results . . . 141
A.8.2 Legendre fitting coefficients . . . 141
A.8.3 Total cross section for $\gamma p \to K^0\Sigma^+$ . . . 143

B **Tables of $d\sigma/d\Omega$ and $\sigma_{\rm tot}$ for $\gamma p \to K^0\Sigma^+$** . . . 148

C **Tables of $d\sigma/d\Omega$ and $\sigma_{\rm tot}$ for $\gamma n \to K^0\Lambda$** . . . 153

D **Legendre fitting coefficients for $\gamma p \to K^0\Sigma^+$** . . . 159

E **Legendre fitting coefficients for $\gamma n \to K^0\Lambda$** 161

F **Background contributions to $\sigma_{\rm tot}(\gamma p \to K^0\Sigma^+)$** 163

G **Background contributions to $\sigma_{\rm tot}(\gamma n \to K^0\Lambda)$** 164

List of Figures

1.1 The members of the isospin doublets u and d quarks and the isospin singlet s quark can be used to form the two axes of the $SU(3)$ flavors. 3

1.2 Left: The pseudoscalar mesons with $J^P = 0^-$. Right: The vector mesons with $J^P = 1^-$. 4

1.3 Feynman diagram showing the conversion of K^0 and $\bar{K}^0$. 5

1.4 Left: The baryon octet with $J^P = \frac{1}{2}^+$. Right: The baryon decuplet with $J^P = \frac{3}{2}^+$. . 8

1.5 (a) The QED vertex showing the emission or the absorption of a photon (represented by a wavy line) by a charged particle. (b) The electromagnetic interaction between the charged particles e_1 and e_2 with the exchange of a photon (c) The QCD vertex showing the emission or absorption of a gluon (represented by a spiral line) by a quark. (d) The strong interaction between two quarks q_1 and q_2 with the exchange of a gluon. 10

1.6 By flipping a quark's spin, a proton is changed into a Δ^+ 11

2.1 Schematic representation of the reaction $\gamma n \to K^0\Lambda$ as detected in our experiment. 16

2.2 Representation of the reaction $\gamma n \to K^0\Lambda$ using branching ratios. The K^0 has equal probability to decay into K^0_S and K^0_L. Only the K^0_S was detected in our experiment. 17

2.3 Diagram to represent the neutral kaon photoproduction mechanism. 17

2.4 (a) The laboratory frame for K^0 photoproduction. (b) The center-of-mass frame for K^0 photoproduction. In both cases the direction of the incident beam is along the z-axis. 20

2.5 Feynman diagrams used in an isobar-model calculation of kaon photoproduction. The hadronic vertices are represented by (1), (2), (3) and the electromagnetic vertices by (a), (b), (c). In $\gamma n \to K^0\Lambda$, there is no contribution from the Δ resonance. The intermediate states N, Y, and K are associated with the Born terms and those N^*, Y^*, and K^* are associated with the resonance terms. The diagrams, from left to right, depict contributions from s-channel exchange, u-channel exchange, and t-channel exchange, respectively. Figure from Ref. [31]. 22

2.6 Theoretical results for the total cross section for the six channels of strangeness photoproduction for the Kaon-MAID model (solid lines shows the current and the dotted lines shows the older Kaon-MAID model as described in Ref. [31]). The solid squares represent the new SAPHIR data taken from Ref. [15], open circles represent the old data taken from Ref. [34], and the solid circles are the data from Ref. [35]. 24

2.7 The filled circles represent the total cross section for $^{12}\mathrm{C}(\gamma, K^0)$ and the open triangles represent that for $^{12}\mathrm{C}(\gamma, K^+)$. Figure from Ref. [37]. 26

2.8 Differential cross section for $\gamma n \to K^0\Lambda$. The Kaon-MAID model is shown by the dashed line and SLA model predictions for r_{KK_1} = -0.447, -1.5, -3.4 are represented by the dotted, solid, and dot-dashed lines, respectively. Figure from Ref. [19]. 27

2.9 The differential cross section for $\gamma n \to K^0\Lambda$ as predicted by Kaon-MAID [31] (solid line), SLA [28] (dotted line), PH1 (dashed line), and PH2 (dotted dashed line). 28

2.10 Comparison of the total cross section for $\gamma n \to K^0\Lambda$. The Kaon-MAID prediction [31] is represented by the solid line, SLA [28] by the dotted line, and the PH1 and PH2 predictions coincide with each other and are represented by the dashed dotted line. Figure from Ref. [36]. 29

3.1 The experimental set-up in the A2 Hall in Mainz consists of three main components: (i) MAMI electron accelerator for production of electrons up to 1.5 GeV, (ii) Glasgow Photon Tagger, (iii) Detector system (CB, TAPS, PID, MWPC). 30
3.2 The floor plan of MAMI facility. Three racetrack microtrons RTM1, RTM2, and RTM3 together with the Harmonic Double Sided Microtron (HDSM) produce an electron beam with energy up to 1508 MeV in MAMI-C. A1, A2, A4, and X1 are the experimental halls. Our experimental work was carried out in the A2 Hall. . . . 32
3.3 General layout of the HDSM. HDSM consists mainly of two pairs of 90° bending magnets and two linear accelerators. These two linear accelerators work on two different frequencies, 2.45 GHz and 4.90 GHz. Figure from Ref. [38] 33
3.4 The Glasgow Tagger. As soon as the high-energy electron beam strikes the surface of the radiator, photons are created by the bremsstrahlung process. The trajectory of the electrons is bent by a huge Tagger dipole magnet onto the focal-plane detectors and the photons are sent to the target. 36
3.5 An individual crystal in the CB is 40.6 cm long with a truncated pyramid shape. . . 38
3.6 A transverse view of the Crystal Ball showing the sub detectors inside it. A liquid deuterium target is also located at its center. 39
3.7 The two-dimensional Mercator-like projection of CB Crystals. It shows 90 shaded and unshaded groups of rectangles each containing eight crystals. It also shows the geometry of CB as there are 20 major triangles each of which is made of four minor triangles and each minor triangle contains nine crystals. The ‘beam in’ and ‘beam out’ hole is also visible. 40
3.8 The PID before inserting it into position within the CB. 41
3.9 The Multiwire Proportional Chamber before inserting it into its position within the CB. 42

3.10 Each individual TAPS BaF_2 detector consists of a hexagonally shaped crystal tube of 25 cm in length with a 2.5 cm cylindrical end connected directly to the photo-multiplier tube. 43

3.11 The use of TAPS as a forward wall detector at a distance 1.8 m from the CB. The 384 BaF_2 crystals of the TAPS forward wall cover the hole of the CB to cover $\sim$96% of 4π in solid angle. 44

3.12 A schematic plot of the pulse shape for an α-particle and a photon in TAPS. The larger long component make it possible to distinguish the α-particle and a photon. 45

3.13 Our deuterium target cell was 48 mm long and 40 mm in diameter. The target was surrounded by thin multi-layers made of Kapton and super insulation foils to prevent moisture build-up on the target window. 47

3.14 The complete liquid deuterium (LD_2) target system. It consists of a gas storage tank (of capacity 1000 liters), a deuterium gas compressor, a liquefier containing the reservoir for the LD_2, and the LD_2 supply line connecting the target cell with the reservoir. During the experiment, this target cell was inserted at the center of the CB. 47

3.15 Tagger electronics system. 50

3.16 The CB electronics system. 51

3.17 The TAPS electronics system. 52

3.18 Technical scheme of the trigger electronic system. 53

4.1 The tree structure of AcquRoot Analyzer with its Apparatus, Detector, Physics and Analysis classes. Figure from Ref. [47]. 56

4.2 A cosmic-ray energy spectrum in a TAPS module with a fit (exponential+Gaussian) showing the narrow pedestal peak at 0 MeV (near ADC channel 100) and the broad cosmic peak at 37.7 MeV (near ADC channel 275). Figure from Ref. [49]. 58

4.3 TAPS pulse-shape analysis for the identification of baryons and the electromagnetic particles. The energy deposited in the short gate ADC (fast component) and that deposited in the long gate ADC (total light output) are plotted against each other. . 60

4.4 A Tagger timing spectrum for all the tagger elements in the focal plane. A coincidence of the CB trigger and the Tagger time gives the prompt peak. The red shaded area (95-115 ns) indicates the prompt events. The region underneath it (PQRS) is the random background. 61

4.5 The Tagger-time alignment for the data acquisition period. 62

4.6 Tagger timing spectrum for channel 25 for which the calculated ratio of the random-prompt areas was $r_{\rm pr}$ = 0.492. 63

4.7 Example of random background subtraction of missing mass of K^0 for a typical channel 51 at photon energy E_γ= 1251.9 MeV. (a) The red-filled histogram corresponds to random background events and the green-filled histogram is for prompt coincident events. (b) The resulting histogram fitted with a Gaussian distribution after the subtraction of the two previous histograms using Eq. (4.2). 64

4.8 The cluster patterns mentioned in the cluster algorithm. (a) A NaI cluster for an ideal event in the CB with the central crystal red in color. The cluster-finding algorithm defines the crystal with the highest energy and surrounded by 12 nearest neighboring crystals as the central crystal in CB. (b) A TAPS cluster for an ideal event in TAPS with the central crystal red in color. The cluster-finding algorithm defines the crystal with the highest energy and surrounded by six nearest neighboring crystals as the central crystal in TAPS. 65

4.9 The pull distributions for (a) the energy E, (b) the angular variation θ, and (c) the angular variation ϕ of the incoming photon beam in the analysis of $\gamma n \rightarrow K^0\Lambda$ using kinematic fitting. When each distribution is fitted with a Gaussian function, the mean is close to zero with standard deviation σ close to one. 70

4.10 (a) Probability density of χ^2 for different numbers of degrees of freedom. The distribution for k = 1 is the curve at the far left and the curves move to the right as the value of k increases. (b) The cumulative distribution of χ^2 for different numbers of degrees of freedom. The curve for k = 1 is the one at the far left, and the curve for k = 5 is at the far right. 72

4.11 The confidence level distributions for Monte Carlo simulation (blue circles) and for real data (red triangles) in the reaction $\gamma n \rightarrow K^0\Lambda$. The vertical line shows a CL cut placed at 0.15 for the selection of good events. This cut reduces 33% misidentified events from the real data. 73

4.12 The z coordinate of the incident beam for Monte Carlo simulation (blue circles) and for real data (red triangles) in the reaction $\gamma n \rightarrow K^0\Lambda$. It is considered as the **primary vertex** in our analysis. 74

4.13 The invariant mass of 2γ for all combinations of two out of six photons in the final state for $\gamma n \rightarrow K^0_S\Lambda \rightarrow 3\pi^0 n \rightarrow 6\gamma n$. The invariant mass of 2γ gives a peak around the mass of π^0. 76

4.14 The distribution of invariant mass for the four photons identified as coming from $\gamma n \rightarrow K^0\Lambda$ followed by $K^0_S \rightarrow 2\pi^0 \rightarrow 4\gamma$. The peak is near the mass (497.6 MeV) of the neutral kaon. 77

4.15 The distribution of missing mass for the four photons clusters identified as coming from $\gamma n \rightarrow K^0\Lambda$ followed by $K^0_S \rightarrow 2\pi^0 \rightarrow 4\gamma$. The peak is near the mass (1115.7 MeV) of the Λ hyperon. 78

4.16 The distribution of missing mass of the six photons identified as coming from $\gamma n \rightarrow K^0_S\Lambda \rightarrow 3\pi^0 n \rightarrow 6\gamma n$. The peak is near the mass (939.6 MeV) of the neutron. . . 79

4.17 Two-dimensional plot of invariant masses of the reconstructed π^0 pairs from the decay of K^0 as $K^0 \rightarrow 2\pi^0 \rightarrow 4\gamma$ for $\gamma n \rightarrow K^0\Lambda$ events. 80

4.18 The distribution of invariant mass for the two photons identified as coming from $K^0_S \to 2\pi^0$ followed by $\pi^0 \to 2\gamma$. The peak is near the mass (135.0 MeV) of the neutral pion. 81

4.19 Geometry of the CB and TAPS in the Monte Carlo simulation. Figure from Ref. [46]. 83

4.20 (a) The distributions of the distance traveled by K^0_S before its decay for Monte Carlo simulation (blue dashed line) and for real data (red solid line). (b) The distribution of the lifetime of K^0_S for Monte Carlo simulation (blue dashed line) and for real data (red solid line). (c) The distribution of the distance traveled by Λ before its decay for Monte Carlo simulation (blue dashed line) and for real data (red solid line). (d) The distribution of the lifetime of Λ for Monte Carlo simulation (blue dashed line) and for real data (red solid line). 90

4.21 (a) The distribution of the lifetime for the K^0_S with fit values $(0.864 \pm 0.0320) \times 10^{-10}$ s and the PDG values [4], $(0.8958 \pm 0.0005) \times 10^{-10}$ s. (b) The distribution of the lifetime for the Λ with fit values $(2.865 \pm 0.046) \times 10^{-10}$ s and the PDG values [4], $(2.631 \pm 0.020) \times 10^{-10}$ s. 91

4.22 The acceptance for $\gamma n \to K^0\Lambda$ as a function of $\cos(\theta^{\rm CM}_{\rm K^0})$ for beam energies between 950 and 1400 MeV. 93

4.23 Detector efficiency for $\gamma n \to K^0\Lambda$ events as a function of incident photon energy. . 94

4.24 The tagging efficiency during our measurements. 95

4.25 The photon flux, which is related to the number of incident photons on the target. . 96

5.1 Angular distributions of contamination ratio $\varepsilon_{\rm MC}$ for the reaction $\gamma n \to K^0\Lambda$ at E_γ= 1250 MeV due to (a) $\gamma p \to K^0\Sigma^+$, (b) $\gamma n \to K^0\Sigma^0$, (c) $\gamma N \to \eta N$, and (d) $\gamma N \to 3\pi^0 N$. The angular distributions for other energy bins are similar. 102

5.2 Differential cross section in the center-of-mass system for the reaction $\gamma n \to K^0\Lambda$ at incident photon energies, E_γ, from 925 to 1375 MeV. The plots also show the corresponding center-of-mass energy W. The solid curves are from the Legendre polynomial fits to our data. 104
5.2 Continued. 105
5.2 Continued. 106
5.3 Comparison of our results (red filled circles) for the differential cross section of $\gamma n \to K^0\Lambda$ at $E_\gamma = 1100$ MeV with predictions of the Kaon-MAID model [31] (blue dashed curve) and the SLA model [26] (green dotted curve). The solid curve is the result of the Legendre polynomial fit to our data. 107
5.4 Legendre fitting coefficients for $d\sigma/d\Omega$ of the reaction $\gamma n \to K^0\Lambda$. 108
5.5 The total cross section for $\gamma n \to K^0\Lambda$ without subtraction of background (filled squares) and estimation of the total contribution of background stemming from the background reactions and the empty target (open crosses) as described in the text. . 109
5.6 The total cross section for $\gamma n \to K^0\Lambda$ after background subtractions as a function of center-of-mass energy W. The error bars shown are due only to counting statistics. 110
5.7 Comparison of our results (red filled circles) for $\sigma_{\rm tot}(\gamma n \to K^0\Lambda)$ after background subtraction with predictions of the Kaon-MAID model [31] (blue solid curve) and SLA model [26] (green dashed curve). 111

A.1 Tagger timing spectrum for channel 25 for which the calculated ratio of the random-prompt areas was $r_{\rm pr}$ = 0.516. 122
A.2 Example of random background subtraction of missing mass of K^0 for Tagger channel 34 and incident photon energy 1300.9 MeV. (a) The red-filled histogram corresponds to random background events and the green-filled histogram is for the prompt coincident events. (b) The resulting histogram fitted with a Gaussian distribution after the subtraction of the two previous histograms using Eq. (4.2). . . 122

A.3 Confidence level distributions for Monte Carlo simulation (blue circles) and for real data (red triangles) in the reaction $\gamma p \to K^0\Sigma^+$. The vertical line shows a CL cut placed at 0.15 for the selection of good events. This cut reduces 33% misidentified events from the real data. 123

A.4 The z coordinate of the incident beam for Monte Carlo simulation (blue circles) and for real data (red triangles) in the reaction $\gamma p \to K^0\Sigma^+$. It is considered as the **primary vertex** in our analysis. 124

A.5 The invariant mass distribution of 2γ for all combinations of two out of six photons in the final state for $\gamma p \to K^0_S\Sigma^+ \to 3\pi^0 p \to 6\gamma p$. 125

A.6 The distribution of invariant mass for the four photons identified as coming from $\gamma p \to K^0\Sigma^+$ followed by $K^0_S \to 2\pi^0 \to 4\gamma$. The peak is near the mass (497.6 MeV) of the neutral kaon. 126

A.7 The distribution of missing mass for the four photons identified as coming from $\gamma p \to K^0\Sigma^+$ followed by $K^0_S \to 2\pi^0 \to 4\gamma$. The peak is near the mass (1189 MeV) of the Σ^+ hyperon. 127

A.8 Two-dimensional plot of invariant masses of the reconstructed π^0 pairs from the decay of K^0_S as $K^0_S \to 2\pi^0 \to 4\gamma$ for $\gamma p \to K^0\Sigma^+$ events. 128

A.9 The distribution of invariant mass for the two photons identified as coming from $K^0_S \to 2\pi^0$ followed by $\pi^0 \to 2\gamma$. The peak is near the mass (135.0 MeV) of the neutral pion. 129

A.10 The distribution of missing mass of the six photons identified as coming from $\gamma p \to K^0_S\Sigma^+ \to 3\pi^0 p \to 6\gamma p$. The peak is near the mass (938.3 MeV) of the proton. . . 130

A.11 (a) The distributions of the distance traveled by K^0 before its decay for Monte Carlo simulation (blue dashed line) and for real data (red solid line). (b) The distribution of the lifetime of K^0_S for Monte Carlo simulation (blue dashed line) and for real data (red solid line). (c) The distribution of the distance traveled by Σ^+ before its decay for Monte Carlo simulation (blue dashed line) and for real data (red solid line). (d) The distribution of the lifetime of Σ^+ for Monte Carlo simulation (blue dashed line) and for real data (red solid line). 133

A.12 (a) The distribution of the lifetime for the K^0_S with fit values $(0.961 \pm 0.032) \times 10^{-10}$ s and the PDG values [4], $(0.895 \pm 0.0005) \times 10^{-10}$ s. (b) The distribution of the lifetime for the Σ^+ with fit values $(0.973 \pm 0.024) \times 10^{-10}$ s and the PDG values [4], $(0.8018 \pm 0.0026) \times 10^{-10}$ s. 134

A.13 The acceptance for $\gamma p \rightarrow K^0\Sigma^+$ as a function of $\cos(\theta^K_{\rm CM})$ at beam energies between 1100 and 1400 MeV. 135

A.14 Detector efficiency for $\gamma p \rightarrow K^0\Sigma^+$ events as a function of incident photon energy. 136

A.15 Angular distributions of contamination ratio $\varepsilon_{\rm MC}$ for the reaction $\gamma p \rightarrow K^0\Sigma^+$ at E_γ = 1200 MeV due to (a) $\gamma n \rightarrow K^0\Lambda$, (b) $\gamma n \rightarrow K^0\Sigma^0$, (c) $\gamma N \rightarrow \eta N$, and (d) $\gamma N \rightarrow 3\pi^0 N$. The angular distributions for other energy bins are similar. 137

A.16 Differential cross section in the center-of-mass system for the reaction $\gamma p \rightarrow K^0\Sigma^+$ at incident photon energies E_γ between 1050 and 1375 MeV. The solid curves are the results of the Legendre polynomial fits to our data. 139

A.16 Continued. 140

A.16 Continued. 141

A.17 Differential cross section for the reaction $\gamma p \to K^0\Sigma^+$ from this work (red solid circles) compared to measurements by CB-ELSA/TAPS [52] (green triangles) at incident photon energies of E_γ = 1100, 1200, and 1300 MeV. The solid curves are the results of Legendre polynomial fits to our data. Only statistical uncertainties are displayed. 142
A.18 Legendre coefficients obtained by fitting $d\sigma/d\Omega$ for $\gamma p \to K^0\Sigma^+$. 143
A.19 The total cross section for $\gamma p \to K^0\Sigma^+$ without subtraction of background (filled squares) and estimation of the total contribution of background stemming from the background reactions and the empty target (open crosses) as described in the text. . 144
A.20 The total cross section for $\gamma p \to K^0\Sigma^+$ after background subtractions as a function of c.m. energy W. The uncertainties shown are due only to counting statistics. . . . 145
A.21 The total cross section for $\gamma p \to K^0\Sigma^+$ measured after background subtractions in this work (black circles) compared with results of prior experiments. Measurements by the SAPHIR Collaboration [58] using a liquid hydrogen (LH2) target are shown as pink stars, measurements by the CB-ELSA Collaboration [52] using a LH2 target are shown as green triangles, and measurements by Shende (CB-ELSA/TAPS Collaboration) [57] using a liquid deuterium target are shown as blue squares. 147

List of Tables

1-1 Summary of quark properties including their quantum numbers. Here S, C, B, T denote, respectively, the quantum numbers strange, charm, bottom (or beauty), and top. 2

1-2 Some of the physical parameters of the K_S^0 and K_L^0 with their decay modes. 7

1-3 The status of the N and Δ resonances [4]. The existence of **** resonances is considered certain, the existence of *** resonances is likely to certain, and the existence of ** and * resonance is fair and poor, respectively. 12

2-1 Some physical parameters of the K_S^0 and Λ. 18

3-1 Comparison of some of the main features of the HDSM and RTM3. RTM3 is the third race track microtron, the last stage of MAMI-B, and HDSM is the fourth stage of MAMI to increase the energy from 0.855 GeV to 1.5 GeV. Table from Ref. [40]. 34

3-2 Properties of the Crystal Ball. 41

3-3 Detection properties of TAPS. 46

3-4 Overview of data taking scheme. 54

4-1 Survival probability for several background reactions to $\gamma n \rightarrow K^0\Lambda$ calculated from Monte Carlo analysis. 84

A-1 Survival probability for several background reactions to $\gamma p \rightarrow K^0\Sigma^+$ calculated from Monte Carlo analysis. 131

B-1 $d\sigma/d\Omega$ for $\gamma p \rightarrow K^0\Sigma^+$. 148

B-1 Continued. 149

B-1 Continued. 150

B-1 Continued. 151

B-2 Total cross section for $\gamma p \to K^0\Sigma^+$. 152

C-1 $d\sigma/d\Omega$ for $\gamma n \to K^0\Lambda$. 153

C-1 Continued. 154

C-1 Continued. 155

C-1 Continued. 156

C-1 Continued. 157

C-2 Total cross section for $\gamma n \to K^0\Lambda$. 158

D-1 Legendre coefficients for $\gamma p \to K^0\Sigma^+$. 159

D-1 Continued. 160

E-1 Legendre coefficients for $\gamma n \to K^0\Lambda$. 161

E-1 Continued. 162

F-1 Total contribution to $\sigma_{\rm tot}(\gamma p \to K^0\Sigma^+)$ from different background reactions and the empty target. 163

G-1 Total contribution to $\sigma_{\rm tot}(\gamma n \to K^0\Lambda)$ from different background reactions and the empty target. 164

Acknowledgements

I am extremely thankful to my adviser Prof. Mark Manley for his guidance and support throughout the time I worked on my thesis.

I am grateful to all the members of the Crystal Ball at MAMI, TAPS, and A2 Collaborations, for their support in carrying out this experiment. Especially, I am thankful to D. L. Hornidge, A. Starostin, M. Unverzagt, J. W. Brudvik, and M. Corolija for their valuable contributions.

I am indebted to my friends Mr. N. H. Rai and Mr. D. Chamling who are my fellow co-founders of the United Education Foundation in Nepal. Both provided a constant source of encouragement for me to complete my Ph.D. at Kent State University. I am also grateful to Dr. S. Rai, Dr. S. Dahal (Subba), Dr. B. K. Shrestha, Mr. M. Ojha, Mr. B. Nepali, and Mrs. S. J. Rai for providing expert administration at the United Education Foundation in my six-year absence.

I am also thankful to all my friends in the Kent State University Department of Physics, especially M. Shrestha, N. Subba, P. Gyawali, F. Bhatta, C. P. Pokhrel, and G. Acharya who made my stay joyful. I would like to thank all the professors who taught me, and my special thanks goes to Dr. E. Mann and Dr. S. Margetis, who were members of my Ph.D. defense committee and qualifying exam committee, providing me an additional kick every time towards success.

Finally, my wife Sumitra Rai deserves my special thanks for her precious smiling even in the midst of my hard and struggling days. Thanks to my two daughters Suravi and Manasvi for their kind cooperation and understanding while I carried out my research.

This work was supported by the U.S. Department of Energy under grant DE-FG02-01ER41194.

Chapter 1

Introduction

This chapter begins by reviewing the basic classification scheme of hadrons within the quark model. A brief introduction to **quantum chromodynamics** (QCD) is also included. Following this review, we describe the physics motivations for our study of $\gamma n \to K^0\Lambda$ and then give an outline for the remainder of this dissertation.

1.1 Quark model

After the development of new experimental techniques at accelerator laboratories, more and more hadrons were discovered. This introduced a challenge to develop an appropriate classification scheme for hadrons. In 1964, Gell-Mann and Zweig [1] independently observed that a hadron consists of substructures called $\mathbf{quarks}$, which led to the development of the $\mathbf{quark\ model}$ for hadrons. Each quark has spin-$\frac{1}{2}$ and baryon number $\frac{1}{3}$. There are three generations of quarks. The basic properties of the three generations of quarks are given in the Table 1-1 in terms of the additive quantum numbers. The quark model for the light quarks (u, d, and s) is represented by using a flavor symmetry group *SU(3)*, which provides a good description of the observed hadron spectrum.

According to the quark model, these quarks combine with each other to form a group of particles called **hadrons**. The hadrons are divided into two groups: **baryons** and **mesons**. The three light quarks (up (u), down (d), and strange (s)) introduce a broken flavor $SU(3)$ symmetry. Each of the quarks has its corresponding antiquark, i.e., anti-up ($\bar{u}$), anti-down ($\bar{d}$), anti-strange ($\bar{s}$). The u and d quarks form an isospin doublet and the s quark is an isospin singlet. The corresponding isospin components I_3 for u and d quarks are $\frac{1}{2}$ and $-\frac{1}{2}$, respectively. The strange quark has assigned quantum number -1 for its strangeness, which is denoted by S. We can consider these two

Name	**Symbol**	**Charge (Q)**	**Isospin** $(\mathbf{I_3})$	**S**	**C**	**B**	**T**	**Constituent Mass (GeV/c^2)**
Down	*d*	$-\frac{1}{3}$	$-\frac{1}{2}$	0	0	0	0	0.35
Up	*u*	$+\frac{2}{3}$	$+\frac{1}{2}$	0	0	0	0	0.35
Strange	*s*	$-\frac{1}{3}$	0	-1	0	0	0	0.5
Charm	*c*	$+\frac{2}{3}$	0	0	$+1$	0	0	1.5
Bottom	*b*	$-\frac{1}{3}$	0	0	0	-1	0	4.5
Top	*t*	$+\frac{2}{3}$	0	0	0	0	1	171

Table 1-1: Summary of quark properties including their quantum numbers. Here S, C, B, T denote, respectively, the quantum numbers strange, charm, bottom (or beauty), and top.

quantum numbers I_3 and S as two perpendicular axes, as shown in Fig. 1.1, in order to classify the hadrons.

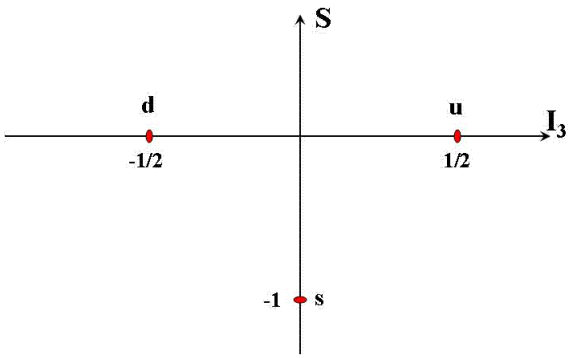

Figure 1.1: The members of the isospin doublets u and d quarks and the isospin singlet s quark can be used to form the two axes of the $SU(3)$ flavors.

During the strong interaction process, a quark and antiquark pair $(q\bar{q})$ can be created and/or annihilated.

1.1.1 Mesons in the quark model

Ordinary mesons are bound states of a quark and an antiquark with zero baryon number. Using *SU(3)* we can represent such mesons as:

$$q \otimes \bar{q} = 3 \otimes \bar{3} \rightarrow 1 \oplus 8. \tag{1.1}$$

Thus mesons can be placed in the singlet and octet representations of *SU(3)* symmetry. Since quarks are spin-$\frac{1}{2}$ fermions, in a meson the $q\bar{q}$ pair must have a total intrinsic spin equal to 0 or 1. The parity of a meson is expressed as $(-1)^{L+1}$, where L is the orbital angular momentum of the $q\bar{q}$ pair. In the ground state ($L = 0$) a meson always has negative parity.

Mesons with total spin zero and odd parity (J^P=0^-) are called **pseudoscalar mesons**. The nine members of the octet and singlet form a pseudoscalar meson nonet. The lightest pseudoscalar mesons include pions (π) with strangeness 0 and kaons (K) with strangeness $+1$. Likewise, the mesons with spin one and odd parity (J^P = 1^-) are called **vector mesons**, and the nine members

of the vector-meson octet and singlet form a vector-meson nonet. A diagram for the ground-state pseudoscalar and vector mesons is shown in Fig. 1.2.

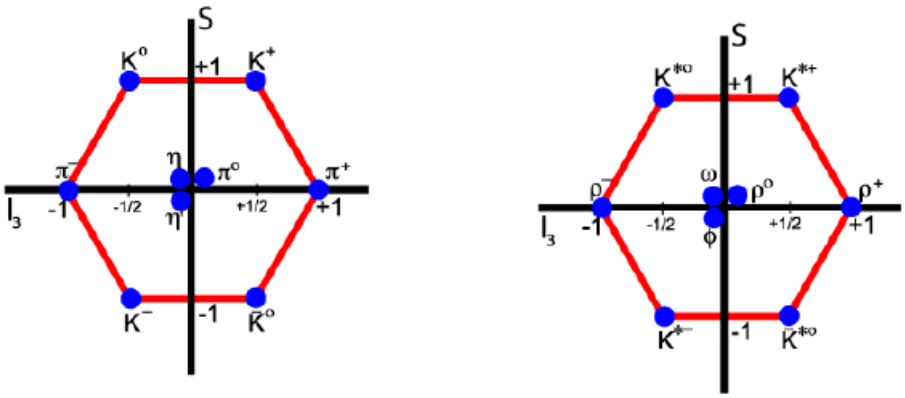

Figure 1.2: Left: The pseudoscalar mesons with $J^P = 0^-$. Right: The vector mesons with $J^P = 1^-$.

1.1.2 Neutral kaons

Neutral kaons are produced in strong and electromagnetic interactions as strangeness eigenstates:

$$K^0 \text{ (497)} = d\bar{s} \text{ and } \bar{K}^0 \text{ (497)} = s\bar{d},$$

with strangeness S = +1 and $S = -1$, respectively. These neutral kaons are anti-particles to each other. In weak decay interactions, strangeness is not a good quantum number and K^0 and $\bar{K}^0$ can be converted into each other by the process shown in Fig. 1.3. CP is approximately conserved in weak decays. The effect of CP on K^0 and $\bar{K}^0$ is given by

$$CP|K^0\rangle = \eta|\bar{K}^0\rangle \tag{1.2a}$$

$$CP|\bar{K}^0\rangle = \eta'|K^0\rangle, \tag{1.2b}$$

where η and η' are arbitrary phase factors satisfying $\eta\eta'$ = 1. We may choose $\eta = \eta'$ = 1. This equation clearly shows $|K^0\rangle$ and $|\bar{K}^0\rangle$ are not CP eigenstates. Consider the states, K_1 and K_2, which are formed by the linear combinations

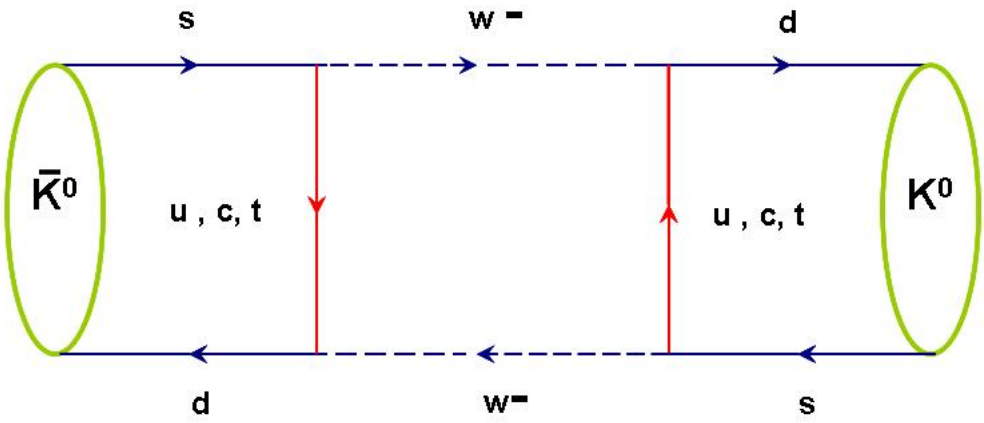

Figure 1.3: Feynman diagram showing the conversion of K^0 and $\bar{K}^0$.

$$|K_1\rangle = \frac{1}{\sqrt{2}}(K^0 + \bar{K}^0), \tag{1.3a}$$

$$|K_2\rangle = \frac{1}{\sqrt{2}}(K^0 - \bar{K}^0). \tag{1.3b}$$

From Eq. (1.2), it follows that K_1 and K_2 are CP eigenstates. For K_1, CP = +1 and for K_2, CP = -1:

$$CP|K_1\rangle = |K_1\rangle; \tag{1.4a}$$

$$CP|K_2\rangle = -|K_2\rangle. \tag{1.4b}$$

.

We ignore small CP-violating effects in the following discussion. Then K_1 and K_2 can be distinguished experimentally by their decay modes. If we consider CP to be conserved in weak decays, then K_1 can decay only into a state with CP = +1, while K_2 must decay only into a state with CP= -1. Experimentally, neutral kaons may decay into two or three pions. In the two-pion (2π) decay mode, the final-state pions have C = $(-1)^L$ and P = $(-1)^L$, so that CP = $(-1)^{2L}$ = +1, where L is the orbital angular momentum of the two pions. In the three-pion (3π) decay mode, the Q value which is the difference between the initial reactant mass (mass of a kaon) and the final

product mass (mass of 3π) is order of 70 MeV. This small value suggests that the three pions are in an S state with no angular momentum between any pairs of pions. Thus, parity of the 3π final state is

$$P = P_\pi^3 = -1, \text{ since } P_\pi = -1.$$

For the 3π final state, C = $+1$. Hence, for the 3π system, CP = -1. Thus the dominant mode of K_1 decay is 2π with CP= $+1$, while the K_2 may decay into 3π with CP = -1. Because of the very small Q value for the three-pion decay, the rate of K_1 decay into two pions is much faster than that of K_2 into three pions; thus, K_1 and K_2 have different lifetimes. Because of their lifetimes, K_1 and K_2 are called **short-lived neutral kaon** (K_S^0) and **long-lived neutral kaon** (K_L^0), respectively. Experimentally their lifetimes are

$$\tau_S = (0.08953 \pm 0.00005)\ \text{ns}, \tag{1.5a}$$

$$\tau_L = (51.16 \pm 0.20)\ \text{ns}. \tag{1.5b}$$

Because of their different lifetimes, K_S^0 can travel a few centimeters, whereas the K_L^0 can travel many meters. The states K^0 and $\bar{K}^0$ are superpositions of the states $|K_S^0\rangle$ and $|K_L^0\rangle$ as the inverse relation of Eq. (1.3). This allows us to write

$$|K^0\rangle = \frac{1}{\sqrt{2}}(K_S^0 + K_L^0), \tag{1.6a}$$

$$|\bar{K}^0\rangle = \frac{1}{\sqrt{2}}(K_S^0 - K_L^0). \tag{1.6b}$$

.

1.1.3 CP-Violation in neutral kaons

In 1964, Christenson $et\ al.$ [2] demonstrated that the long-lived neutral kaon could decay to $\pi^+\pi^-$ with a branching ratio of order 10^{-3}. This decay is a CP-violating process. This means that the physical states K_S^0 and K_L^0 do not exactly correspond to the CP-eigenstates K_1 and K_2 as just described above, but can contain small components of states with opposite CP:

$$|K_S^0\rangle = \frac{1}{\sqrt{1+|\epsilon|^2}}(|K_1\rangle + \epsilon|K_2\rangle), \tag{1.7a}$$

$$|K_L^0\rangle = \frac{1}{\sqrt{1+|\epsilon|^2}}(|K_2\rangle + \epsilon|K_1\rangle), \tag{1.7b}$$

where ϵ is a small complex number that measures the degree of CP-violation. Experimentally its magnitude is about 2.3×10^{-3}. Some important properties of the K_S^0 and K_L^0 including their decay modes are given in Table 1-2.

Properties	K_S^0	K_L^0
mass difference $(m_{K_S^0} - m_{K_L^0})$	(3.483± 0.006) $\times 10^{-12}$ MeV	
mean lifetime τ (ns)	0.08953 ± 0.00005	51.16 ± 0.20
decay modes	$\pi^+\pi^-$ (69.20±0.05)%	$\pi^+\pi^-\pi^0$ (12.54±0.05)%
and branching	$\pi^0\pi^0$ (30.69±0.05)%	$\pi^0\pi^0\pi^0$ (19.52±0.12)%
fractions	$\pi^+\pi^-\pi^0$ $(3.5^{+1.1}_{-0.9}) \times 10^{-7}$	$\pi^0\pi^0$ (8.65±0.06)$\times 10^{-4}$
	$\pi^0\pi^0\pi^0 < 1.2 \times 10^{-7}$	$\pi^+\pi^-$ (1.966±0.010)$\times 10^{-3}$
	$\pi^\pm e^\mp \nu_e$ (7.04±0.08)$\times 10^{-4}$	$\pi^\pm e^\mp \nu_e$ (40.55±0.12)%
	$\pi^+\pi^-\gamma$ (1.79±0.05)$\times 10^{-3}$	$\pi^\pm \mu^\mp \nu_\mu$ (27.04±0.07)%

Table 1-2: Some of the physical parameters of the K_S^0 and K_L^0 with their decay modes.

1.1.4 Baryons in the quark model

Ordinary baryons are bound states of three quarks with baryon number one. Each baryon has a corresponding antiparticle called an anti-baryon in which the quarks are replaced by their corresponding antiquarks. Using *SU(3)* we can represent the baryons as:

$$q \otimes q \otimes q = 3 \otimes 3 \otimes 3 \rightarrow 1 \oplus 8 \oplus 8 \oplus 10. \tag{1.8}$$

Thus baryons can be placed in the singlet, octet, and decuplet representations of *SU(3)* symmetry. The quark constituents of the baryon octet and decuplet are illustrated in Fig. 1.4.

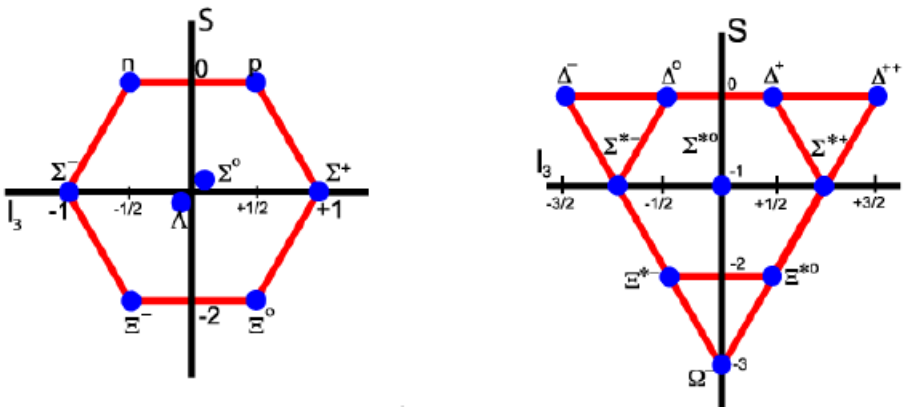

Figure 1.4: Left: The baryon octet with $J^P = \frac{1}{2}^+$. Right: The baryon decuplet with $J^P = \frac{3}{2}^+$.

The most common baryons are the proton and neutron: $p = |uud\rangle$ and $n = |udd\rangle$, which are collectively called **nucleons** (N). The baryon octet with $J^P = \frac{1}{2}^+$ also includes the isosinglet Λ and isotriplet Σ baryons with strangeness -1. Baryons with nonzero strangeness are called **hyperons**. The Λ (uds) with $B = 1$, $Q = 0$, and $S = -1$ is the lightest hyperon or strange baryon.

1.2 Quantum Chromodynamics (QCD)

Quantum chromodynamics (QCD) is the theory of the strong interaction which attempts to describe the 'quarks' and 'gluons' found in hadrons. At high energy, the strong coupling constant becomes smaller which results in the quarks and gluons interacting very weakly. Inside a hadron, when quarks become asymptotically close, they behave as non-interacting particles. At medium energies (up to few GeV), the strong force is still an enigmatic force.

Although the original quark model explained successfully the classification of the mesons and some baryons, the explanation of the Δ^{++} state in the baryon decuplet required an additional quantum number called **color**. Each quark carries one of three colors: red, green, or blue and each anti-quark carries one of three anti-colors: anti-red, anti-green, or anti-blue. All the hadrons

are color singlet states as these quarks are confined with other quarks by the strong interaction to form pairs (as in mesons) and triplets (as in baryons) so that the color is neutral. Because of color confinement, the force between quarks never vanishes as they are separated and it would take an infinite amount of energy to separate two quarks. Thus quarks are forced to be in a bound state in an infinitesimally small volume of a hadron and it is impossible to free a quark from its combination. Like quarks, gluons also carry color charges and participate in the strong interaction. These colors, which are additional degrees of freedom for the quarks, are an analog of electric charge in quantum electrodynamics (QED). Actually gluons are the exchange particles for the color force between the quarks analogous to the exchange of photons between two charged particles in the electromagnetic force. However, unlike the electrically neutral photons of QED, gluons carry the color charges of QCD. Thus like the representation of the photon interaction in QED, the gluon interaction can be represented by a Feynman diagram as shown in Fig. 1.5. Just as in QED in which a charged particle emits or absorbs photons, vertices in QCD allow a quark to emit or absorb a gluon.

The strong nuclear force is one of the most complicated subjects in physics. QCD explains the strong interaction in the high-energy region successfully. Here hadrons are described well in terms of partons (quarks and gluons), where asymptotic freedom allows the use of perturbative quantum chromodynamics (pQCD). However, at lower energies the pQCD treatment breaks down and therefore the explanation of the strong interaction in the medium-energy (resonance region) is still one of the unsolved problem in physics [3]. Effective field methods, such as chiral perturbation theory (ChPT) have been successful at low energies, but its extension to the resonance regime is difficult.

1.3 Nucleon resonances

In the quark model, many of the particles in the ground state baryon octet ($J = 1/2$) and baryon decuplet ($J = 3/2$) have the same valence quarks combinations. This suggests that many particles in the baryon decuplet can be produced by supplying enough energy to change the alignment of their quark contents (total spin $\frac{3}{2}$ from total spin $\frac{1}{2}$) in the baryon octet. Figure 1.6 shows how a

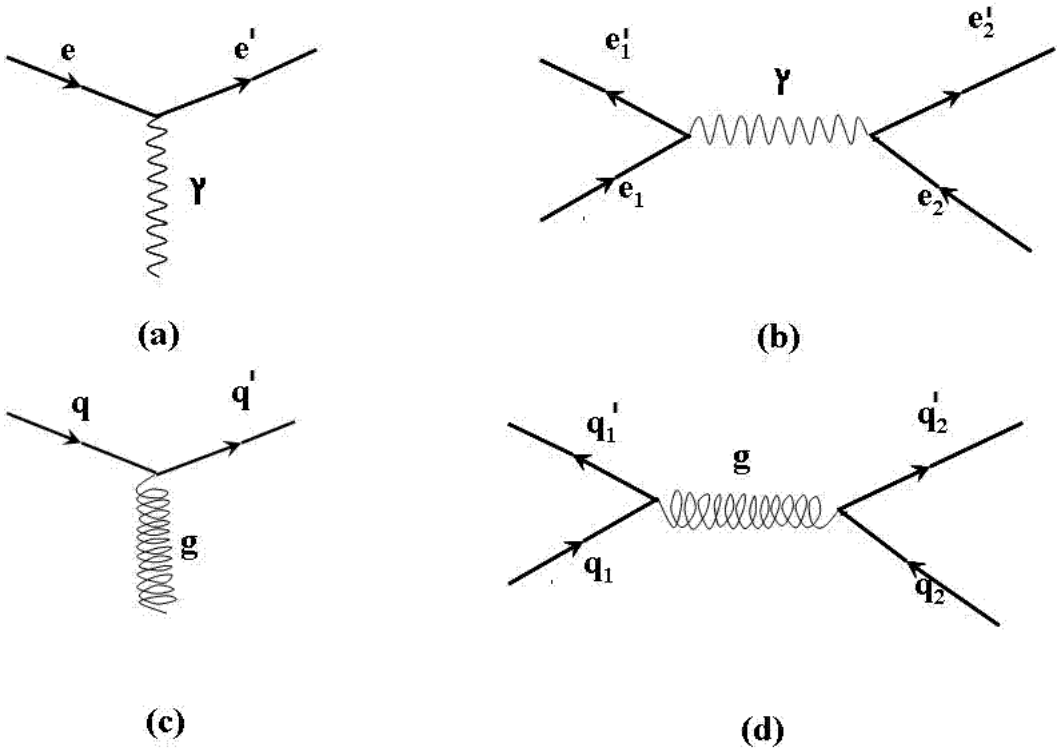

Figure 1.5: (a) The QED vertex showing the emission or the absorption of a photon (represented by a wavy line) by a charged particle. (b) The electromagnetic interaction between the charged particles e_1 and e_2 with the exchange of a photon (c) The QCD vertex showing the emission or absorption of a gluon (represented by a spiral line) by a quark. (d) The strong interaction between two quarks q_1 and q_2 with the exchange of a gluon.

proton (octet) is changed into a Δ^+ (decuplet) just by flipping the spin of a quark in the proton.

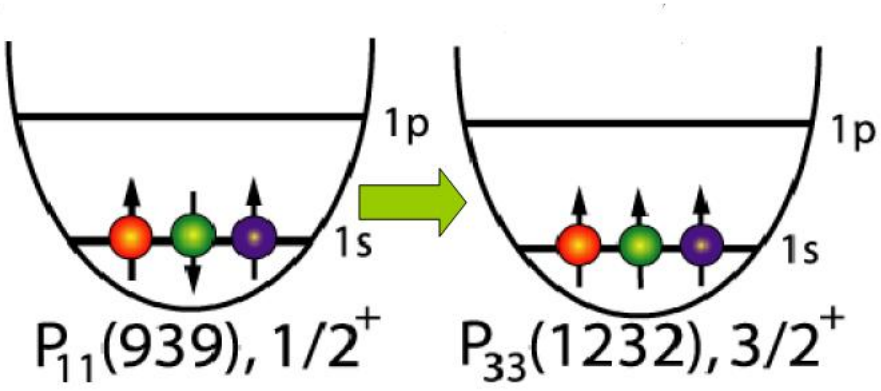

Figure 1.6: By flipping a quark's spin, a proton is changed into a Δ^+ .

Nucleons can be excited into higher energy states, called **resonances**. The resonances with zero strangeness are extremely short-lived and decay strongly with a mean lifetime of about 10^{-23} s, so that they cannot be observed directly. In the photoproduction process, the nucleon is excited into resonances via electromagnetic interaction with real photons. Resonances with isospin $I = \frac{1}{2}$ are called N resonances, and resonances with isospin $I = \frac{3}{2}$ are called Δ resonances. Collectively, N and Δ resonances are often called N^* resonances. When an energetic beam of photons is incident on a target nucleon, a peak in the particle production will sometimes be observed at the corresponding resonance energy. In the basis of these resonances, the hadrons can be classified in a proper way. There are many known baryon resonances as shown in Table 1-3. Each resonance is denoted by a symbol that consists of a capital letter showing the orbital angular momentum for the pion-nucleon decay channels (S, P, D, F) used as the usual spectroscopic notation. This capital letter is followed by two subscripts $2I$ and $2J$, and usually the approximate mass of the resonance (in MeV) is enclosed in parentheses.

Resonance	$\mathbf{L_{2I-2J}}$	**Status**	**Resonance**	$\mathbf{L_{2I-2J}}$	**Status**
N(939)	P_{11}	****	$\Delta(1232)$	P_{33}	****
N(1440)	P_{11}	****	$\Delta(1600)$	P_{33}	***
N(1520)	D_{13}	****	$\Delta(1620)$	S_{31}	****
N(1535)	S_{11}	****	$\Delta(1700)$	D_{33}	****
N(1650)	S_{11}	****	$\Delta(1750)$	P_{13}	*
N(1675)	D_{15}	***	$\Delta(1900)$	S_{31}	**
N(1680)	F_{15}	****	$\Delta(1905)$	F_{35}	****
N(1700)	D_{13}	***	$\Delta(1910)$	P_{31}	****
N(1710)	P_{11}	***	$\Delta(1920)$	P_{33}	***
N(1720)	P_{13}	***	$\Delta(1930)$	D_{35}	*
N(1900)	P_{13}	**	$\Delta(1940)$	D_{33}	*
N(1990)	F_{17}	**	$\Delta(1950)$	F_{37}	****
N(2000)	F_{15}	***	$\Delta(2000)$	F_{35}	****
N(2080)	D_{13}	**	$\Delta(2150)$	S_{31}	*
N(2090)	S_{11}	*	$\Delta(2200)$	G_{37}	*
N(2100)	P_{11}	*	$\Delta(2300)$	H_{39}	**
N(2190)	G_{17}	**	$\Delta(2350)$	D_{35}	****
N(2200)	P_{11}	**	$\Delta(2390)$	F_{39}	**
N(2220)	H_{19}	****	$\Delta(2400)$	G_{39}	**
N(2250)	G_{19}	****	$\Delta(2420)$	H_{311}	****
N(2600)	I_{111}	***	$\Delta(2750)$	I_{313}	**
N(2700)	K_{114}	**	$\Delta(2950)$	K_{315}	**

Table 1-3: The status of the N and Δ resonances [4]. The existence of **** resonances is considered certain, the existence of *** resonances is likely to certain, and the existence of ** and * resonance is fair and poor, respectively.

1.4 Physics motivation

Since the electromagnetic interaction provides an accurate and well-understood probe, meson photoproduction plays an important role in the nonperturbative region [5]. Due to the advent of several world-class electron accelerator facilities (CLAS at JLab, MAMI at Mainz, ELSA at Bonn, etc.), there have been numerous recent measurements involving photoproduction of single and double pions [6, 7], η mesons [8, 9], ϕ mesons and charged kaons (K^+ mesons) [11, 12]. When the present work began, there were no published measurements of neutral kaon photoproduction. Such measurements recently became feasible at the upgraded MAMI-C facility in Mainz, Germany. This dissertation reports on the world's first measurement of the differential and total cross section for the $\gamma n \rightarrow K^0\Lambda$ reaction. The measurements were performed at MAMI-C using a tagged photon beam incident on a liquid deuterium target. Final-state photons were detected using multiphoton spectrometers known as the Crystal Ball and TAPS (see Chapter 3). As kaon photoproduction on the neutron is isospin-$\frac{1}{2}$ selective, the reaction $\gamma n \rightarrow K^0\Lambda$ can provide essentially new information about the spectrum of N^* resonances. In addition, this reaction is also important to develop a theoretical understanding of the differences between the $\gamma n \rightarrow K^0\Lambda$ and $\gamma p \rightarrow K^+\Lambda$ reactions.

1.5 Outline of Current Work

This dissertation is divided into six chapters. Chapter 2 describes the theory and kinematics of kaon photoproduction. This chapter also describes some recent experiments similar to our research work. Chapter 3 gives a brief description of the experimental set-up at MAMI-C. It describes the various detector systems and gives an overview of their electronics. Chapter 4 describes the process used to calibrate the different detectors used in our experiment. In addition, this chapter explains the methods used to reconstruct the energy and momentum of various particles, and the procedure used for background subtraction. The method of kinematic fitting used for event reconstruction process is also described in detail. Chapter 5 describes the results of this analysis with the differential and the integrated cross section. Chapter 6 includes a summary and conclusions of our work. Appendix A outlines the analysis of $\gamma p \rightarrow K^0\Sigma^+$, the major background reaction to $\gamma n \rightarrow K^0\Lambda$

in our experiment. Appendix B and Appendix C tabulate the total cross sections for the reactions $\gamma p \rightarrow K^0\Sigma^+$ and $\gamma n \rightarrow K^0\Lambda$, respectively. Appendix D and Appendix E tabulate values of the Legendre fitting coefficients for $\gamma p \rightarrow K^0\Sigma^+$ and $\gamma n \rightarrow K^0\Lambda$, respectively. Finally, the percentage contributions of the background reactions to $\gamma p \rightarrow K^0\Sigma^+$ and $\gamma n \rightarrow K^0\Lambda$ are tabulated in Appendix F and Appendix G, respectively.

Chapter 2

Theory, Kinematics, and Previous Experiments

This chapter begins with a brief description of how we identified the events for the $\gamma n \to K^0\Lambda$ reaction. It also provides a theoretical description of kaon photoproduction. Some of the recent prior experiments on the photoproduction of neutral kaons are discussed at the end of this chapter.

2.1 Kaon photoproduction process

There are six elementary strangeness photoproduction reactions:

$$\gamma + p \to K^+ + \Lambda, \tag{2.1a}$$

$$\gamma + p \to K^+ + \Sigma^0, \tag{2.1b}$$

$$\gamma + p \to K^0 + \Sigma^+, \tag{2.1c}$$

$$\gamma + n \to K^0 + \Lambda, \tag{2.1d}$$

$$\gamma + n \to K^+ + \Sigma^-, \tag{2.1e}$$

$$\gamma + n \to K^0 + \Sigma^0. \tag{2.1f}$$

Among these reactions, (2.1a) and (2.1b) have received intensive experimental attention [13–17]. Our experimental work is focused on reaction (2.1d), $\gamma+n \to K^0+\Lambda$, which has an all-neutral final state and has received little experimental attention. We detected the final-state K^0 as a K^0_S through its decay chain,

$$K^0_S \to \pi^0\pi^0 \to 4\gamma. \tag{2.2}$$

We detected the final-state Λ through its decay chain,

$$\Lambda \to \pi^0 n \to 2\gamma + n. \tag{2.3}$$

Thus, the chain for the events of reaction (2.1d) is

$$\gamma + n \rightarrow K^0 + \Lambda \rightarrow 3\pi^0 + n \rightarrow 6\gamma + n. \tag{2.4}$$

As noted in Chapter 1, the final-state photons were detected using a multiphoton spectrometer known as the Crystal Ball (CB), which is described in Chapter 3.

In our experiment a photon beam was incident on a liquid deuterium target. The reaction process is shown schematically in Fig. 2.1. The neutral kaon photoproduction process in terms of branching ratios can be represented as shown in Fig. 2.2.

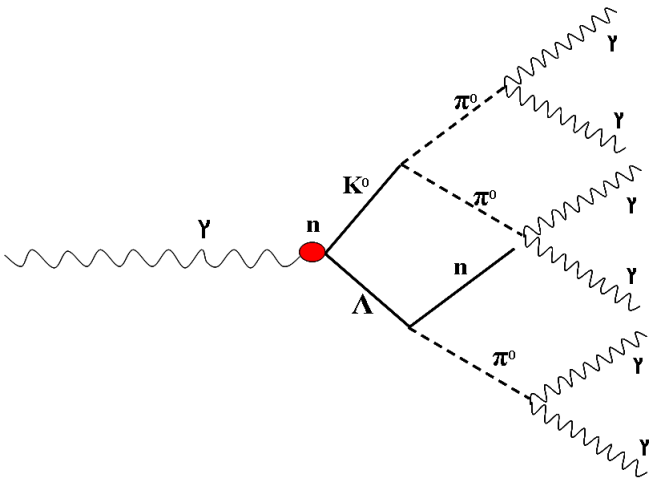

Figure 2.1: Schematic representation of the reaction $\gamma n \rightarrow K^0\Lambda$ as detected in our experiment.

In the reaction $\gamma n \rightarrow K^0\Lambda$, strangeness is conserved as the neutron (udd) has zero strangeness and the K^0 $(d\bar{s})$ and Λ (uds) have strangeness +1 and -1, respectively. The K^0 can decay into a K^0_S and K^0_L with equal probability. Because of its long lifetime, the K^0_L will typically travel about 15.1 m before it decays; thus, it is very unlikely that it will decay within Crystal Ball (diameter $\sim$1.5 m). Consequently, only K^0_S mesons were taken into account in our analysis.

While calculating the cross section for $\gamma n \rightarrow K^0\Lambda$, the missing K^0_L is accounted for by the 50% branching ratio for $K^0 \rightarrow K^0_S$. The K^0_S predominantly decays into a $\pi^+\pi^-$ pair with a branching ratio of 69.20$\pm$0.05%, but it has a significant branching ratio of 30.69$\pm$0.05% into the

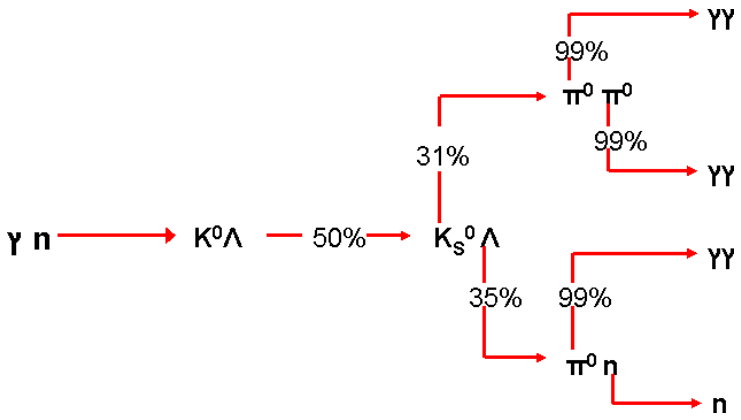

Figure 2.2: Representation of the reaction $\gamma n \rightarrow K^0\Lambda$ using branching ratios. The K^0 has equal probability to decay into K^0_S and K^0_L. Only the K^0_S was detected in our experiment.

$\pi^0\pi^0$ channel. The Λ decays weakly into $\pi^0 n$ and $\pi^+ n$ with branching ratios of 35.8$\pm$0.5% and 63.9$\pm$0.5%, respectively. The π^0 decays into 2γ with a branching ratio of 99.798 $\pm$ 0.032%. The physical parameters of the particles K^0_S and Λ are summarized in Table 2-1.

2.1.1 Kinematics

In our experiment, liquid deuterium was used as the target since free neutron targets do not exist. We ignored Fermi motion of the neutrons, which were therefore assumed to be at rest in the lab. After the interaction of the incident photon beam with the neutron, the outgoing K^0_S makes a polar angle θ with respect to the direction of the incident photon as shown in Fig. 2.3.

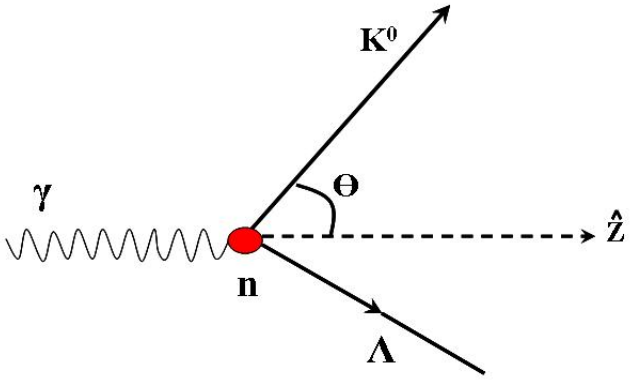

Figure 2.3: Diagram to represent the neutral kaon photoproduction mechanism.

Properties	K_S^0	Λ
Mass (MeV)	497.614±0.024	1115.683±0.006
$J^P(I)$	$0^-(\frac{1}{2})$	$\frac{1}{2}^+(0)$
$c\tau$ (cm)	2.684	7.89
Decay Modes	$\pi^+\pi^-$ (69.20±0.05)% $\pi^0\pi^0$ (30.69±0.05)%	π^0n (35.8± 0.5)% π^-p (63.9± 0.5)%

Table 2-1: Some physical parameters of the K_S^0 and Λ.

Let us consider $P^\mu_{\rm beam}$, P^μ_n, $P^\mu_{K_S^0}$, and P^μ_Λ as the four-momenta of the incident photon, target neutron, K_S^0 meson, and Λ hyperon, respectively. Now, using the energy-momentum conservation relation in four-momentum notation, we may write

$$P^\mu_{\rm beam} + P^\mu_n = P^\mu_{K_S^0} + P^\mu_\Lambda. \tag{2.5}$$

The superscript letter μ takes four values μ = 0,1,2,3, where $\mu = 0$ gives the energy (E) and the other values of μ represent the three-momentum ($\mathbf{P} = P^1, P^2, P^3$) of the four vector ($P^\mu$). The four-momentum of K_S^0 is determined by summing the four-momenta of its photon decays (4γs) as

$$P^\mu_{K_S^0} = \sum_i^4 P^\mu_{\gamma i}. \tag{2.6}$$

In the laboratory frame, these four-momenta can be expressed as

$$P^\mu_{\rm beam} = (E_{\rm beam}, \mathbf{P}_{\rm beam}), \tag{2.7a}$$

$$P^\mu_n = (E_n, \mathbf{P}_n) = (M_n, \mathbf{0}), \tag{2.7b}$$

$$P^\mu_{K_S^0} = (E_{K_S^0}, \mathbf{P}_{K_S^0}) = \sum_i^2 (E_{\pi_i^0}, \mathbf{P}_{\pi_i^0}). \tag{2.7c}$$

Since the square of the neutron four-momentum gives the invariant mass of the neutron (M_n), we can write $P_n^2 = P_n^\mu P_{n\mu} = E_n^2 - \mathbf{P}_n^2 = M_n^2$. As the target is at rest in the laboratory frame, it follows that $\mathbf{P}_n = 0$ and $E_n = M_n$ in Eq. (2.7b). The photon energy $E_{\rm beam}$ is measured by using the Glasgow Photon Tagger (see Chapter 3) and $E_{\rm beam} = \mathbf{P}_{\rm beam}c$ in Eq. (2.7a). When there is only one undetected particle in the final state (like Λ here), its kinematics is reconstructed by using four-momentum conservation. Using Eqs. (2.5) and (2.7c), the four-momentum (P_Λ^μ) of the undetected Λ can be expressed as

$$P_\Lambda^\mu = (E_\Lambda, \mathbf{P}_\Lambda) = P_{\rm beam}^\mu + P_n^\mu - P_{K_S^0}^\mu = P_{\rm beam}^\mu + P_n^\mu - \sum_i^4 P_{\gamma i}^\mu, \tag{2.8a}$$

where E_Λ and $\mathbf{P}_\Lambda$ are the energy and the three-momentum of the undetected Λ. Using Eqs. (2.7a), and (2.7b), these can be expressed as

$$E_\Lambda = E_{\rm beam} + M_n - \sum_i^4 E_{\gamma i}, \tag{2.8b}$$

$$\mathbf{P}_\Lambda = \mathbf{P}_{\rm beam} - \sum_i^4 \mathbf{P}_{\gamma i}. \tag{2.8c}$$

Thus the the missing mass $MM(K_S^0)$ of K_S^0 is given as

$$MM(K_S^0) = M_\Lambda = \sqrt{E_\Lambda^2 - \mathbf{P}_\Lambda^2}. \tag{2.8d}$$

The outgoing K_S^0 makes a polar angle θ with respect to the direction of the incident photon. For our reaction the three possible mechanisms for K_S^0 production can be expressed using the Mandelstam variables s, t, and u:

$$s = (P_{\rm beam}^\mu + P_n^\mu)^2 = W^2, \tag{2.9a}$$

$$t = (P_{\rm beam}^\mu - P_{K_s^0}^\mu)^2 = (P_n^\mu - P_\Lambda^\mu)^2, \tag{2.9b}$$

$$u = (P_{\rm beam}^\mu - P_\Lambda^\mu)^2 = (P_n^\mu - P_{K_S^0}^\mu)^2. \tag{2.9c}$$

Here, W is the total center-of-mass energy for the reaction.

2.1.2 Kaon center-of-mass angle ($\Theta^{K^0}_{\rm CM}$)

Figure 2.4 shows the reaction $\gamma n \rightarrow K^0\Lambda$ in the laboratory and center-of-mass (CM) frames. In the CM frame the products K^0_S and Λ travel back-to-back with equal and opposite momenta in a single plane. The angle between the K^0_S and γ momenta is called **kaon center-of-mass angle** ($\Theta^{K^0}_{\rm CM}$). The photon momentum defines the z-axis. If $\hat{p}_\gamma$ and $\hat{p}_{K^0_S}$ represent the direction of the photon and the kaon momenta, respectively, then the y-axis is defined as:

$$\hat{y} = \hat{p}_\gamma \times \hat{p}_{K^0_S}.$$

The CM reference frame moves with a velocity $\beta^{\rm CM}$ along the z-axis with respect to the laboratory frame as shown in Fig. 2.4. The kaon angle variation in this frame of reference is crucial in order to calculate the cross section in our work. In the laboratory frame, the three Cartesian components of $\mathbf{P}^{\rm Lab}_{K^0_S}$ are given as:

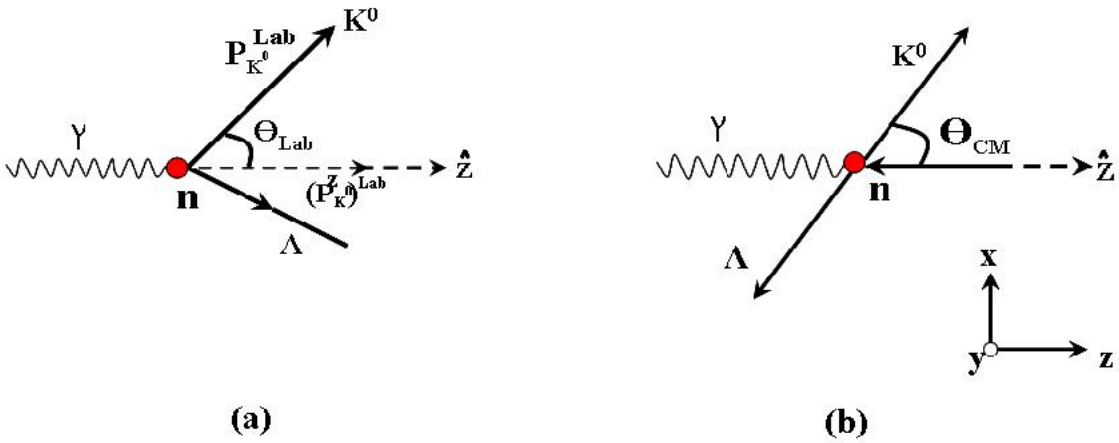

Figure 2.4: (a) The laboratory frame for K^0 photoproduction. (b) The center-of-mass frame for K^0 photoproduction. In both cases the direction of the incident beam is along the z-axis.

$$\mathbf{P}^{\rm Lab}_{K^0_S} = (P^x_{K^0_S}, P^y_{K^0_S}, P^z_{K^0_S}). \tag{2.10}$$

Similarly, the three Cartesian components of K^0_S in the CM reference frame are given as:

$$\mathbf{P}^{\rm CM}_{K^0_S} = ((P^x_{K^0_S})^{\rm CM}, (P^y_{K^0_S})^{\rm CM}, (P^z_{K^0_S})^{\rm CM}). \tag{2.11}$$

As there is only motion along the z-axis, we have [22]:

$$(P^z_{K^0_S})^{\rm CM} = (P^z_{K^0_S})^{\rm Lab} + \gamma^{\rm CM}\beta^{\rm CM}\left[\frac{\gamma^{\rm CM}\beta^{\rm CM}(P^{\rm Lab}_{K^0_S})}{(\gamma^{\rm CM}+1)} - E^{\rm Lab}_{K^0_S}\right], \tag{2.12}$$

while the other momentum components are the same in the laboratory and CM frames. Here $\beta^{\rm CM} = \frac{E_\gamma}{(E_\gamma + M_n)}$ and $\gamma^{\rm CM} = \frac{1}{\sqrt{1-(\beta^{\rm CM})^2}}$. Now using Eq. (2.12) we can express the kaon angle in the center-of-mass reference frame as:

$$\cos(\Theta^{K^0}_{\rm CM}) = \frac{(P^z_{K^0_S})^{\rm CM}}{|\mathbf{P}^{\rm CM}_{K^0_S}|}. \tag{2.13}$$

2.2 Theory of kaon photoproduction

In the last four decades, many theoretical explanations have been proposed to describe strangeness photoproduction. An isobar model which assumes that particle production and decay proceed via resonances and all subsequent decays, is suitable for the photon energy range 0.9 - 1.4 GeV in our work. In an isobar model, each decay is described as a quasi-two-body reaction. For example, the decay of B as B $\rightarrow$ M + N + E in the isobar model is written as B $\rightarrow$ X + E, where X = M + N is a resonance with a given mass and width. This model is based on the Feynman diagrammatic technique as shown in Fig. 2.5, which includes Born terms and resonance terms. In this phenomenological model, the kaon photoproduction process is described in terms of hadronic degrees of freedom using an effective Lagrangian approach. In 1966, the first isobar model for kaon photoproduction was developed by Thom [23], in which Feynman diagrams for Born terms and partial-wave amplitudes for the resonances were used. Because of the lack of experimental data, theoretical models made no significant progress for two decades after Thom's work. The isobar model was further improved by Adelseck *et al.* in 1985 by using diagrammatic techniques for the resonance and Born terms [24].

With the start of experimental activities at Jefferson Lab/CLAS, ELSA/SAPHIR, MAMI, and SPring-8/LEPS using continuous beam electron accelerators and detectors in the present decade, many theoretical explanations have been proposed to explain the experimental results. [25–30].

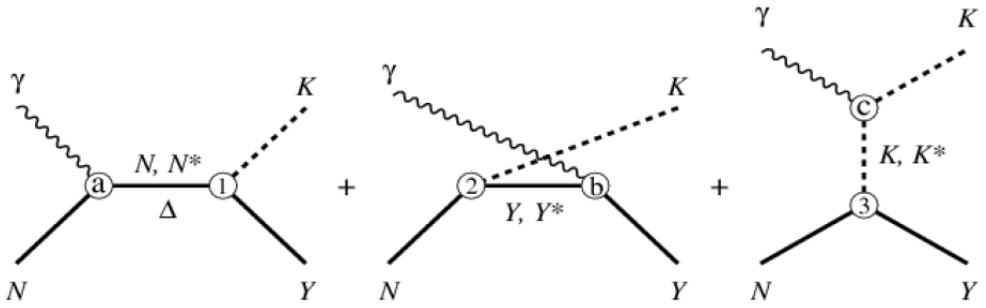

Figure 2.5: Feynman diagrams used in an isobar-model calculation of kaon photoproduction. The hadronic vertices are represented by (1), (2), (3) and the electromagnetic vertices by (a), (b), (c). In $\gamma n \rightarrow K^0\Lambda$, there is no contribution from the Δ resonance. The intermediate states N, Y, and K are associated with the Born terms and those N^*, Y^*, and K^* are associated with the resonance terms. The diagrams, from left to right, depict contributions from s-channel exchange, u-channel exchange, and t-channel exchange, respectively. Figure from Ref. [31].

Although many theories have been developed for K^+ photoproduction, there are only a few theories to explain K^0 photoproduction. Some of these are described in the following sub-sections.

2.2.1 Kaon-MAID model

The Kaon-MAID group [31] has put forward a theoretical prediction for exclusive quasifree kaon photoproduction in a Distorted Wave Impulse Approximation (DWIA) framework. They revised the tree-level model for the elementary kaon photoproduction using the $SU(3)$ values for the Born couplings and resonances consistent with a multi-channel analysis. They developed some relations based on isospin symmetry [33] to relate the coupling constants for the various reaction channels described in Sec. 2.1:

$$g_{K^+\Lambda p} = g_{K^0\Lambda n}, \tag{2.14a}$$

$$g_{K^+\Sigma^0 p} = -g_{K^0\Sigma^0 n} = g_{K^0\Sigma^+ p}/\sqrt{2} = -g_{K^0\Sigma^- n}/\sqrt{2}. \tag{2.14b}$$

The model also relates the electromagnetic couplings of the resonances to the proton and the neutron by means of the helicity amplitude $A_{1/2}$ of spin-$\frac{1}{2}$ resonances as [32]:

$$A^{\pm}_{1/2} = \pm\frac{1}{2m_N}\left(\frac{m_{N^*} - m_N^2}{2m_N}\right)^2 e g_{N^*N\gamma}, \tag{2.15}$$

where $e g_{N^*N\gamma}$ is the electromagnetic vertex coupling constant of the s-channel exchange diagram

shown in Fig. 2.5, and the $\pm$ sign refers to the parity of the resonance. Thus, the relation between helicity amplitudes for the production on the proton and on the neutron is given as

$$\frac{g_{N^{*0}n\gamma}}{g_{N^{*+}p\gamma}} = \frac{A^n_{1/2}}{A^p_{1/2}}. \tag{2.16}$$

In the electromagnetic vertices, the ratio of the neutral to the charged coupling constants must be known. In K^0 photoproduction, the coupling constant $g_{K^{*+}K^+\gamma}$ used in K^+ photoproduction must be replaced by the neutral coupling constant $g_{K^{*0}K^0\gamma}$. For the vector mesons $K^*(892)$ and $K_1(1270)$, the coupling constants are related to their decay widths (See Eq. (22) in Ref. [31]). Thus, the ratio of these two coupling constants is given as

$$r_{KK^*} = -\sqrt{\Gamma_{K^{*0}\to K^0\gamma}/\Gamma_{K^{*+}\to K^+\gamma}} = -1.53.$$

Since the decay widths of the K_1 meson are not known, the ratio r_{KK_1}, is treated as a free parameter and it was fixed using the available data in the $p(\gamma, K^0)\Sigma^+$ channel in the Kaon-MAID model.

The predicted total cross sections for the six channels of kaon photoproduction on the nucleon are shown in Fig. 2.6.

2.2.2 SLA model

J. C. David *et al.* [26] in 1996 developed a model based on an isobaric approach using Feynman diagrammatic techniques, which includes contributions from N^* resonances (spin $\leq \frac{5}{2}$), hyperons (spin-$\frac{1}{2}$), and kaon resonances. This model is known as the Saclay-Lyon (SL) model. Using this model, a series of investigations were performed for the several strangeness photoproduction processes for which experimental results were already available. The main kaon-hyperon-nucleon couplings were found to be in good agreement with the values predicted by using $SU(3)$ symmetry. This model was extended by T. Mizutani *et al.* [28] in 1998 with an improvement of the effective hadronic Lagrangian approaches by incorporating the correct spin-$\frac{3}{2}$ resonances propagator and what is called off-shell effects entering the vertices connected to the resonances. This extended model is valid for processes with a kaon $K(K^+, K^0)$ and a hyperon $Y(\Lambda, \Sigma^0, \Sigma^+)$ in the

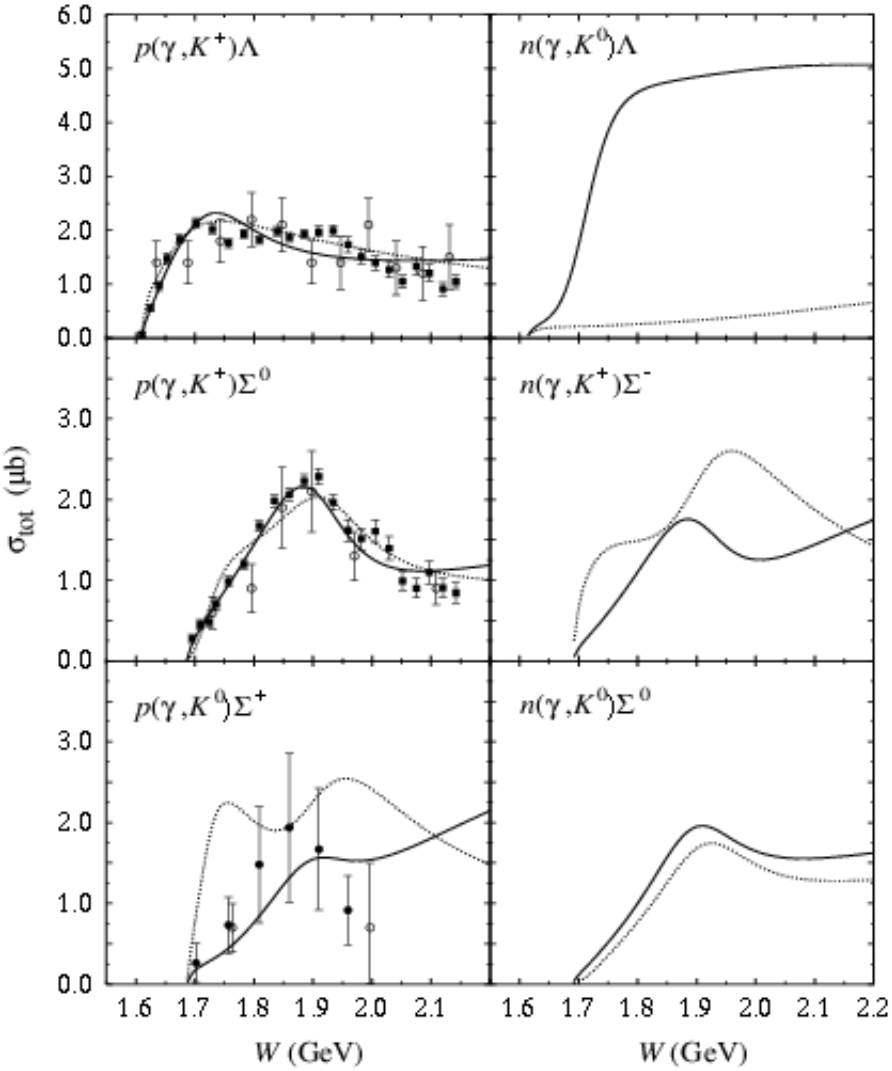

Figure 2.6: Theoretical results for the total cross section for the six channels of strangeness photoproduction for the Kaon-MAID model (solid lines shows the current and the dotted lines shows the older Kaon-MAID model as described in Ref. [31]). The solid squares represent the new SAPHIR data taken from Ref. [15], open circles represent the old data taken from Ref. [34], and the solid circles are the data from Ref. [35].

final state. The extended model has four variations. Model A is obtained by removing the nucleonic resonances N1 and N8 from Table I of Ref. [26]. The results of model A are called **SLA** in our analysis. As described for the Kaon-MAID model in Sec. 2.2.1, it is important to evaluate the elementary amplitudes in this model as well. Beside the Born terms, this model includes diagrams for $K^*(890)$ and $K_1(1270)$ exchange. The structure in hadronic vertices is modeled by point-like hadrons. Before this model can be applied to the $K^0\Lambda$ channel, the ratio of the electromagnetic transition coupling constants between the charged and neutral particles has to be adjusted. Like in the Kaon-MAID model, the ratios for processes involving a nucleon or a K^0 are known while those involving a $K_1(1270)$ are unknown. This ratio r_{KK_1} is free and has to be adjusted for K^0 production.

2.3 Previous experiments

Until recently, there were no published experimental results for the photoproduction of K^0 off the neutron. At the Thomas Jefferson National Accelerator Facility a new experiment designated g13, using tagged photons with both circular and linear polarization, was carried out in 2006 [18]. The data were taken using a liquid deuterium target with photon beam energies E_γ of 0.4-1.9 GeV and 0.5-2.5 GeV. As yet, no results from the analysis of these data have been published. Two new studies [19, 36], were conducted at the Laboratory of Nuclear Science (LNS) in Sendai, Japan with an incident photon energy up to 1.1 GeV. The next two sub-sections describe these studies.

2.3.1 ^{12}C target

K^0 photoproduction on a ^{12}C target was studied at the LNS in the photon energy range 0.8-1.1 GeV [19]. The neutral kaons were identified by the invariant mass constructed from two charged pions emitted in the $K^0_S \to \pi^+\pi^-$ decay channel. This photoproduction reaction has been considered as the mirror of $\gamma + p \to K^+ + \Lambda$, as the coupling constants $g_{K^+\Lambda p}$ and $g_{K^0\Lambda n}$ have the same sign and magnitude for the two reactions because of isospin symmetry ($g_{K^+\Lambda p} = g_{K^0\Lambda n}$).

The integrated cross sections for K^0 and K^+ photoproduction are plotted in Fig. 2.7 as a function of photon energy E_γ. This figure shows that the cross sections for both K^0 and K^+ photoproduction on ^{12}C are similar in magnitude, which suggests that the elementary cross sections $n(\gamma, K^0)\Lambda$ and $p(\gamma, K^+)\Lambda$ are of the same order.

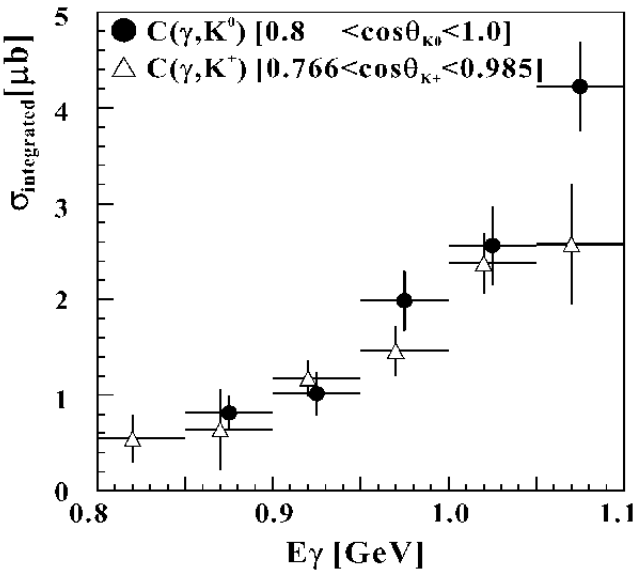

Figure 2.7: The filled circles represent the total cross section for $^{12}\mathrm{C}(\gamma, K^0)$ and the open triangles represent that for $^{12}\mathrm{C}(\gamma, K^+)$. Figure from Ref. [37].

As described in Sec. 2.2.1, it is important to fix the values of r_{KK_1} for the Kaon-MAID and SLA models of K^0 photoproduction. For this work, the value of the ratio r_{KK_1} for Kaon-MAID was -0.447, and for SLA was tested for the three values -0.447, -1.5, and -3.4. Out of these three values, satisfactory results were observed for $r_{KK_1} = -1.5$. Figure 2.8 shows predictions for the differential cross section of $\gamma n \to K^0\Lambda$ at the photon energy E_γ= 1.05 GeV. These predictions resulted from comparing the measured momentum spectra with those calculated by the models. The SLA prediction with $r_{KK_1} = -1.5$, which represents a gentle backward angular distribution, provides a reasonable agreement with the experimental data. The dashed line represents the result from Kaon-MAID, which is concave. The SLA model predictions for $r_{KK_1} = -0.447$, -1.5, and -3.4 are represented by dotted, solid, and dot-dashed lines, respectively.

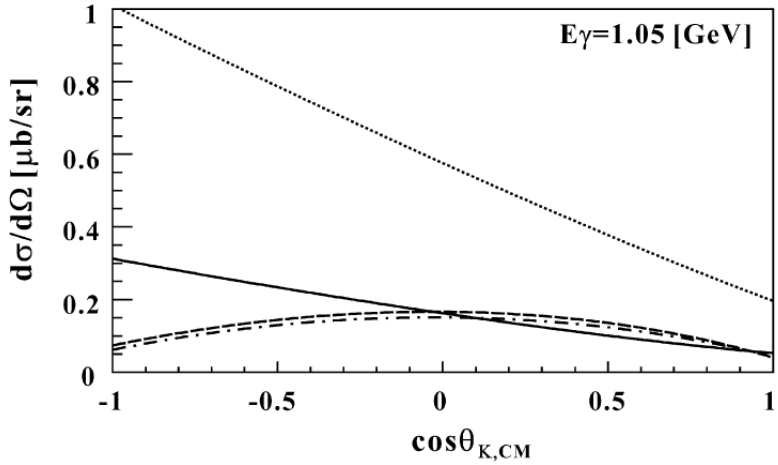

Figure 2.8: Differential cross section for $\gamma n \rightarrow K^0\Lambda$. The Kaon-MAID model is shown by the dashed line and SLA model predictions for r_{KK_1} = -0.447, -1.5, -3.4 are represented by the dotted, solid, and dot-dashed lines, respectively. Figure from Ref. [19].

2.3.2 Liquid deuterium target

K. Tsukada *et al.* [36] used a liquid deuterium target to study the photoproduction of neutral kaons at the LNS with an incident photon energy up to 1.1 GeV. This was the first published work for $\gamma n \rightarrow K^0\Lambda$ in the threshold region using a deuterium target. The neutral kaons were detected from the positive and negative pions emitted in the decay $K^0_S \rightarrow \pi^+\pi^-$.

In order to calculate theoretical predictions of cross sections and other observables for channels that include K^0 in the final state, Tsukada *et al.* assumed isospin symmetry for the strong coupling constants and appropriately adopted electromagnetic coupling constants for the neutral mode by replacing those for the charged mode in Kaon-MAID [31]. As mentioned in Sec 2.2.1, for the t-channel meson resonances, the ratio of the coupling constants for the neutral and the charged modes is well known for $K^*(892)$ but unknown for the $K_1(1270)$ resonance. This ratio for the latter, r_{KK_1} was fixed at -0.45 as in the work of Tsukada *et al.*. This value of r_{KK_1} differs from that quoted in Ref. [31], and it has been used in the newer version of the Kaon-MAID model (See Ref.[31] of Ref. [36]). By comparing the measured inclusive momentum distribution with the theoretical calculation, the value of r_{KK_1} for SLA model has been selected, and it is -2.09.

A simple phenomenological parametrization in the CM system was introduced to describe the angular dependence of the elementary cross section as

$$\frac{d\sigma}{d\Omega} = \sqrt{(s-s_0)}(1+e_0(s-s_0))(a_0P_0(x)+a_1P_1(x)+a_2P_2(x)), \tag{2.17}$$

where $P_l(x)$ are Legendre polynomials, $x = \cos(\Theta^K_{\rm CM})$, s is the square of the photon-nucleon CM energy ($s = W^2$), and s_0 = 2.603 GeV^2, the $K^0\Lambda$ threshold. This is called the PH parametrization. The best-fit parameters, denoted as PH1, were $a_0 = 0.0884, a_1 = -0.0535, a_2 = -0.0098$, and $e_0 = -0.132$. The parametrization with the opposite of sign for a_1 is named PH2, which is expected to give the inverse angular distribution as that of PH1.

The predicted differential cross section for $\gamma n \to K^0\Lambda$ in the CM system for incident photon energies of E_γ = 0.97 GeV and E_γ = 1.1 GeV is shown in Fig. 2.9. The solid line represents the Kaon-MAID [31] prediction and the dotted line represents the SLA prediction [28]. Similarly the PH1 and PH2 predictions are denoted by the dashed line and dotted dashed line, respectively.

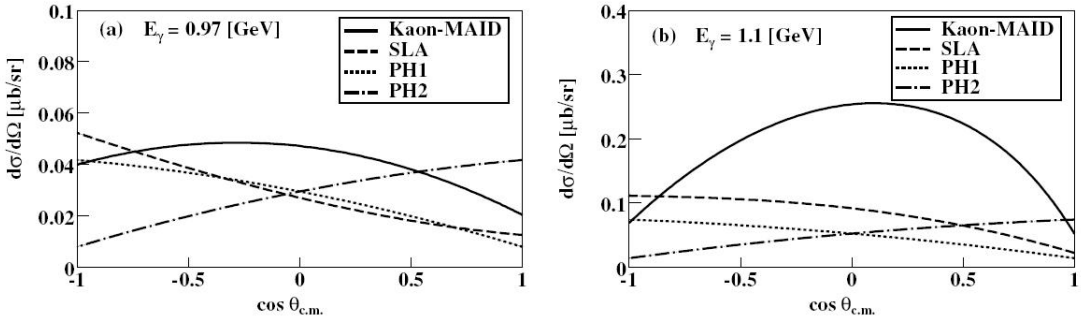

Figure 2.9: The differential cross section for $\gamma n \to K^0\Lambda$ as predicted by Kaon-MAID [31] (solid line), SLA [28] (dotted line), PH1 (dashed line), and PH2 (dotted dashed line).

Figure 2.10 shows the corresponding predicted total cross section for $\gamma n \to K^0\Lambda$ as a function of photon energy for SLA, Kaon-MAID, PH1, and PH2. Because of the limited kinematical acceptance for K^0, the work of Tsukada *et al.* was unable to extract the experimental total cross section. The Kaon-MAID plot for the total cross section is almost convex in shape and there is a very sharp

rise from threshold (920 MeV) up to $E_\gamma \simeq 1.2$ GeV, whereas the results of SLA, PH1, and PH2 show a flatter energy dependence with a much smaller cross section near the threshold region.

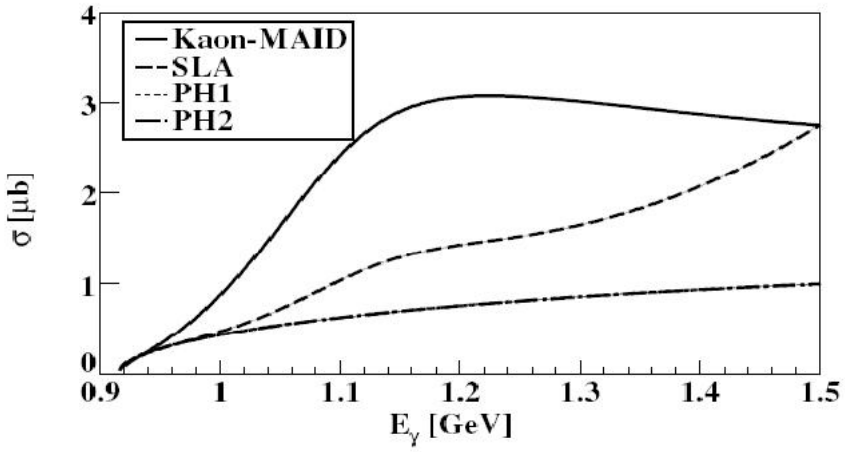

Figure 2.10: Comparison of the total cross section for $\gamma n \rightarrow K^0\Lambda$. The Kaon-MAID prediction [31] is represented by the solid line, SLA [28] by the dotted line, and the PH1 and PH2 predictions coincide with each other and are represented by the dashed dotted line. Figure from Ref. [36].

Chapter 3

Experimental Setup

This chapter describes the experimental facility used by the A2 Collaboration in Mainz, Germany. The set-up is mainly comprised of the three components shown in Fig. 3.1. The primary component is the electron accelerator, which is also called the **Mainz Microtron** (MAMI-C). It produces a continuous-wave electron beam. The beam of electrons from MAMI-C is directed onto a thin diamond or copper foil generating a beam of high-energy photons via a bremsstrahlung process. The second component is the Glasgow Photon Tagging Spectrometer, which is used to analyze the momentum of the corresponding bremsstrahlung electrons. The photon beam is allowed to impinge on a target causing the production of various particles. The third component, which is the detector system used to detect these particles and their decays, consists of the Crystal Ball (CB) and the TAPS spectrometer.

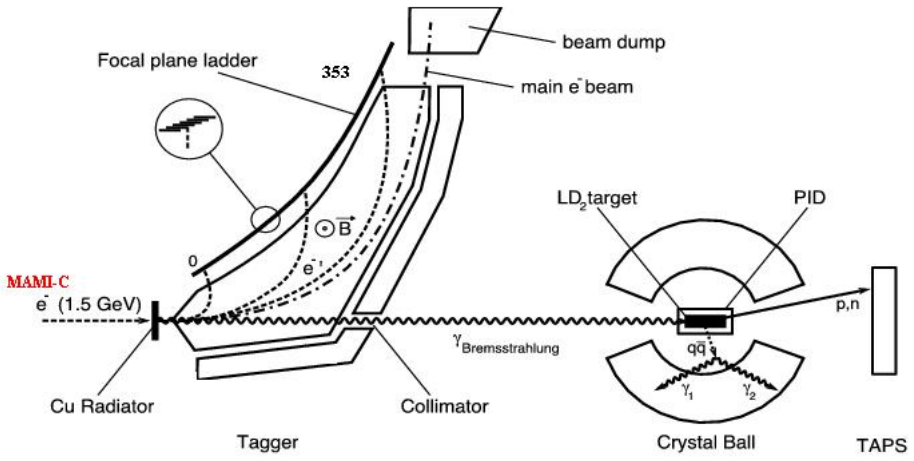

Figure 3.1: The experimental set-up in the A2 Hall in Mainz consists of three main components: (i) MAMI electron accelerator for production of electrons up to 1.5 GeV, (ii) Glasgow Photon Tagger, (iii) Detector system (CB, TAPS, PID, MWPC).

3.1 Mainz Microtron (MAMI)

The Mainz Microtron (MAMI) is an intense, stable and continuous-wave accelerator that accelerates electrons to the relativistic limit. It is operated by the Institut für Kernphysik at Johannes Guttenberg Universität in Mainz, Germany. The accelerator in its current configuration was constructed in four stages: (i) MAMI-A1, (ii) MAMI-A2, (iii) MAMI-B, and (iv) MAMI-C. MAMI-A1 was installed in 1979, producing electrons up to 14 MeV. In 1983, a second microtron was added, upgrading the facility to MAMI-A2 with maximum energy 183 MeV. With the addition of a third microtron in 1990, the maximum energy was increased to 855 MeV under the name MAMI-B. MAMI-C, which is the present facility, was set into operation in December, 2006 producing a continuous high quality electron beam with maximum energy 1.5 GeV. It supplies the electron beam to any of the experimental halls (A1, A2, A4, X1) as shown in Fig. 3.2.

MAMI-C consists of three cascades of RTMs (Race Track Microtrons) and a recently added Harmonic Double-Sided Microtron (HDSM). This new HDSM is considered as a worldwide unique recirculating electron accelerator. It consists of two systematic pairs of 90°-dipoles, each forming an achromatic 180° bending system as shown in Fig. 3.3. In order to compensate for the strong vertical defocusing due to the 45°-pole face inclination at beam entrance and exit, these dipoles incorporate an appropriate field gradient normal to the pole edge. This functions as a scheme for transversal focusing, with only two quadrupole doublets on each of the two dispersion-free anti-parallel linac axes. In the HDSM, the two linacs operate at different frequencies: one at 2.45 GHz and the other at 4.90 GHz. The linac operating at the lower frequency maintains a higher longitudinal stability. The linac at the higher frequency is responsible for a synchronous acceleration energy gain per turn below 20 MeV [39]. For the HDSM, the electron energy gained per turn is given by

$$\Delta E/\mathrm{turn} = n \times \frac{ecB}{(\pi - 2)} \times \lambda_{rf}, \tag{3.1}$$

where n is the number of complete turns made by electrons (n = 1 is the lowest possible value) and λ_{rf} is the rf-wavelength. The injection of the electrons is made from the result of RTM3 (MAMI-B)

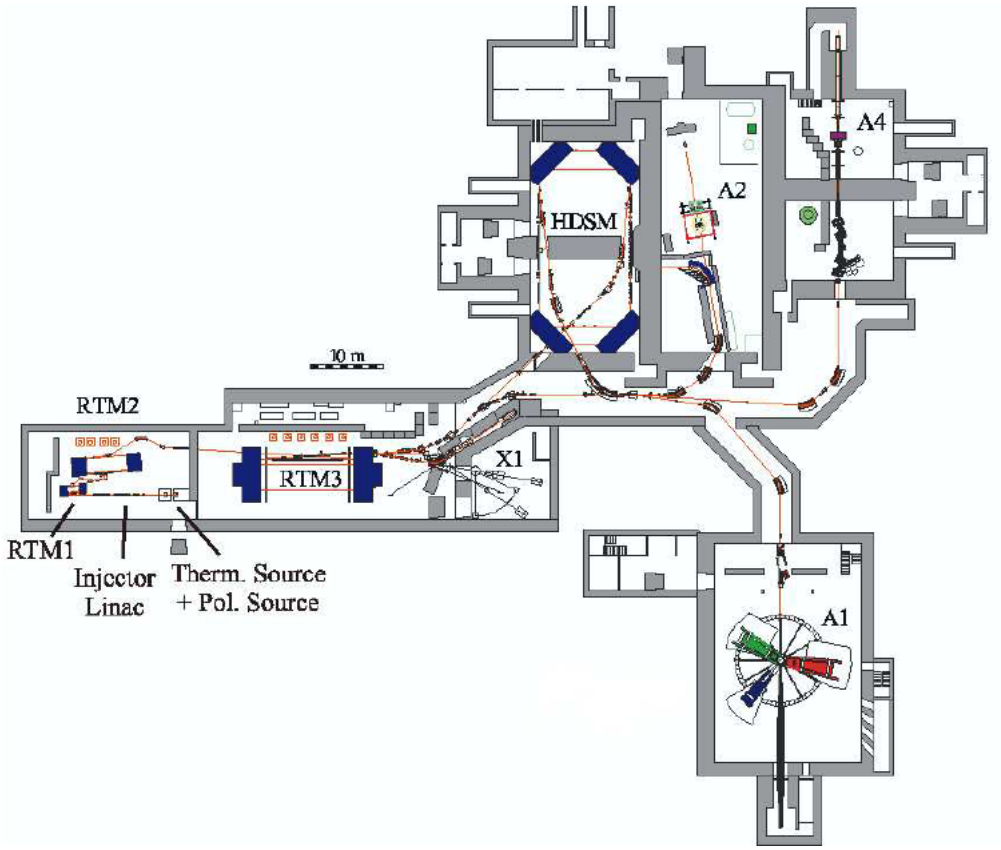

Figure 3.2: The floor plan of MAMI facility. Three racetrack microtrons RTM1, RTM2, and RTM3 together with the Harmonic Double Sided Microtron (HDSM) produce an electron beam with energy up to 1508 MeV in MAMI-C. A1, A2, A4, and X1 are the experimental halls. Our experimental work was carried out in the A2 Hall.

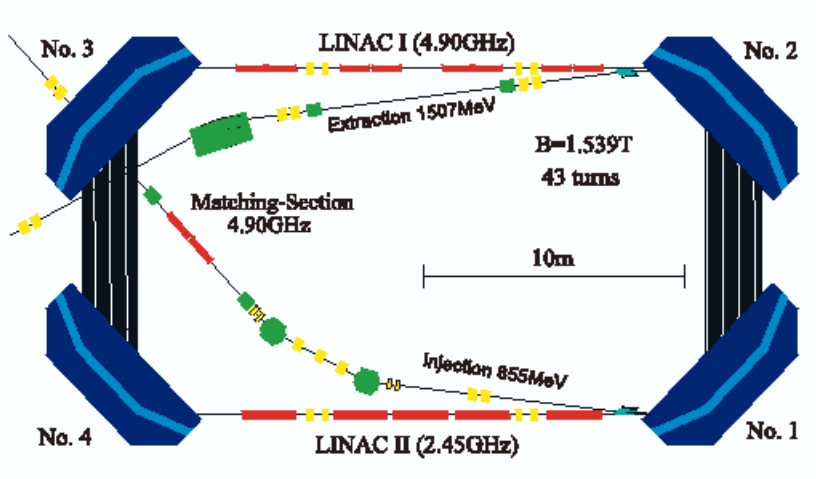

Figure 3.3: General layout of the HDSM. HDSM consists mainly of two pairs of 90° bending magnets and two linear accelerators. These two linear accelerators work on two different frequencies, 2.45 GHz and 4.90 GHz. Figure from Ref. [38]

with the value of $B = 1.23$ T, λ_{rf} = 0.1224 m; thus, from Eq. (3.1), $\Delta E = 41.1$ MeV/turn. This also needs 20 m long linacs, which would not fit into the existing MAMI-floor, as shown in Fig. 3.2. Moreover, it would consume four times the electric power of MAMI-B. So it is practicable to adjust the frequency of the HDSM at 4.90 GHz (λ_{rf} = 0.0612 m) with a small variation in B value as 1.823 T, to keep the length of the linacs about 10 m and the other parameters similar to that of RTM3. The HDSM takes the beam energy from 855 MeV to 1508 MeV by 43 turns in 14.0 to 16.7 MeV per step through its accelerating section. Table 3-1 shows a comparison of the main parameters of the HDSM to that of RTM3, which was the third stage known as MAMI-B.

3.2 The Glasgow Photon Tagger

The Glasgow Photon Tagger was installed in the A2 Hall in 1991 for MAMI-B with a maximum electron energy of 883 MeV. Recently the Tagger was upgraded for the MAMI-C accelerator to work up to maximum electron energy of 1508 MeV. The electron beam from MAMI-C is made to collide with a thin diamond or copper radiator of the Glasgow Tagger, to produce photons through the bremsstrahlung process:

Features	**Unit**	**RTM3 (MAMI-B)**	**HDSM (MAMI-C)**
General			
E_{injected}	MeV	180.2	855.3
E_{output}	MeV	855.3	1508.4
Turns	#	90	43
Power Consumption	kW	650	1400
RF System			**Linac 1 — Linac 2**
Linac amplitude	MV	7.8	9.05 — 9.30
Energy gained per turn	MeV	7.50	16.7 — 14.0
Frequency	GHz	2.4495	4.8990 — 2.4495
Electrical linac length	m	5×1.77	8×1.07 — 5×2.02
Beam load 100 μA	kW	67.5	37.0 — 28.4
Magnet System			
min./max. field	T	1.2842	0.939 — 1.539
min./max. gap	mm	100	85 — 140
min./max. radius	m	0.47 — 2.22	2.23 — 4.60
Weight	ton	2×450	4×250

Table 3-1: Comparison of some of the main features of the HDSM and RTM3. RTM3 is the third race track microtron, the last stage of MAMI-B, and HDSM is the fourth stage of MAMI to increase the energy from 0.855 GeV to 1.5 GeV. Table from Ref. [40].

$$e^- + A \rightarrow A + e^- + \gamma,$$

where e^- is an electron, A is a nucleus, and γ represents a photon. Using the principle of conservation of energy and momentum, the photon energy is given by

$$E_\gamma = E_0 - E_e, \tag{3.2}$$

where E_0 is the electron beam energy and E_e is the energy of the deflected electron. In this equation, the recoil energy of the nucleus has been ignored due to the large mass of the nucleus compared with the energy of the photon and electron. In order for the application of Eq. ((3.2)), the timing coincidence of each photon to the corresponding electron should be known. This process of using the timing coincidence to match an electron to its corresponding photon is called **tagging**.

The Glasgow Photon Tagger used for the tagging process is shown schematically in Fig. 3.4. It consists of 353 plastic scintillators that overlap each other to form a ladder in the focal plane of a quadrupole magnet of weight 1030 tons, which produces a magnetic field of 1.8 T. These focal-plane detectors have a length of 8 cm, a thickness of 0.2 cm, and widths of 0.9 to 3.2 cm. They cover an energy range from 6-95% of the energy of the primary electron beam. The different widths of these detectors are arranged in such a way as to achieve slightly more than half-overlap of neighboring detectors so that each tagging electron should trigger two detectors at a time. The width of the overlap region (a "channel") is equivalent to an energy width of $\sim$4 MeV for an incident electron beam energy of 1500 MeV, and neighboring channels overlap by about 0.4 MeV [41]. All the events involving only a single detector are rejected, which thereby reduces the background. Each detector is adjusted perpendicular to the anticipated electron's path for the electron momentum corresponding to that particular position in the focal-length plane. During the construction of the Tagger, the number of required focal-plane detectors was determined by the physical space occupied by a single photomultiplier. The 353 detectors provide a maximum comfortable packing density for the photomultiplier tubes, covering an electron range of 80 to 1401 MeV with photon flux up to $\sim$ 2.5 $\times 10^5$ photons per MeV and an energy resolution of about 4 MeV.

Most of the electrons in the incident beam do not interact with the radiator and are deflected by the magnet onto a Faraday cup called the **beam dump**. A collimator consisting of four lead

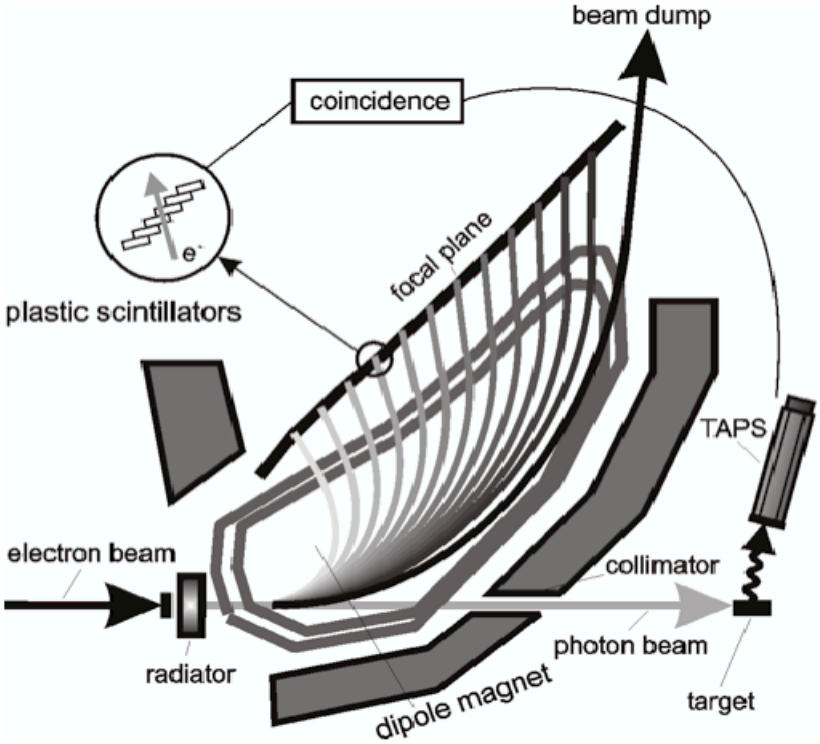

Figure 3.4: The Glasgow Tagger. As soon as the high-energy electron beam strikes the surface of the radiator, photons are created by the bremsstrahlung process. The trajectory of the electrons is bent by a huge Tagger dipole magnet onto the focal-plane detectors and the photons are sent to the target.

cylinders each 2 cm long with a 4 mm hole bored through the center parallel to the beam axis is used to eliminate the noise and deviations of the resulting photon beam. Thus because of the use of the collimator, the ratio of the photons to the electrons is always less than one. This ratio is called the **tagging efficiency**:

$$\varepsilon = \frac{N_\gamma}{N_e}, \tag{3.3}$$

where N_γ is the number of photons that passed through the collimator and N_e is the number of electrons detected in the tagger ladder. The tagging efficiency is measured by using a Pb-glass detector placed downstream of the collimator in the beam line to measure N_γ. While performing the tagging efficiency measurement, normal experimental beam currents may damage the lead-glass

detector. Therefore, a greatly reduced beam current was used to protect the lead-glass detector. The photon beam was monitored with an ionization chamber that measures the overall bremsstrahlung flux during normal running.

As the bremsstrahlung spectrum is a continuous one in which the photon flux varies as $N_\gamma \sim 1/E_\gamma$, a larger number of low-energy photons is produced that are accompanied by the high-energy photons. For our experiment, the high-electron energy (low-photon energy) area of the Tagger focal plane was switched off so that the energies of the tagged photons varied from 700 MeV to 1400 MeV.

3.3 The Crystal Ball

The Crystal Ball (CB) was designed in 1974 as a multiphoton spectrometer with high detection efficiency over a large solid angle. It was initially used to detect photons produced in high-energy e^-e^+ collisions [42] at SLAC (Stanford Linear Accelerator Center in Stanford, CA). From 1978 to 1981, it was used to investigate the spectroscopy of the J/Ψ and radiative decays of particles such as τ, Ψ, and D at SPEAR[1]. After this period, it was put into storage at SLAC until 1995 when it was moved to the AGS[2] facility at BNL, where it was used for the study of nucleon and hyperon spectroscopy, and rare η decays. It was moved to Mainz in 2002 and after completion of a major upgrade of the detector's electronics it was used at MAMI-B until 2005. It resumed operation in 2007 as the central detector at MAMI-C.

The CB consists of 672 thallium-doped sodium iodide NaI (Tl) crystals. These crystals are optically isolated from one another by wrapping them in reflecting paper and aluminized mylar. A SRC L50B01 type photomultiplier tube (PMT) of 5.1 cm diameter and 21 cm in length is arranged behind each crystal to convert the resulting light pulse into electric signals. Each crystal is shaped like a truncated pyramid of length 40.6 cm (or 15.7 radiation lengths) with the side of inner face 5.1 cm in length and the side of outer face 12.7 cm as shown in Fig. 3.5. These crystals are arranged

[1] Stanford Positron Electron Accelerating Ring
[2] Alternating Gradient Synchrotron

to form a ball structure as shown in Fig. 3.6 with an inner radius of 25.3 cm and outer radius of 66 cm.

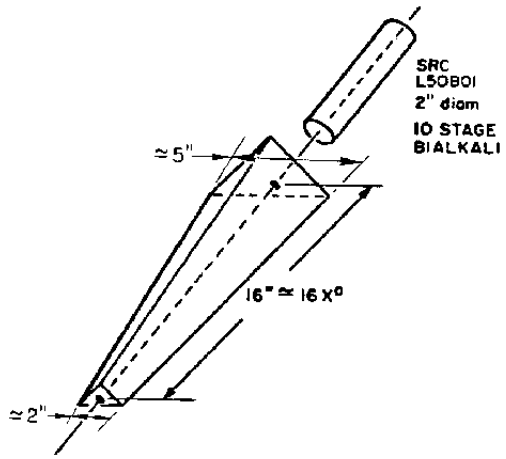

Figure 3.5: An individual crystal in the CB is 40.6 cm long with a truncated pyramid shape.

The geometry of the Crystal Ball is that of an icosahedron (a solid with 20 faces). These 20 faces form “major triangles” which in turn are divided into faces of four “minor triangles” each containing nine crystals as shown in Fig. 3.7. When these crystals are stacked together closely they form a spherical shell of 720 elements. In order to make a space for the photon beam and the target system, 24 crystals were removed from the opposite poles. The CB is divided into two hemispheres: an upper one and a lower one separated with two 0.8 mm stainless steel plates and a 0.8 cm air gap. Because of this, an active space amounting to 1.6% of the solid angle (or 4π) is introduced. Since NaI(Tl) is hygroscopic, all the crystals are hermetically sealed in the two separated hemispheres. This also helps to control the temperature ($\sim 23 \pm 2^{\circ}$C), pressure (low) and humidity ($\sim$30%) inside the hemispheres.

In the Crystal Ball, the incident photon beam produces electromagnetic showers that in turn deposit their energy in the NaI(Tl) crystals depending on the energy of the photon. An incident photon below 10 MeV may deposit energy only in one or two crystals whereas a photon up to 400 MeV deposits 98% of its energy in a cluster of 13 crystals. Because of this, the measurement of

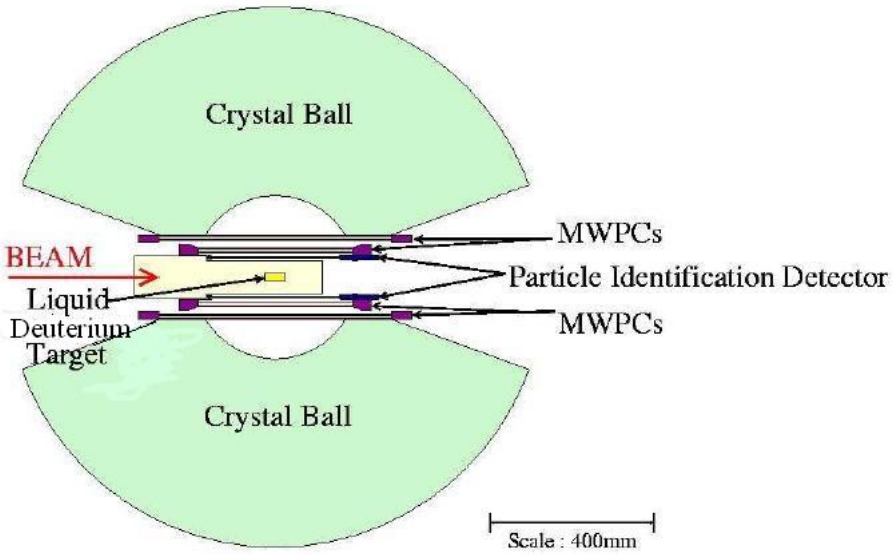

Figure 3.6: A transverse view of the Crystal Ball showing the sub detectors inside it. A liquid deuterium target is also located at its center.

photon energy from the Crystal Ball is considered quite precise and the energy resolution is taken as

$$\frac{\sigma_E}{E} = \frac{2.05\%}{E(\mathrm{GeV})^{0.36}}. \tag{3.4}$$

Because of the high granularity of the Crystal Ball it also has a good position resolution. For hadrons and charged particles, the positional resolution is not optimal as the hadronic shower has less transverse extension. Thus for charged particles other additional detectors are required. Some of the important properties of the Crystal Ball are listed in Table 3-2.

3.4 Particle Identification Detector (PID)

The PID shown in Fig. 3.8 is a cylindrical detector with 10 cm inner diameter around the beam axis centered on the target within the Crystal Ball. It is comprised of 24 plastic scintillators each with the size 31 cm $\times$ 1.3 cm $\times$ 0.2 cm. Optical isolation between each scintillator is achieved by wrapping each individually in a foil. Each of these scintillators is connected to a Hamamatsu R1635 photomultiplier tube of thickness 10 mm. The PID is installed inside the Crystal Ball for the

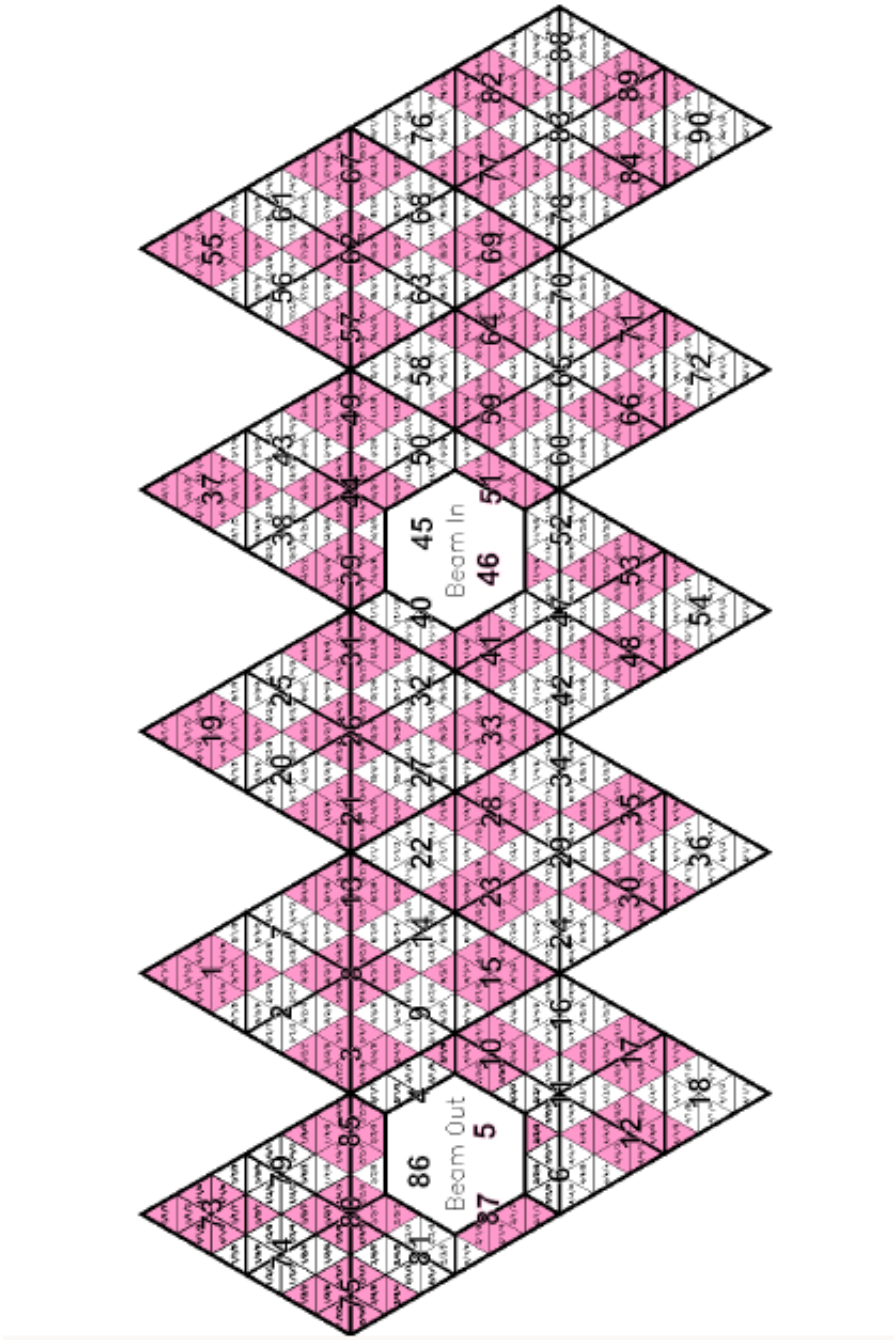

Figure 3.7: The two-dimensional Mercator-like projection of CB Crystals. It shows 90 shaded and unshaded groups of rectangles each containing eight crystals. It also shows the geometry of CB as there are 20 major triangles each of which is made of four minor triangles and each minor triangle contains nine crystals. The ‘beam in’ and ‘beam out’ hole is also visible.

Azimuthal angular acceptance	$0^\circ \leq \phi \leq 360^\circ$
Polar angular acceptance	$20^\circ \leq \theta \leq 160^\circ$
Azimuthal Angular resonance (σ_θ)	$(2 - 3^\circ)/\sin\theta$
Polar angular resolution (σ_ϕ)	2 - 3°
Photon Energy Resolution (σ_E/E)	$\frac{2.05\%}{E(\mathrm{GeV})^{0.36}}$

Table 3-2: Properties of the Crystal Ball.

purpose of identifying charged particles. This detector measures small energy losses (ΔE) in the thin plastic scintillators and a rough variation of the azimuthal angle (ϕ) of the charged particles. By considering this ΔE and the total energy deposited in the Crystal Ball one can identify different charged particles. In our experiment we did not use the output of PID because our analysis involved only neutral particles.

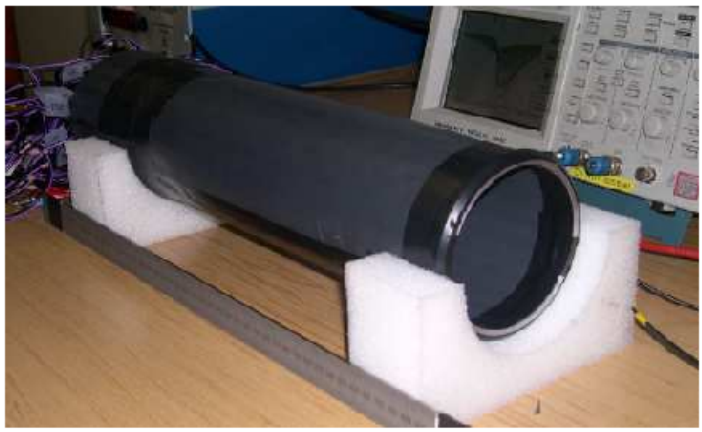

Figure 3.8: The PID before inserting it into position within the CB.

3.5 Multiwire proportional chambers (MWPCs)

There is a charged-particle tracking detector inside the Crystal Ball that surrounds the PID and consists of two cylindrical multiwire proportional chambers (MWPCs), as shown in Fig. 3.9. Each MWPC has three layers: an inner and outer layer that act as a cathode and a middle layer that acts as an anode. The cathode layers are made of 1 m Rohacel covered with 25 μm Kapton film and the anode layer is an array of thin diameter tungsten wire stretched parallel to the cylindrical axis at 2 mm intervals around the circumference [43]. The cathode layers are wound helically in opposite directions at an angle of $\pm 45^{\circ}$ with respect to the wires. A mixture of argon (74.5%), ethane (25%), and freon (0.5%) is filled between the gap (4 mm) of the anode and cathode layers. A high positive voltage of 2300-2500 V is applied between the anode wire and the two cathode layers. The MWPCs cover the complete azimuthal angular range and 21° to 159° in the polar angular range. During the measurements for this work these chambers were turned off. This was of little importance since our analysis involved only the detection of neutral final-state particles.

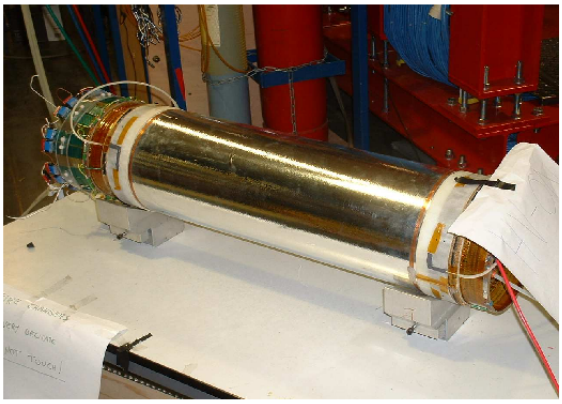

Figure 3.9: The Multiwire Proportional Chamber before inserting it into its position within the CB.

3.6 The TAPS detector

TAPS is a front-end detector for the Crystal Ball as it detects photons or any charged particles that escape from the exit hole of the ball. TAPS was designed and installed with the purpose to study high-energy photon beams as well as neutral mesons [44].

TAPS consists of several hundred hexagonally shaped BaF_2 detectors (see Fig. 3.10) each of length 25 cm (equivalent to 12 radiation lengths) that can be arranged in different configurations. For our experiment, 384 BaF_2 crystals were configured as a forward wall at a distance 180 cm from the center of the Crystal Ball covering the angular range $0^\circ < \theta < 20^\circ$. The combined photon detection set-up for the Crystal Ball and TAPS shown in Fig. 3.11 covers approximately 96% of a complete sphere. Since many particles are emitted in the forward direction, this forward wall is useful to increase the overall detection efficiency.

Figure 3.10: Each individual TAPS BaF_2 detector consists of a hexagonally shaped crystal tube of 25 cm in length with a 2.5 cm cylindrical end connected directly to the photomultiplier tube.

Because of some special characteristics of BaF_2 crystals, they are considered a good choice for the construction of scintillation detectors. First, BaF_2 has a fast rise time of the scintillation pulse; because of this virtue the intrinsic time resolution (about 200 ps) of a single crystal is very good. The accurate particle identification using the time of flight of a particle is made using this essential feature of the BaF_2 crystal. Second, it produces scintillation light with two components: a fast component and a slow component, corresponding to decay times of 0.60 ns (λ = 195 nm and 220 nm) and 620 ns (λ = 310 nm), respectively. These characteristics of BaF_2 crystals provide a means to separate slower hadrons like protons and neutrons from the faster particles like photons, electrons, and pions by finding their corresponding time of flights. Particle identification using this technique of decay of short and long light components is generally called **pulse shape analysis (PSA)**. By integrating the light signals over a short and a long time gate, the pulse shape analysis

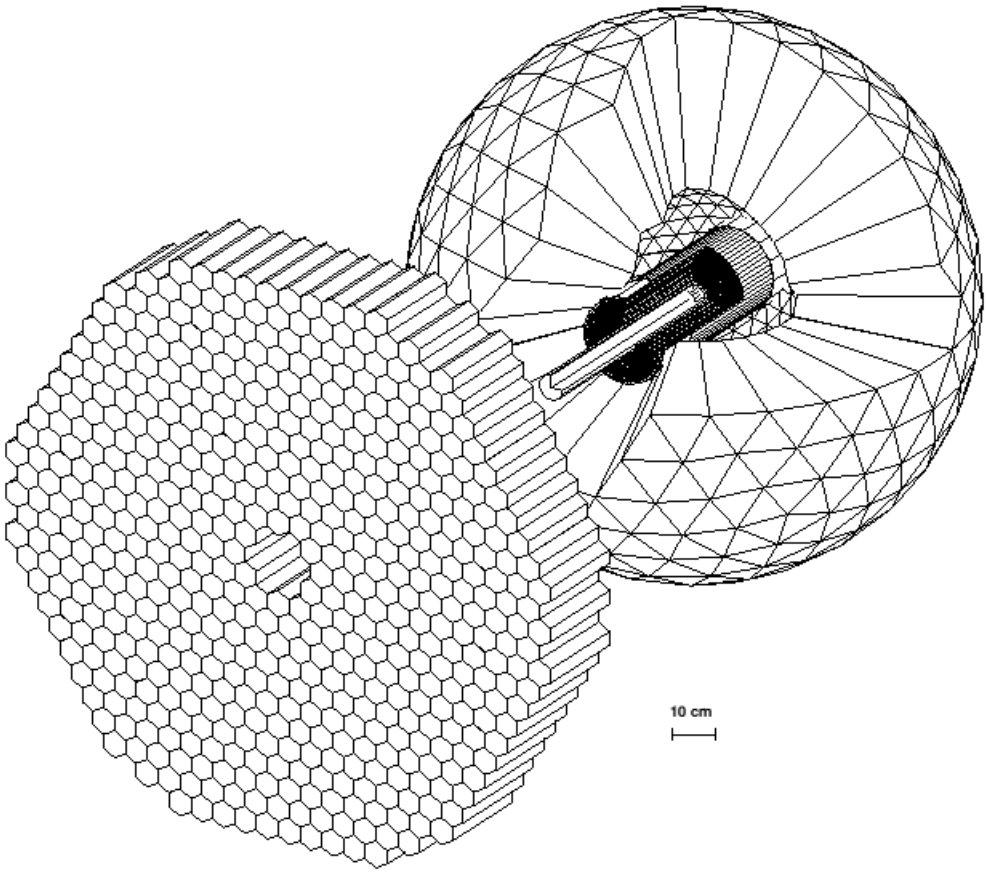

Figure 3.11: The use of TAPS as a forward wall detector at a distance 1.8 m from the CB. The 384 BaF_2 crystals of the TAPS forward wall cover the hole of the CB to cover $\sim$96% of 4π in solid angle.

is carried out. Because the relative intensity of the short component is higher for photons than for nucleons, the ratio of these two components provides a good tool to identify these particles as shown in Fig. 3.12. Third, BaF_2 has a high photon detecting efficiency and energy resolution over a wide range of energies. In addition, because of the high granularity of TAPS, there is a good position resolution.

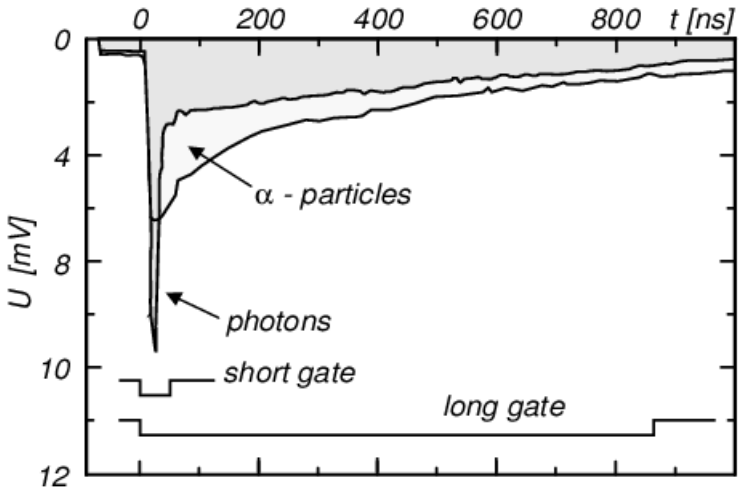

Figure 3.12: A schematic plot of the pulse shape for an α-particle and a photon in TAPS. The larger long component make it possible to distinguish the α-particle and a photon.

Each of the BaF_2 detectors has hexagonal front and back shapes with a cylindrical end part of inner diameter 5.9 cm as shown in Fig. 3.10. The surfaces of the crystals are polished. A UV reflector that is made up of eight layers of PTFE[3] and one layer of thin aluminum foil is wrapped around these crystals. The individual crystals are coupled to a Hamamatsu R2059 photomultiplier tube using silicone grease. In order to provide effective magnetic shielding up to a flux of 0.02 T, the phototubes and the cylindrical section of the crystals are completely surrounded by a magnetic shield. In front of each BaF_2 detector, a hexagonally shaped 5 mm thick NE102A plastic scintillator is installed so as to distinguish between charged and neutral particles. These are called veto detectors. In our work the output of these detectors was not included. Some of the important

[3]Polytetrafluorethylene

properties of the TAPS detector are summarized in Table 3-3.

Distance from the center of CB	1.80 m
Polar angular acceptance	$2^\circ \leq \theta \leq 20^\circ$
Time resolution	0.5 ns FWHM
Angular resolution (σ_ϕ)	0.7° FWHM
Energy Resolution (σ_E/E)	$\frac{3.7\%}{E(\mathrm{GeV})^{1/4}}$

Table 3-3: Detection properties of TAPS.

3.7 The target system

For our work, the target was liquid deuterium (LD_2) contained in a cylindrical cell made of Kapton. The target cell had length 4.8 cm and it was surrounded by eight layers of super insulation foils (8 μm Mylar, 2 μm aluminum) and a 1 mm CFK vacuum tube (See Fig. 3.13). There was a storage tank of volume 1.0 m^3 to store the liquid deuterium, which was located at the Tagger vault. A gas compressor connected to a liquefier was kept outside the Tagger vault. The liquefier, a storage reservoir for the liquid deuterium, was a rectangular aluminum box at a distance of 1.8 m from the center of the Crystal Ball. A deuterium supply line connected the reservoir in the liquefier to the target cell. The supply line and the target cell were located inside the beam pipe in a reduced pressure of 3×10^{-7} mbar as shown in Fig. 3.14.

Initially, the deuterium in the storage tank was at a pressure of 1400 mbar. While in operation, about 25% of the deuterium liquefied and the pressure in the storage tank dropped to typically 1080 mbar. Because of this, the temperature might fall below a certain temperature (21 K) for the liquid deuterium. Thus the temperature of the liquid was maintained by a heating system, which

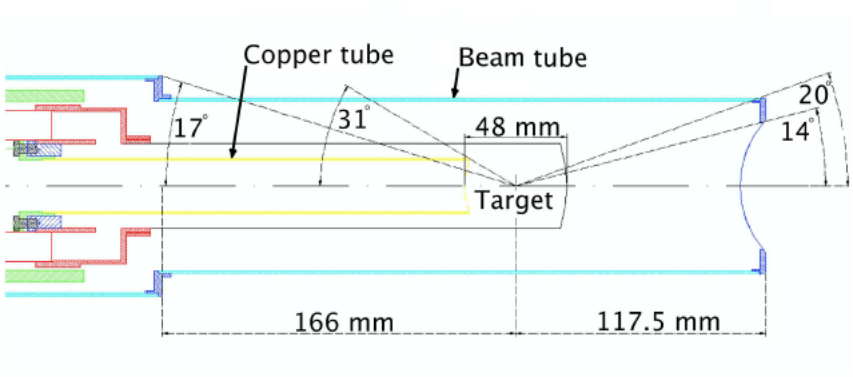

Figure 3.13: Our deuterium target cell was 48 mm long and 40 mm in diameter. The target was surrounded by thin multi-layers made of Kapton and super insulation foils to prevent moisture build-up on the target window.

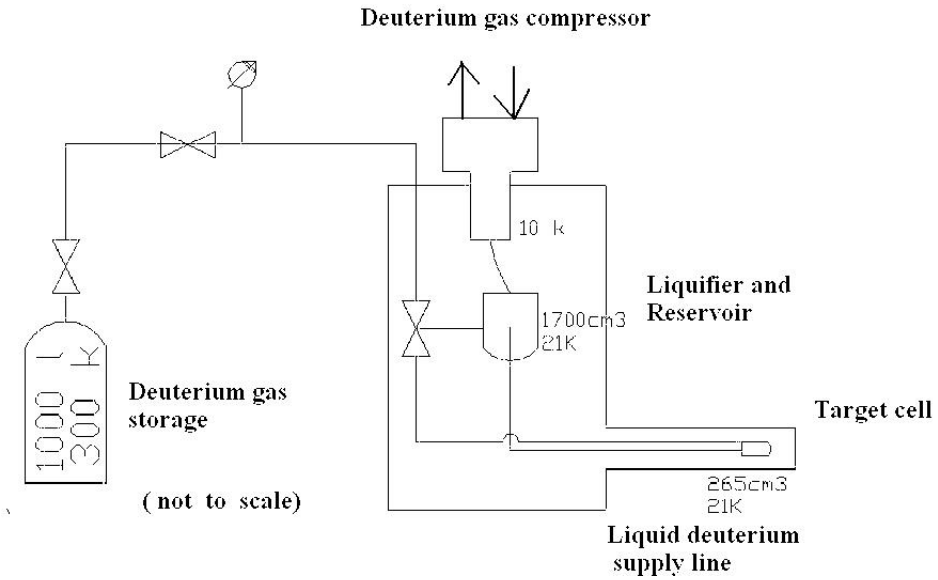

Figure 3.14: The complete liquid deuterium (LD_2) target system. It consists of a gas storage tank (of capacity 1000 liters), a deuterium gas compressor, a liquefier containing the reservoir for the LD_2, and the LD_2 supply line connecting the target cell with the reservoir. During the experiment, this target cell was inserted at the center of the CB.

was turned on and off by a pressure and temperature control system. There are two heaters in the heating system, each of 4 watts, one located on the reservoir and the other on the target cell. The temperature and pressure of the target system were monitored at regular intervals during the experiment. Transverse and longitudinal alignments of the target were done by using a telescope adjusted on the beam axis, a laser and crossed wires inside the Crystal Ball detector. In order to make target-empty background corrections, there was a facility to use the target in its empty mode by switching the button to “Target Empty”. It took 20 s to empty the target cell or refill it with liquid deuterium.

3.8 Electronics

The electronics system performed mainly two tasks: (i) it obtained information from CB, TAPS, Tagger, MWPC, PID, Veto, and (ii) stored the collected information on a computer so that it could be read by the data acquisition system (DAQ). In order to digitize the amplitude and time of the input signals, the signals of the detectors were sent to a charge-to-digital converter (QDC) via a discriminator, and to a time-to-digital converter (TDC). A start and a stop signal above the discriminator threshold was required for the TDC. The experimental triggering electronics acted as a gate for the QDC and provided the start signal for the TDC while the relevant detector gave the stop signal for it.

3.8.1 Tagger electronics

A small electronics card containing two discriminators and a coincidence logic was associated with each of the individual Tagger channels. These discriminators had two thresholds: a low one that determined signal time and a higher one that determined if the signal was sufficiently large to result from an incident electron. Each individual Tagger channel had a timing resolution of $\sim$0.5 ns FWHM because of this dual threshold setup.

Each photomultiplier tube from the focal-plane detectors was attached to a custom designed

amplifier discriminator (A/D) [41]. High voltage (HV) was distributed to the photomultiplier electrodes through a Zener stabilizer as shown in Fig. 3.15. The anode signals from each photomultiplier tube were amplified about 10 times and then sent to the dual low-high type of threshold discriminator, which supplied a logic pulse to the relevant TDCs and scalers. When the signals were fed to the TDCs, counting was started. Counting was stopped by a logic pulse from the triggering electronics after delaying it 500 ns. The measurement of the electron event rate for the computation of the photon flux was carried out using the scalers that were not gated by the trigger.

3.8.2 CB electronics

The Crystal Ball photomultiplier tubes were connected in parallel to each other and the output analog signals from each photomultiplier were sent to an active split delay module where each set of 16 crystals formed a group. Three matched outputs were formed from the splitter as shown in Fig. 3.16. One of the output signals was delayed by 300 ns and passed into a sampling ADC that sampled the shape of the signals with a frequency of 40 MHz.

The other output signal was the summed amplitude of all the 672 crystals, which was sent to the energy sum trigger for making trigger decisions. This trigger decision was sent to the ADCs, TDCs, and scalers via the Trigger Control System (TCS). When a positive trigger decision was made, the information was digitized in the ADC and TDC and stored in data for reading.

The last signal was fed into a discriminator that had high and low thresholds of 20 MeV and 2 MeV, respectively. The signal above the high threshold was sent to the trigger decision in the cluster multiplicity and the signal above the low threshold was used to start the TDC and the scalers.

3.8.3 TAPS electronics

Like in the Crystal Ball, an analog output signal from a BaF_2 detector photomultiplier was sent to a Constant Fraction Discriminator (CFD), two Leading Edge Discriminators (LED1,2) and four Charge-to-Amplitude Converters (QAC1-4), as shown in Fig. 3.17. The CFD had a 5-MeV

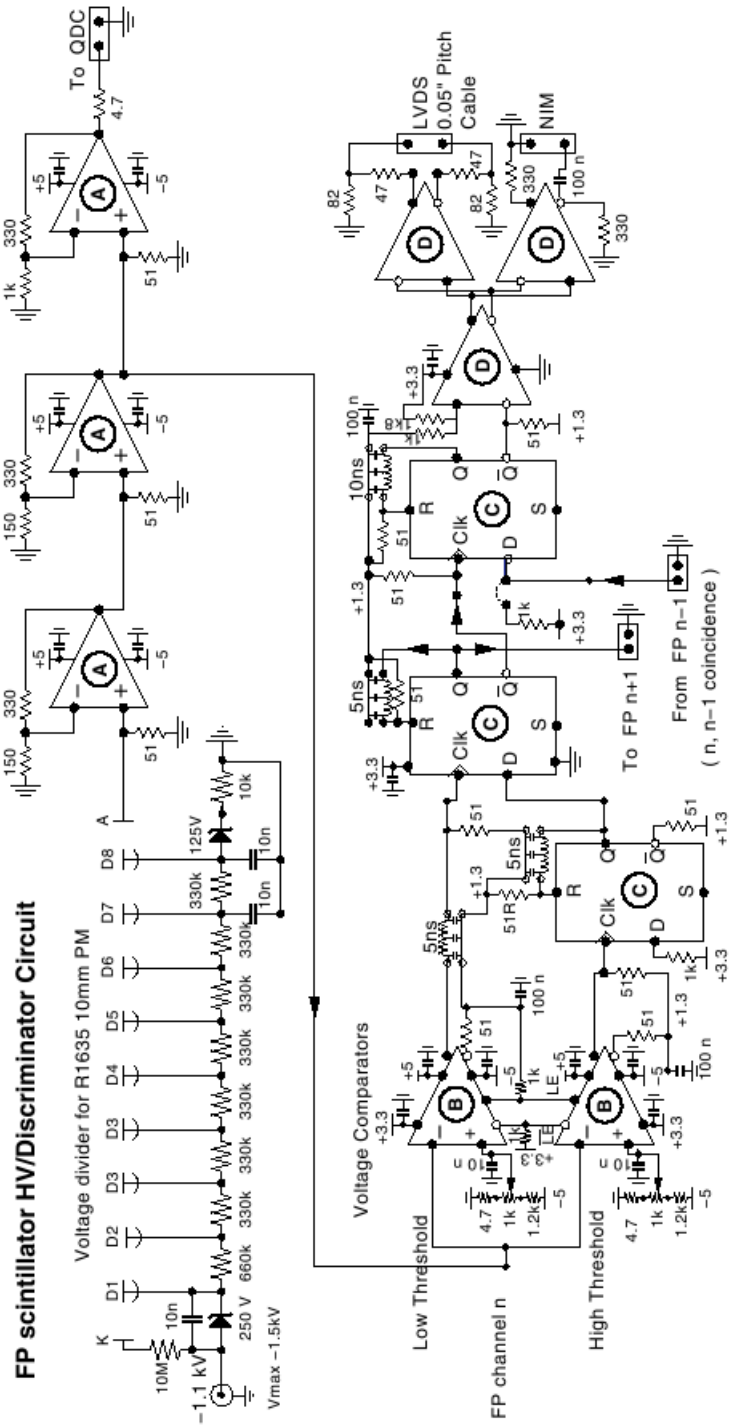

Figure 3.15: Tagger electronics system.

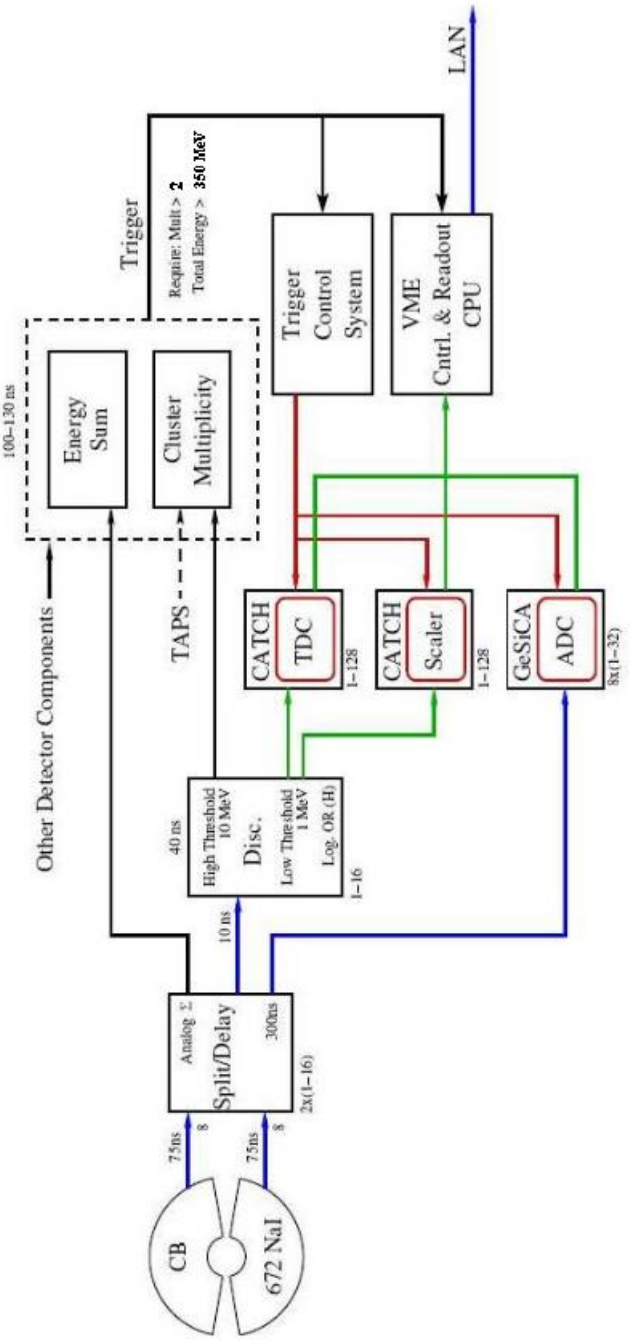

Figure 3.16: The CB electronics system.

threshold. A signal higher than the threshold was considered as a hit in the crystal. It also provided an accurate timing for the pulse with reduced amplitude dependent walk [45]. This accurate timing signal was necessary for making the start signal of the QACs and the Time-to-Amplitude converter (TAC) and also for measuring time in the TDCs. The LED1 had a threshold of 30 MeV. When the signal was higher than this threshold, it was fed into the triggering information. The trigger decision was sent to the TAC and QACs. It stopped the time measurement in the TAC.

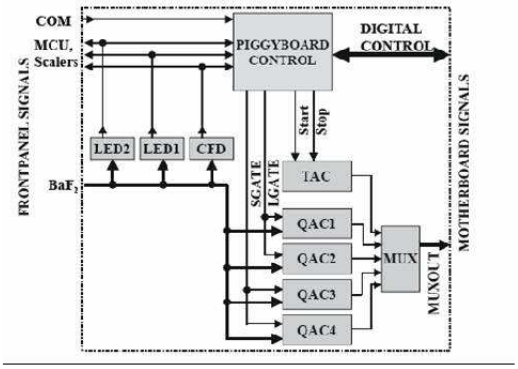

Figure 3.17: The TAPS electronics system.

The analog output from the veto detectors of TAPS was passed to the LED2. The threshold of these detectors was set between the background signal noise and the energy of a minimum ionizing particle incident on the detectors [46]. Any signal higher than this threshold was considered as the signature of a hit in the veto detectors. The QACs measured the fast and slow components of the scintillators response with high and low gains, which resulted in a perfect determination of the pulse shape.

3.8.4 Event triggering

The event triggering system was based on the energy sum of the Crystal Ball and its cluster multiplicity. In our work only the CB was considered for event triggering.

As mentioned in Sec. 3.8.2, the energy sum of the Crystal Ball was obtained by summing the analog energies of all 672 NaI crystals. For the triggering during our experiment, the threshold total energy sum deposited in the CB was 350 MeV. If the total energy deposited in the CB was below 350 MeV, the events were rejected. Generally, the higher energy set up of the threshold energy for the trigger helped to reject the more energetic background.

Our knowledge of cluster multiplicity filtered out unwanted events based on the number of final-state particles. The active splitter in the Crystal Ball electronics divided the 672 NaI crystals readout into 45 logical sectors containing 16 crystals. These 45 outputs added with four sector outputs (128 BaF_2 crystals) from TAPS were designed to record the multiplicity output using the four LeCroy 16 channel CAMAC discriminators, as shown in Fig. 3.18. If the energy deposited in a crystal of any sector exceeded 20 MeV (threshold limit), a multiplicity hit resulted.

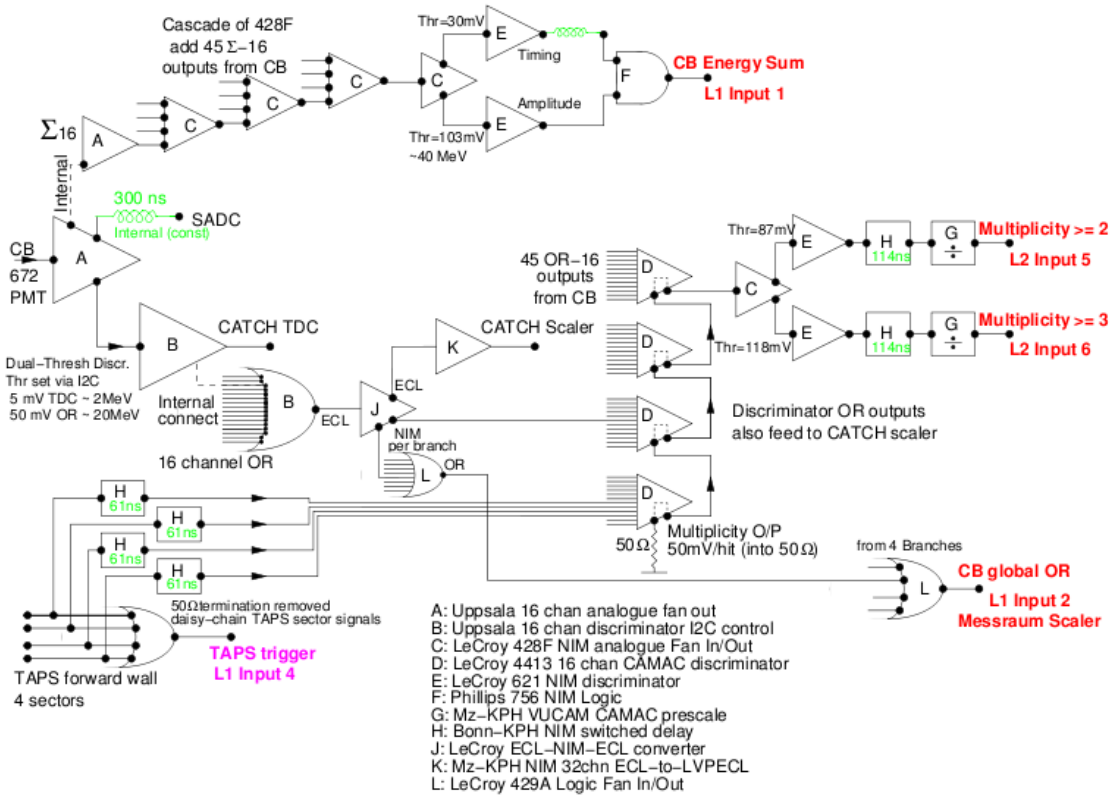

Figure 3.18: Technical scheme of the trigger electronic system.

3.9 Overview of data taking

For this work, data were taken from December 5-21, 2007 with an electron energy up to 1.5 GeV. Test data were also taken from May 11-21, 2007 soon after MAMI-C was commissioned. Because of the low yield of those data, they were not included in our analysis. Table 3-4 summarizes the experimental parameters for the December run.

Data Taking Period	Dec. 5-21, 2007
Total Beam Time	277 hours
Size of Recorded Data	721 GB
Electron Beam Energy	1.508 GeV
Tagged Energy Range	0.4 - 1.4 GeV
Beam Current	10-20 nA
Radiator	10 μm Cu
Diameter of Collimator	4 mm
Target	Liquid Deuterium
Target Length	4.76$\pm$0.03 cm
CB Trigger Multiplicity	2+

Table 3-4: Overview of data taking scheme.

Chapter 4

Data Analysis

This chapter explains the analysis software used for our present work and calibration of energy and time measurement for the CB, TAPS, and the tagger system. It also discusses the method used to reconstruct the particle energy and momentum from the measured energy, and the procedure to subtract the background. The kinematic fitting technique used for the reconstruction and the selection of good events is also described in detail. After the collection of raw data, a calibration of the detector is required in order to convert the stored digital pulse heights and times to the different physical quantities. The values recorded as raw ADC and TDC signals were converted to energies in MeV and time in ns, respectively, and also the cluster algorithms were applied to the data from Crystal Ball and TAPS to form clusters. The final results of the analysis were made from the reconstruction of particle types and four-vectors of each detected hit in all events.

4.1 Analysis software (AcquRoot)

AcquRoot is the analysis software that is used for all of the online and offline analysis of data for Crystal Ball experiments at MAMI. It is an upgraded form of ACQU incorporating with the multi-threaded purely C++ program mainly written by J. R. M. Annand [47]. The new version of AcquRoot (4v0) includes AcquMC and AcquDAQ components. AcquMC is a Monte Carlo reaction kinematics generator and AcquDAQ reads data from some components of the detector system and feeds the data to one or more central event builders. AcquRoot is based on the framework of ROOT [48], which is the CERN C++ based suite of software and libraries. ROOT is based on object-oriented sources, comprised of various types of classes, each performing a specific task. As AcquRoot combines the full ROOT functionality, it makes extensive use of the facilities

offered by ROOT for controlling A2 electronics, data acquisition, storage, retrieval, and analysis. The tree structure of the AcquRoot analyzer is shown in Fig. 4.1.

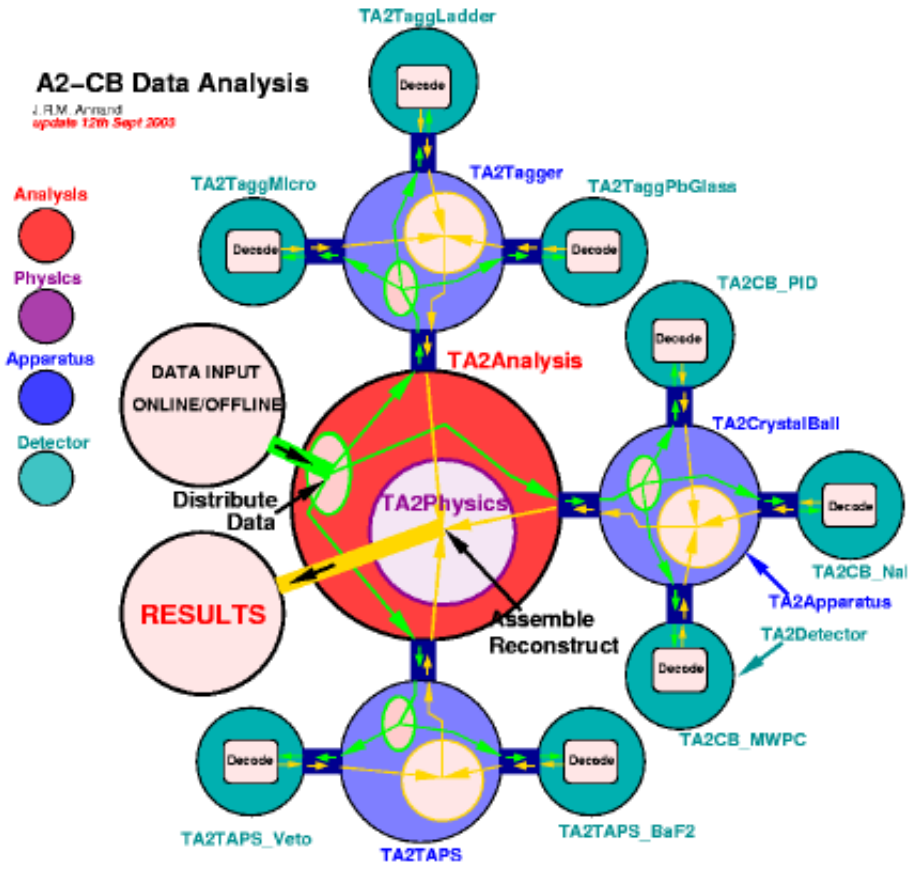

Figure 4.1: The tree structure of AcquRoot Analyzer with its Apparatus, Detector, Physics and Analysis classes. Figure from Ref. [47].

The four circles of different colors on the left-hand side of the figure represent the four important classes involved in AcquRoot. The lowest green circle represents a dedicated class specific to each detector: e.g., Crystal Ball NaI crystals detectors are accounted by the class TA2CB_NaI, TAPS BaF_2 crystals by TA2TAPS_BaF_2, focal plane tagger detectors by TA2TaggLadder, PID by TA2PlasticPID, and so on. These detector classes are responsible for conversion of the digitally stored pulse heights to energies and times. The blue circle, one step higher, represents the three classes that collect information from each of the three subgroups of the detectors. TA2CrystalBall represents the group of detectors related to the

Crystal Ball (e.g., NaI, PID, MWPC). Similarly, TA2TAPS and TA2Tagger represent all the detectors related to the TAPS (e.g., BaF_2, Veto), and the Tagger (e.g., Ladder, Pb Glass, Micro), respectively. These three classes in a group form a class called **TA2Apparatus** which is responsible for the conversion of energies and times into particle types and four-vectors. The pink circle above the blue circle represents a **Physics** class that collects all the information from the three detector systems (such as four-vectors and particle identities) to reconstruct the related events yielding the invariant and missing mass to identify the specific particle. The red circle on the top represents a class called **TA2Analysis** which provides the core of the data analysis system. It decodes the basic ADC, TDC, and Scalers information and passes them to TA2Apparatus.

4.2 Energy calibration process

4.2.1 Tagger energy calibration

The final energy of the tagged electron after producing a photon via bremsstrahlung is determined from the measured position at which the electron hit the focal plane detector, as described by Eq. (3.2) in Sec. 3.2. Because of the application of the large magnetic field (1.834 T), the electron deviates from its path and thus the position at the end of the exit of the Tagger magnet is proportional to its energy. Thus, there is a relationship between the corresponding position of the tagger hit by the electron and the electron's energy. For the Tagger energy calibration, this relationship in a uniform magnetic field is measured by using a computer program. An NMR probe is used to determine and monitor the magnetic field strength of the Tagger.

4.2.2 TAPS energy calibration

The TAPS energy calibration is made using minimum-ionizing cosmic muon radiation. Because all of the BaF_2 detectors in TAPS have the same size and orientation, the energy deposited in them by cosmic ray muons always have minimum ionizing peaks at 37.7 MeV.

For this calibration, special runs were made to measure the energy distribution formed by the passage of cosmic muons through the crystals both before and after the experiments. A typical spectrum obtained from the TAPS energy calibration is shown in Fig. 4.2. The first 'non-zero value' is called the **pedestal**, which corresponds to no true signal and has a value 0 MeV. This pedestal can be seen at the left-most point of the spectrum and is a single-channel peak. In addition to this peak, another peak is essential for the absolute calibration of energy in TAPS. The second reference is provided by the minimum ionizing muon peak at 37.7 MeV. These two points are sufficient for the complete calibration of energy as there exists a linear relationship between the deposited energy and measured channel numbers.

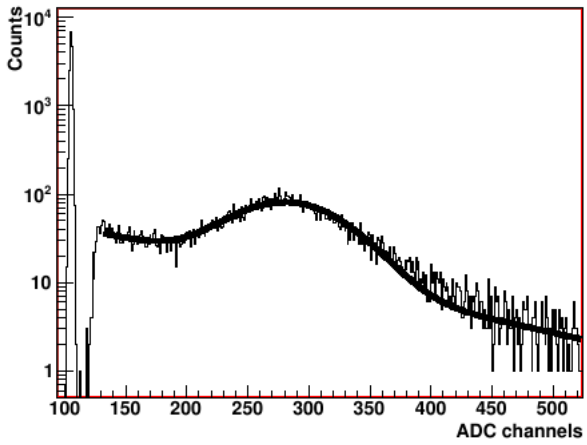

Figure 4.2: A cosmic-ray energy spectrum in a TAPS module with a fit (exponential+Gaussian) showing the narrow pedestal peak at 0 MeV (near ADC channel 100) and the broad cosmic peak at 37.7 MeV (near ADC channel 275). Figure from Ref. [49].

4.2.3 Crystal ball energy calibration

The low-energy photon calibration of the Crystal Ball was done by illuminating the NaI crystals with the help of an Americium-Beryllium ($^{241}\mathrm{Am}/^{9}\mathrm{Be}$) source. As this process produces a certain number of photons of energy 4.38 MeV, the response of the photomultiplier was adjusted to match this energy in the same region of ADC spectra.

Although this matching was made at a far lower energy than those of photons detected in our experiment, it set a rough experimental hardware threshold for all crystals. For much more energetic photons, this low-energy adjustment was not sufficient and a calibration for higher energy photons was done using $\gamma p \to \pi^0 p$.

4.3 TAPS particle identification

As mentioned in Sec. 3.6, the BaF_2 scintillation output contains both fast (0.6 ns) and slow (620 ns) components. This property can be used to distinguish between baryons (e.g., neutrons, protons) and electromagnetic particles (e.g., photons and electrons). These two signals are recorded by two ADCs having two different integration times: a short gate for the short time window (30 ns), and a long gate for the long time window (2 μs). We call E_{short} and E_{long} the energies measured by the short time gate ADC and the long time gate ADC, respectively. The integration for the short time window contains information about the fast component and that for the long time window contains information about both the fast and slow components. The ratio of these two measured energies ($E_{\mathrm{short}}/E_{\mathrm{long}}$) is of order 1 for photons and it is smaller than 1 for baryons. A plot of E_{short} vs. E_{long} is shown in Fig. 4.3.

4.4 Tagger random subtraction

When an energetic electron impinges upon the radiator, it produces a photon. As the electron imparts some fraction of its initial energy to the photon, the deflected electron hits a tagger element in the focal plane that depends on its reduced energy, which starts a TDC clock corresponding to the tagger element. As soon as the photon produced by the electron initiates the experimental trigger (see Sec. 3.8.4), the stop signal for the TDC clock comes into play. This time difference between the start and stop recorded by the TDC is simply related to the time of propagation of the photon to the target and the time

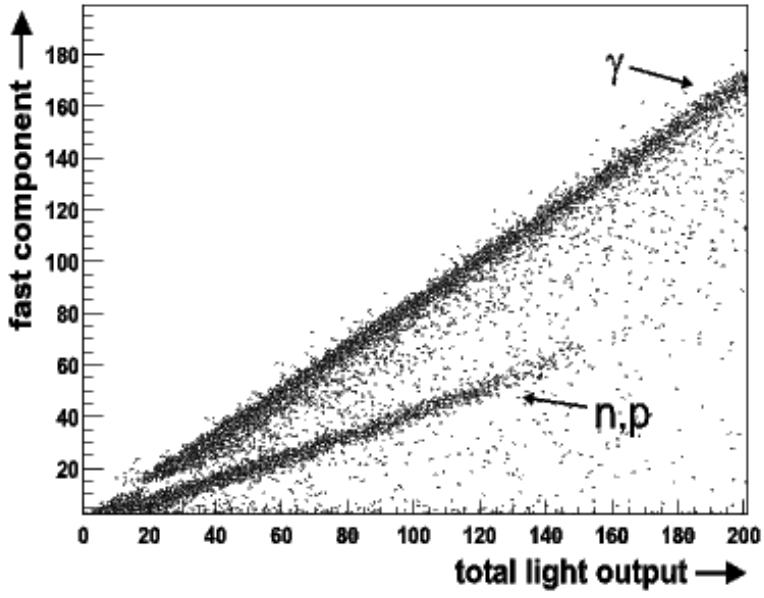

Figure 4.3: TAPS pulse-shape analysis for the identification of baryons and the electromagnetic particles. The energy deposited in the short gate ADC (fast component) and that deposited in the long gate ADC (total light output) are plotted against each other.

taken for the produced particles to make the experimental trigger. This produces a “prompt” peak in each of the Tagger TDC spectra. However, if these electrons are not associated with the photon producing the experimental trigger, then they contribute to the uncorrelated “random” background. A Tagger TDC (TimeOR) spectrum for our experiment is shown in Fig. 4.4. This plot shows the timing of every single photon Tagger hit in every channel relative to the experimental trigger. The prompt peak is at $\sim$105 ns and an almost flat background of random coincidences spreads for the whole 200 ns wide event window.

It is useful to keep uniform cuts on the combined timing spectrum for all the individual tagger TDCs so that the prompt peaks of each element were coincident. The alignment is done by fitting a Gaussian distribution to the prompt peak of each channel for the timing spectra obtained during the tagging efficiency measurements. The number of random coincidences in the Tagger focal plane is small during the tagging efficiency measurements because of the low intensity electron beam and this results in a timing spectrum that is

dominated by the prompt peak. The alignment of all the Tagger TDC spectra is shown in Fig. 4.5, which was obtained by plotting the time for each prompt peak against the corresponding Tagger channel.

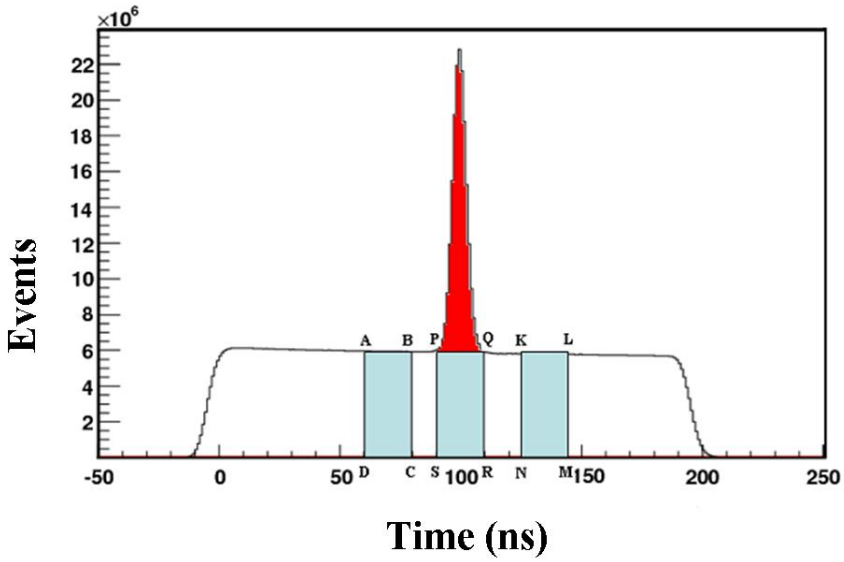

Figure 4.4: A Tagger timing spectrum for all the tagger elements in the focal plane. A coincidence of the CB trigger and the Tagger time gives the prompt peak. The red shaded area (95-115 ns) indicates the prompt events. The region underneath it (PQRS) is the random background.

In order to make a proper random background subtraction, it was necessary to consider three regions of interest in the Tagger TDCs spectrum, as shown in Fig. 4.4:

(i) A prompt region, which normally varied from 95 ns to 115 ns, containing the prompt peak (red shaded) and the random background underneath it (PQRS);

(ii) A random region in the random background to the right of the prompt peak, which normally varied from 125 ns to 145 ns (KLMN);

(iii) A random region in the random background to the left of the prompt peak, which normally varied from 60 ns to 80 ns (ABCD).

Let us define a correction factor (r_{pr}) as the ratio of the areas of the prompt region to

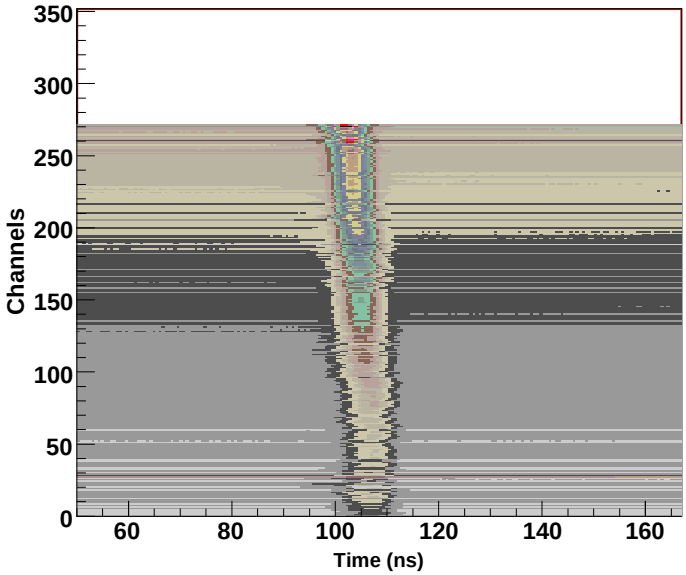

Figure 4.5: The Tagger-time alignment for the data acquisition period.

the sum of the areas of the random regions:

$$r_{\mathrm{pr}} = \frac{\mathrm{PQRS}}{(\mathrm{ABCD} + \mathrm{KLMN})}. \tag{4.1}$$

By using Eq. (4.1), we can calculate the correction factor r_{pr} for each Tagger channel. Figure 4.6 shows a timing spectrum for Tagger channel 25.

The relative time of the photon Tagger hit and the experimental trigger (CB) should be known for every event. Let Y_{prompt} denote the number of prompt counts observed when the time belongs to the prompt region and Y_{rand} denote the number of random counts observed when the times belongs to either of the random regions. Now for each tagger channel and energy bin, the number of counts in the prompt window corrected for random background is expressed as:

$$Y_{\mathrm{subt}} = Y_{\mathrm{prompt}} - r_{\mathrm{pr}} \times Y_{\mathrm{rand}}. \tag{4.2}$$

The uncertainty in Y_{subt} is given by:

$$\sigma_Y = (\sigma_{Y^2_{\mathrm{prompt}}} + r^2_{\mathrm{pr}}\sigma_{Y^2_{\mathrm{rand}}})^{\frac{1}{2}} = (Y_{\mathrm{prompt}} + r^2_{\mathrm{pr}}Y_{\mathrm{rand}})^{\frac{1}{2}}, \tag{4.3}$$

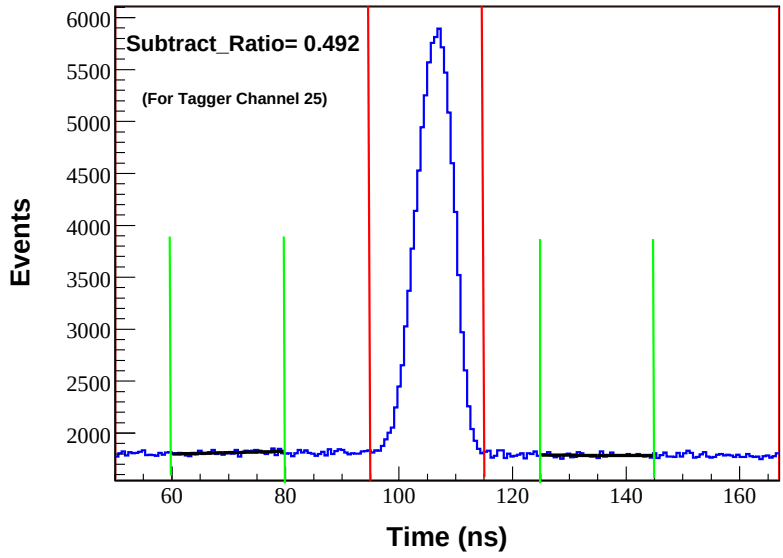

Figure 4.6: Tagger timing spectrum for channel 25 for which the calculated ratio of the random-prompt areas was $r_{\mathrm{pr}} = 0.492$.

where the corresponding σs are the standard deviations in the number of prompt and random counts and are statistical uncertainties, given by the square roots of the corresponding number of counts.

Figure 4.7 shows the application of Eq. (4.2) to the missing mass distribution for the elimination of random background. It is for a particular Tagger channel 51 and the corresponding photon energy 1251.9 MeV. The contribution of background events is represented in Fig. 4.7(a) by the red-filled histogram and the contribution of the coincident events is given by the green-filled histogram. The subtraction of these two histograms is shown fitted with a Gaussian distribution in Fig. 4.7(b).

4.5 Cluster algorithm

When an incident photon strikes a crystal in the Crystal Ball or TAPS detectors, it creates an electromagnetic cascade or shower that consists of a chain reaction of pair production ($\gamma \rightarrow e^{+}e^{-}$), Compton scattering ($\gamma e^{-} \rightarrow \gamma e^{-}$) and bremsstrahlung photon emission. This shower spreads over a group of several adjacent crystals. The group of

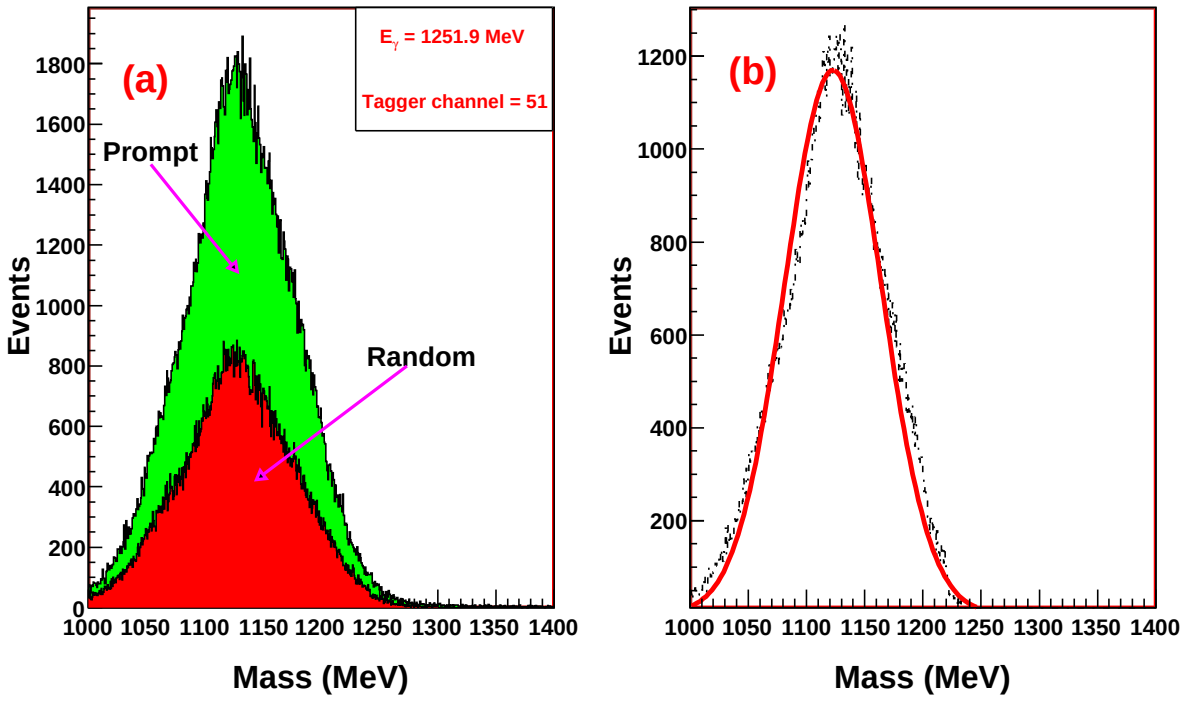

Figure 4.7: Example of random background subtraction of missing mass of K^0 for a typical channel 51 at photon energy E_γ= 1251.9 MeV. (a) The red-filled histogram corresponds to random background events and the green-filled histogram is for prompt coincident events. (b) The resulting histogram fitted with a Gaussian distribution after the subtraction of the two previous histograms using Eq. (4.2).

crystals fired by the same incident photon is called a **cluster**. In the Crystal Ball for 98% of events, the energy is normally deposited in a cluster of 13 NaI crystals as shown in Fig. 4.8(a). The crystal with the largest energy deposited in a cluster is called the **central crystal**. The minimum energy of a cluster should be 25 MeV for the Crystal Ball as below this energy the event is rejected as being below threshold.

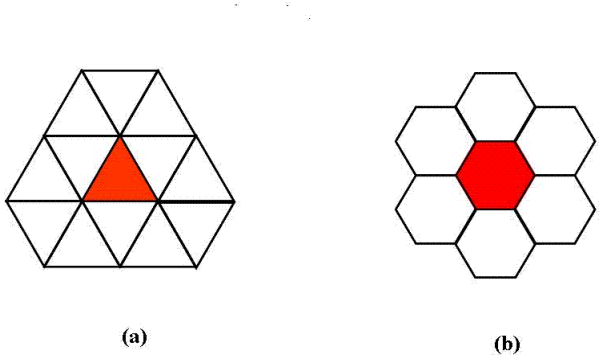

Figure 4.8: The cluster patterns mentioned in the cluster algorithm. (a) A NaI cluster for an ideal event in the CB with the central crystal red in color. The cluster-finding algorithm defines the crystal with the highest energy and surrounded by 12 nearest neighboring crystals as the central crystal in CB. (b) A TAPS cluster for an ideal event in TAPS with the central crystal red in color. The cluster-finding algorithm defines the crystal with the highest energy and surrounded by six nearest neighboring crystals as the central crystal in TAPS.

Similarly, for TAPS there are seven detectors in a cluster with a central crystal surrounded by six nearest neighboring crystals as shown in Fig. 4.8(b). The total minimum energy deposited in a cluster of TAPS should exceed 15 MeV. The position of a cluster in CB or TAPS is calculated using the weighted sum of each of the crystal locations and the energy deposited in the corresponding crystals. For example,

$$X_{\text{cluster}} = \frac{\Sigma_i x_i \sqrt{E_i}}{\Sigma_i \sqrt{E_i}}, \tag{4.4}$$

where E_i and x_i are the energy deposited and the x-coordinate of the i-th crystal respectively. The three direction cosines (α_i) with $i = (x, y, z)$, for a photon can be

expressed as

$$\alpha_i = \cos(\beta_i) = \frac{P_i}{|\mathbf{P}|}, \tag{4.5}$$

where β_i is the angle between the photon's path and the i-axis and P_i is the projection of its momentum onto the i-axis. The corresponding polar angle (θ) and azimuthal angle (ϕ) are related to the direction cosines as:

$$\theta = \cos^{-1}(\alpha_z) = \beta_z, \tag{4.6}$$

$$\phi = \sin^{-1}(\sqrt{(\alpha_x^2 + \alpha_y^2)}. \tag{4.7}$$

When all the photons are reconstructed using the cluster algorithm, a number of quantities can be used to categorize the events. For a particular reaction like $\gamma n \to K^0\Lambda \to 6\gamma n$, the six-cluster events are examined and various quantities related to the photons (such as invariant mass and missing mass, and the total energy and the momentum) can be measured.

4.6 Kinematic fit

In our analysis the kinematic fit is a primary tool for event reconstruction and selection to test all the reaction hypotheses needed. It is used to select the events that are good candidates for each hypothesis being tested. For the better estimation of the background, it has a significant role.

4.6.1 Introduction

Kinematic fitting is a standard method of least-squares fitting with constraints and Lagrange multipliers [50]. The different parameters used for kinematic fits are the measured parameters of the reaction such as total momentum, energies of the clusters, the interaction vertices, and direction of the clusters. In order to determine the good candidates, all the possible combinations of photon clusters for each event are tested. In the kinematic fit, the

constraints are determined by conservation of momentum and energy and the masses of the intermediate particles. Let's suppose $\eta_1, \eta_2, \eta_3, ..., \eta_n$ are measured parameters:

$$\eta = \begin{pmatrix} \eta_1 \\ \eta_2 \\ \eta_3 \\ ... \\ ... \\ \eta_n \end{pmatrix}, \tag{4.8}$$

where η is a set of n measured parameters in vector form. If there are j constraint equations, and using as the first approximation for the kinematic fit:

$$f(\eta) = \begin{pmatrix} f_1(\eta) \\ f_2(\eta) \\ f_3(\eta) \\ ... \\ ... \\ f_j(\eta) \end{pmatrix} = 0. \tag{4.9}$$

Suppose, the initial vector of real values η will not satisfy the constraint equations exactly. Then the initial values are corrected by an amount $\Delta\eta$ so that the kinematic fit tries to fulfill the constraint equation:

$$f(\eta + \Delta\eta) = 0. \tag{4.10}$$

In order to solve the system of equations using the method of least squares, the quantity $\Delta\eta^T G_x^{-1} \Delta\eta$ should be minimized, and where G_x is the weight matrix of the measurement and it is the inverse of the covariance matrix associated with η. This covariance matrix is

just the error matrix of the analysis:

$$G_x = \begin{bmatrix} \sigma_{11}^2 & \sigma_{12}^2 & ... & \sigma_{1n}^2 \\ \sigma_{21}^2 & \sigma_{22}^2 & ... & \sigma_{2n}^2 \\ \vdots & \vdots & ... & \vdots \\ \sigma_{n1}^2 & \sigma_{n2}^2 & ... & \sigma_{nn}^2 \end{bmatrix}. \tag{4.11}$$

The minimization of $\Delta\eta^T G_x^{-1}\Delta\eta$ is done using the method of Lagrange multipliers. For this, let us introduce a Lagrange multiplier, μ with m parameters as:

$$\mu = \begin{pmatrix} \mu_1 \\ \mu_2 \\ \mu_3 \\ ... \\ ... \\ \mu_m \end{pmatrix}. \tag{4.12}$$

Now using Lagrange multipliers and constraints a Lagrange function can be constructed as:

$$L = \Delta\eta^T G_x^{-1}\Delta\eta + 2\mu^T f(\eta + \Delta\eta). \tag{4.13}$$

For the minimum at the certain point, the derivative of L with respect to $\Delta\eta$ and μ must vanish. The parameters such as energies and azimuthal and polar angles are known for each particle in the final state. For this analysis, the minimization process adopted is that of V. Blobel [51].

4.6.2 The pull function

The pull function provides information about systematic uncertainties in the measured values. If there is no systematic uncertainty, the pull function results in a normal distribution centered at zero. The presence of systematic uncertainties causes a shift in the distribution to either positive or negative values. The covariance matrix G_x is related to the resolution of the detectors used in our experiment. The pull distribution is the ratio of the difference

between the measured initial and final (fitted) parameters to the square root of the respective quadratic error differences resulted from the covariance matrix G_x. If η_i and η_f are the set of the initial and the final (fitted) parameters of the measured values respectively, and $\sigma_{\eta_i^2}$ and $\sigma_{\eta_f^2}$ are the corresponding components of the covariance matrix G_x, then the pull of a parameter is defined as

$$\text{pull} = \frac{\eta_i - \eta_f}{\sqrt{\sigma_{\eta_i}^2 - \sigma_{\eta_f}^2}}. \tag{4.14}$$

If the components of G_x (i.e., the uncertainties in the measured parameters) are estimated properly, then the pulls will follow a normal distribution with a mean of zero and a variance of one. In order to find the accuracy of the kinematic fitting used in our analysis, the pull function is a key factor. The pull distributions for energy (E) and for the angular variations theta (θ) and phi (ϕ) of the incoming photon beam are shown in Fig. 4.9 for the reaction $\gamma n \to K^0\Lambda$. These distributions are all centered around 0 and have $\sigma = 1$. A confidence level cut of 15% was applied in the analysis (see Sec. 4.6.3).

4.6.3 Confidence level (CL)

When the components of the covariance matrix are estimated correctly, the quantity $\Delta\eta^T G_x^{-1}\Delta\eta$, will follow a normal χ^2 distribution. The χ^2 distribution plays an important role for measuring the confidence in our analysis. If η_i and η_f are the corresponding initial and final (fitted) values of the set of measured parameters, then the χ^2 value of the fit is defined as [52]:

$$\chi^2 = (\eta_i - \eta_f)^T G_x^{-1}(\eta_i - \eta_f). \tag{4.15}$$

The distribution of χ^2 values of all the possible events is given by the probability density function $f(\chi^2)$ defined as [53]

$$f(\chi^2) = \frac{1}{2^{k/2}\Gamma(k/2)}(\chi^2)^{(k/2)-1}\mathrm{e}^{-1/2\chi^2}, \tag{4.16}$$

where Γ denotes the Gamma function and k is the number of degrees of freedom. The value of $f(\chi^2)$ in Eq. (4.16) will become zero for χ^2 = 0. Figure 4.10(a) shows $f(\chi^2)$

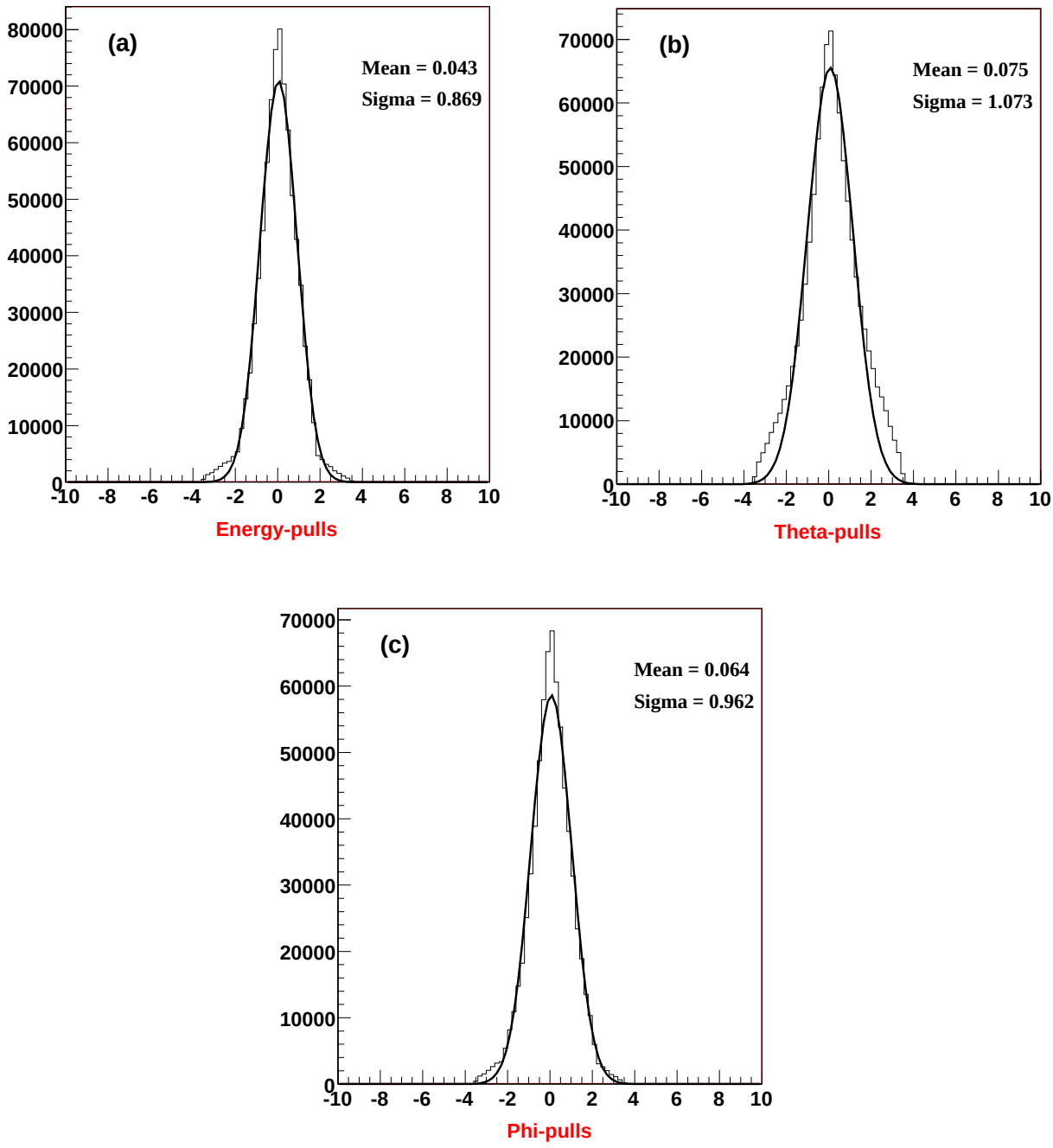

Figure 4.9: The pull distributions for (a) the energy E, (b) the angular variation θ, and (c) the angular variation ϕ of the incoming photon beam in the analysis of $\gamma n \to K^0\Lambda$ using kinematic fitting. When each distribution is fitted with a Gaussian function, the mean is close to zero with standard deviation σ close to one.

for different numbers of degrees of freedom.

The cumulative distribution function $F(\chi^2)$ associated with $f(\chi^2)$ can be defined as

$$F(\chi^2) = \frac{1}{2^{k/2}\Gamma(k/2)} \int_0^{\chi^2} t^{(k/2)-1} \mathrm{e}^{-1/2t} dt, \tag{4.17}$$

where t is a random variable, which is less than or equal to χ^2. Figure 4.10(b) shows the cumulative distribution function for different numbers of degrees of freedom.

The distribution function $F(\chi^2)$ gives the probability (P) as

$$F(\chi^2) = P(x^2 < \chi^2), \tag{4.18}$$

where x^2 is a random variable not larger than χ^2. So we can define a quantity

$$\mathrm{CL}(\chi^2) = 1 - F(\chi^2), \tag{4.19}$$

where $\mathrm{CL}(\chi^2)$ measures the confidence in a measured result and is called **confidence level**.

The confidence level varies from 0 to 1. A high χ^2 corresponds to a confidence level close to 0 and a low χ^2 corresponds to a confidence level close to 1. If the distribution of the measured values is normally distributed around the values calculated by the fit, and the uncertainties in the measured parameters have been estimated properly, then the confidence level distribution will be flat. Figure 4.11 shows the confidence level for all fitted $\gamma n \to K^0\Lambda$ events in our measured data. The events having the largest values of χ^2 in the fit are located near the peak region close to CL = 0 whereas the events with low χ^2 values are distributed close to CL = 1. The distribution of the rest of the events are in the intermediate flat region. As the events near CL = 0 do not satisfy the constraint equations, those events with the large χ^2 are not of interest. These low CL events arise in part from events with partially overlapping photon clusters, or in cases that involve some energy leakage associated with photon clusters in the edge crystals of the CB and TAPS [**?**, 10]. A cut was placed on the confidence level at 15% as shown in the figure, so that events with lower confidence level were discarded.

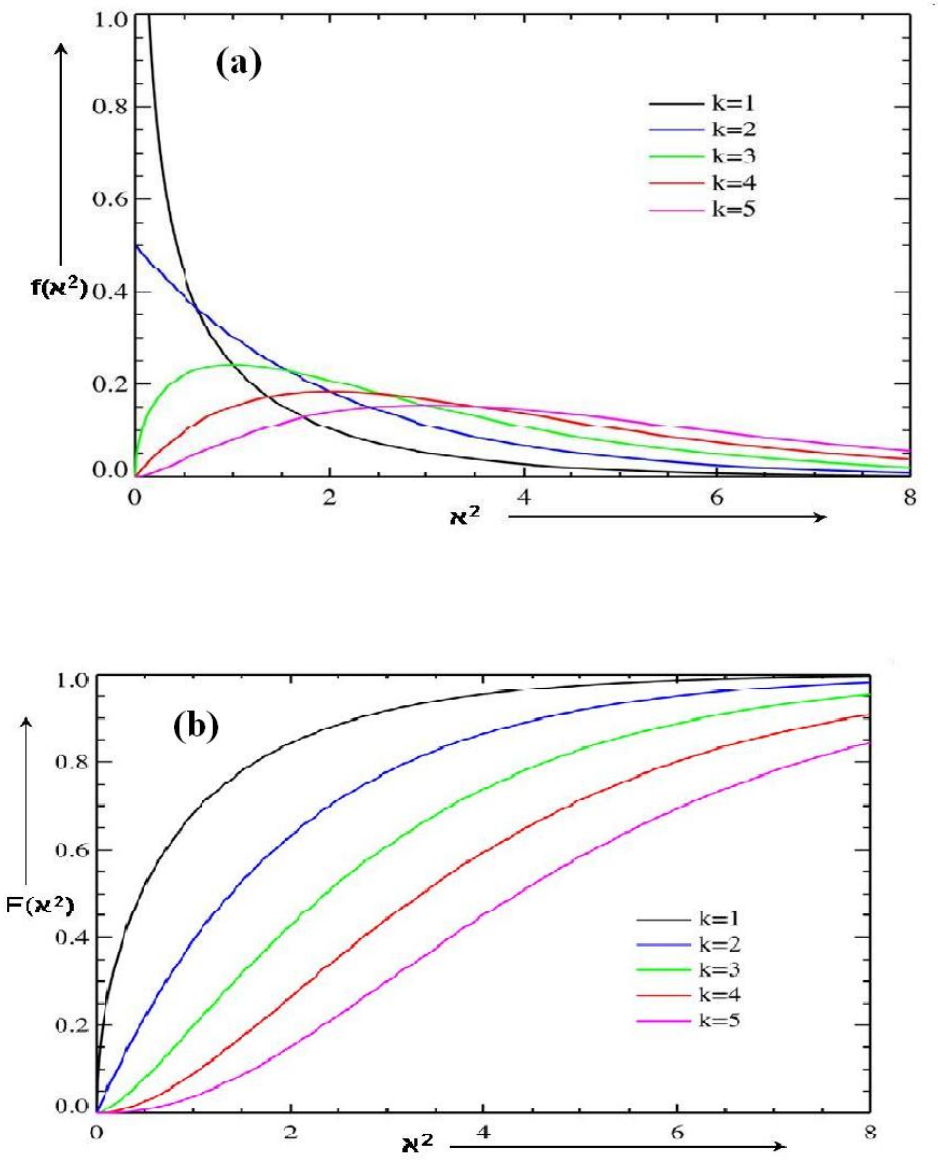

Figure 4.10: (a) Probability density of χ^2 for different numbers of degrees of freedom. The distribution for k = 1 is the curve at the far left and the curves move to the right as the value of k increases. (b) The cumulative distribution of χ^2 for different numbers of degrees of freedom. The curve for k = 1 is the one at the far left, and the curve for k = 5 is at the far right.

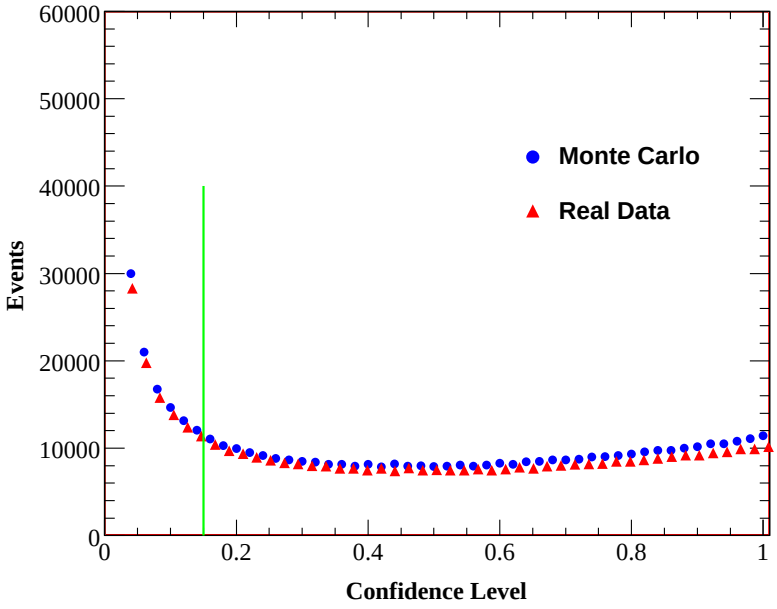

Figure 4.11: The confidence level distributions for Monte Carlo simulation (blue circles) and for real data (red triangles) in the reaction $\gamma n \to K^0\Lambda$. The vertical line shows a CL cut placed at 0.15 for the selection of good events. This cut reduces 33% misidentified events from the real data.

4.6.4 Number of degrees of freedom (NDF)

The number of degrees of freedom (NDF) is a primary factor for determining the confidence level (CL) as explained above. The NDF in an event is defined as

$$\text{NDF} = \text{No. of constraints} - \text{No. of unmeasured quantities.} \tag{4.20}$$

As we consider the momentum of the incident photon to lie along the z-axis, the γn interaction point inside the target is a free variable in the kinematic fit. This z-axis of the interaction point inside the target is taken as the **primary vertex** in our analysis (see Fig. 4.12). Moreover, because of the short lifetimes of the Λ and K^0_S, their decay lengths are comparable to the size of the target, and thus these are also considered as free parameters in the kinematic fit. The variation of the neutron's kinetic energy and the energy deposit in the NaI crystals has not been well defined as nuclear interactions in the NaI crystals are not well known [54]. Thus the energy of the neutron is considered as one of the

unmeasured quantities. If the neutron cluster is completely undetected, the two angles (θ and ϕ) associated with the neutrons are also considered as unmeasured.

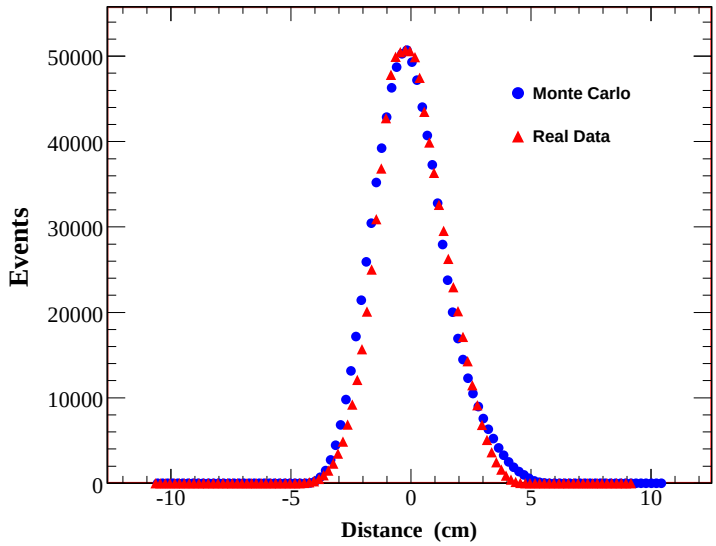

Figure 4.12: The z coordinate of the incident beam for Monte Carlo simulation (blue circles) and for real data (red triangles) in the reaction $\gamma n \to K^0\Lambda$. It is considered as the **primary vertex** in our analysis.

Thus, the number of unmeasured quantities for the six-cluster events of our case is six: the z coordinate of the vertex position, Λ and K^0_S decay lengths, energy of the neutrons, and the two angles of the neutrons. There are mainly nine constraints related to our experiment: four constraints for momentum (p_x, p_y, p_z) and energy conservation, three constraints for the π^0 mass, one for the K^0 mass, and one for the Λ mass. Therefore, the NDF in our case, in which the neutron cluster is undetected, is NDF = $9 - 6 = 3$.

4.7 Event selection

The neutral mesons (π^0, K^0_S) and baryons (Λ) have a very short lifetime, so only the photons resulting from their decay are determined (e.g., $\pi^0 \to 2\gamma, K^0_S \to 2\pi^0, \Lambda \to \pi^0 n$). When a particle decays, its momentum four-vector is conserved. Consequently, the

momentum four-vector of a neutral meson is equal to the sum of the momentum four-vectors of the photons resulting from its decay. For $\gamma n \to K^0\Lambda$, as we considered six photons and a neutron in the final state, only those events containing exactly six clusters were selected. Because of this, it was possible to reduce the amount of data significantly by making a cut on the cluster multiplicity of an event. In our analysis we considered the neutron as an undetected particle. After selecting the events with six clusters, we applied a kinematic fit to select those events with a neutron and three π^0s in the final state.

4.7.1 Particle identification in $\gamma n \to K^0_S\Lambda \to (\pi^0\pi^0)(\pi^0 n) \to 6\gamma n$

As we have seen, the final state we detected was six photons and a neutron. The six photons thus produced in the reaction can be combined into three π^0s in 15 possible ways, as using the following formula

$$N = \frac{n_\gamma!}{2^{n_{\pi^0}} \times n_{\pi^0}!}, \tag{4.21}$$

where N is the total number of combinations, n_γ is the number of photons and n_{π^0} is the number of π^0s. In these combinations, further consideration was given only to those combinations in which the measured two-photon invariant masses were within reasonable limits of the known π^0 mass (134.9 MeV). Figure 4.16 shows a plot of the invariant mass of 2γ for all possible combinations out of six photons in the final state for $\gamma n \to K^0_S\Lambda \to 3\pi^0 n \to 6\gamma n$ to produce a peak around the mass of π^0.

4.7.2 Identification of K^0_S and Λ

In our analysis the momentum four-vectors of detected photons were obtained using kinematic fitting. As explained in Sec. 1.1.2, K^0_S mesons have a very short lifetime, so only the photons resulting from their decays $K^0_S \to 2\pi^0 \to 4\gamma$ were detected. The momentum four-vector of a K^0_S is equal to the sum of the momentum four-vectors of the four photons resulting from its decay. The K^0_S events were identified by constructing the invariant mass of the four photons. Since all six photons in the final state are indistinguishable, it must

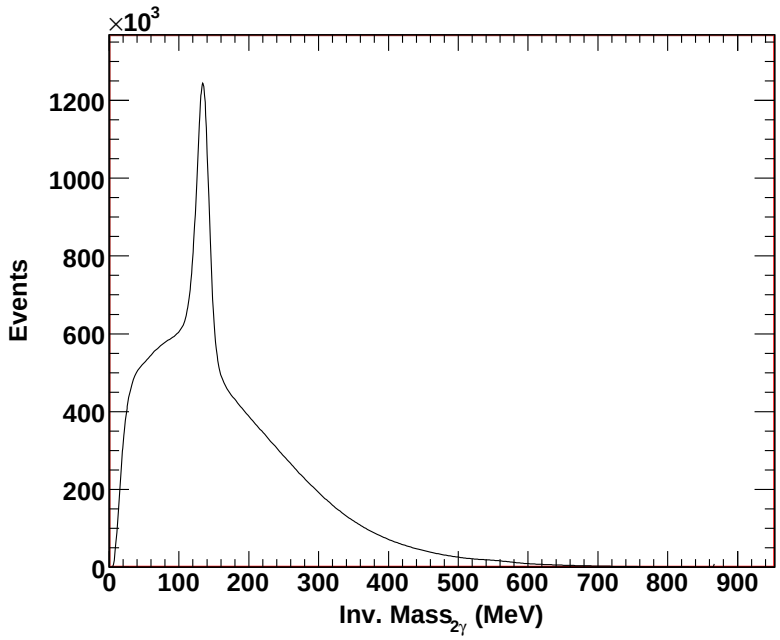

Figure 4.13: The invariant mass of 2γ for all combinations of two out of six photons in the final state for $\gamma n \to K^0_S \Lambda \to 3\pi^0 n \to 6\gamma n$. The invariant mass of 2γ gives a peak around the mass of π^0.

be determined which four photons came from the decay of the K^0_S and which two photons came from the decay of the Λ (as $\Lambda \to \pi^0 n \to 2\gamma n$). The invariant masses from each combination of four photons were compared, and the combination with an invariant mass closest to the K^0_S mass was assigned as coming from the K^0_S decay.

The notation $M_{4\gamma}$ refers to the invariant mass of the four photons. Then the invariant mass squared is given as

$$M^2_{4\gamma} = \left(\sum_{i=1}^{4} P_{\gamma i} \right)^2, \tag{4.22}$$

where $P_{\gamma i}$ is the momentum four-vector $(E_{\gamma i}, \mathbf{P}_{\gamma i})$ of the ith photon determined using kinematic fitting as described in Sec. 4.6. Figure 4.14 shows the distribution of invariant mass for the four photons identified as coming from K^0_S decay in the reaction $\gamma n \to K^0 \Lambda$. There is excellent agreement between the real data and the Monte Carlo simulated events (see Sec. 4.8).

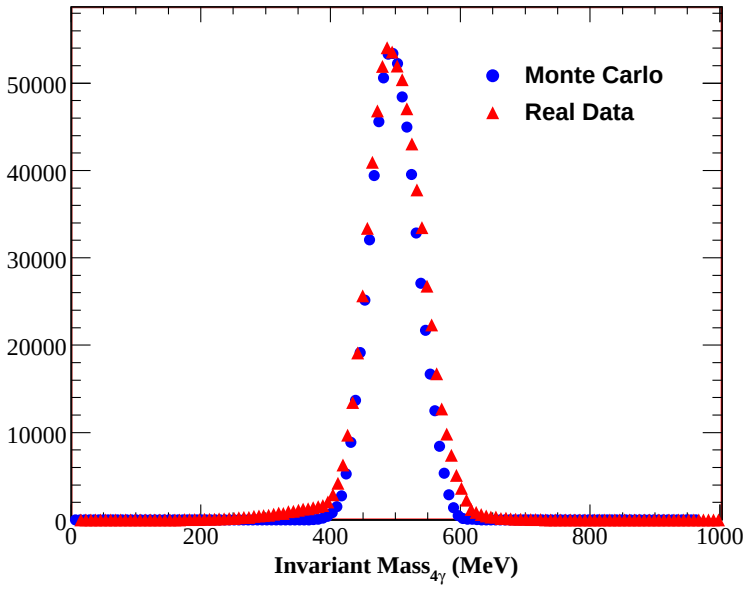

Figure 4.14: The distribution of invariant mass for the four photons identified as coming from $\gamma n \to K^0\Lambda$ followed by $K^0_S \to 2\pi^0 \to 4\gamma$. The peak is near the mass (497.6 MeV) of the neutral kaon.

The notation $MM_{4\gamma}$ refers to the missing mass of the four photons. For the reaction $\gamma n \to K^0\Lambda$, all information about the initial state was available: the energy of the incident photon beam and its direction (along the beam axis), and the target nucleon, which was assumed to be at rest. The momentum four-vector of the K^0_S (the four-vector of the four decay photons) was also known. Thus, using the principal of conservation of energy and momentum, the four-vector of the Λ as the missing particle is given by

$$P_\Lambda = P_{\text{beam}} + P_{\text{target}} - \sum_{i=1}^{4} P_{\gamma i}, \tag{4.23}$$

where P_{beam} and P_{target} are the corresponding momentum four-vectors of the incident photon and target nucleon, respectively. For the target nucleon, we assumed $P_{\text{target}} = (M_n, \mathbf{0})$, where M_n is the neutron mass. I.e., we ignored the neutron's Fermi motion in this work. The square of P_Λ gives the missing mass of the four photons $(MM_{4\gamma})$:

$$(MM_{4\gamma})^2 = (P_\Lambda)^2. \tag{4.24}$$

For $\gamma n \to K^0\Lambda$, the missing mass distribution should be at the mass of the Λ (1116 MeV), as shown in Fig. 4.15.

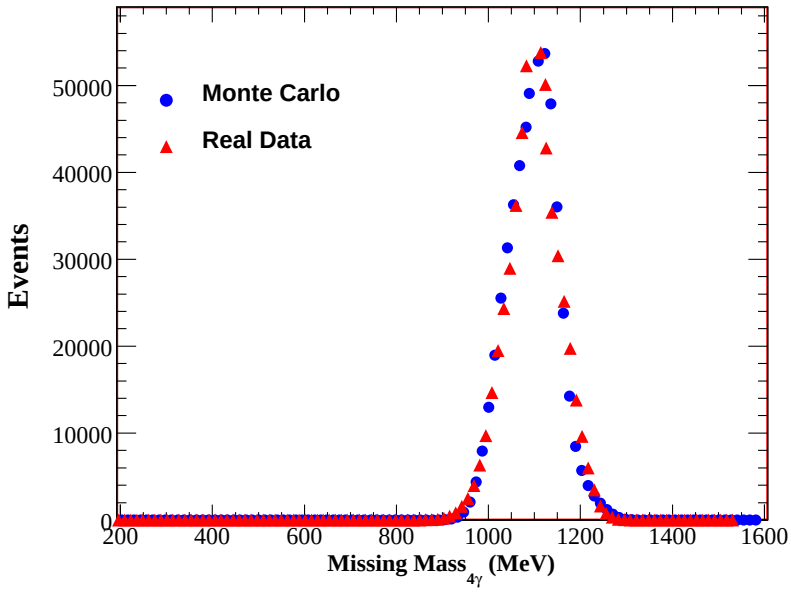

Figure 4.15: The distribution of missing mass for the four photons clusters identified as coming from $\gamma n \to K^0\Lambda$ followed by $K^0_S \to 2\pi^0 \to 4\gamma$. The peak is near the mass (1115.7 MeV) of the Λ hyperon.

4.7.3 Identification of a neutron by missing mass

In the reaction $\gamma n \to K^0_S\Lambda \to (\pi^0\pi^0)(\pi^0 n) \to 6\gamma n$, we just mentioned that the neutron is an undetected particle; however, it can be reconstructed by using the missing mass principal as described in Sec. 4.7.2. As the momentum four-vectors of the incoming photon beam, the target neutron, and the six final-state photons are known, the four-momentum of the missing neutron is given by

$$P_{\text{neutron}} = P_{\text{beam}} + P_{\text{target}} - \sum_{i=1}^{6} P_{\gamma i}. \tag{4.25}$$

The missing mass-squared of the six photons in the final state is obtained by squaring the four-vector P_{neutron} as

$$(MM_{6\gamma})^2 = (P_{\text{neutron}})^2. \tag{4.26}$$

In Fig. 4.16, which shows the missing mass of the six photons, there is a distinct peak at the mass of the neutron (940 MeV) as expected.

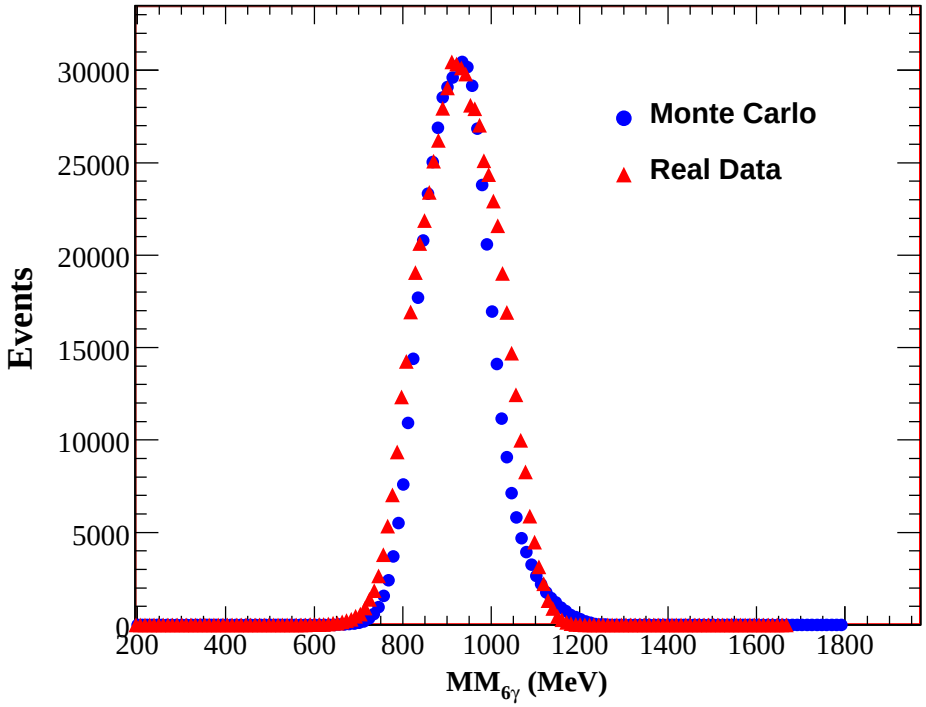

Figure 4.16: The distribution of missing mass of the six photons identified as coming from $\gamma n \to K^0_S \Lambda \to 3\pi^0 n \to 6\gamma n$. The peak is near the mass (939.6 MeV) of the neutron.

4.7.4 Best pion combination of the four photons from K^0_S

The invariant mass of four photons gives the mass of K^0 as described in Sec. 4.7.2, and these four photons are assumed to be from the decay of two π^0s. If the latter is true then some combination of the masses of the photon pairs made out of the four photons $(\gamma_1\gamma_2, \gamma_3\gamma_4)$ must be close to the pion mass. If more than one combination satisfies this criterion, the combination selected was the one minimizing the equation

$$\Delta M = \sqrt{(M_{\gamma_1\gamma_2} - M_{\pi^0})^2 + (M_{\gamma_3\gamma_4} - M_{\pi^0})^2}. \tag{4.27}$$

This condition is called the **best pion combination**. Figure 4.17 shows a two-dimensional view of the invariant mass of these selected pion pairs obtained from the best combination

of the four photons, and Fig. 4.18 is a one-dimensional view of the invariant mass of these selected pion pairs.

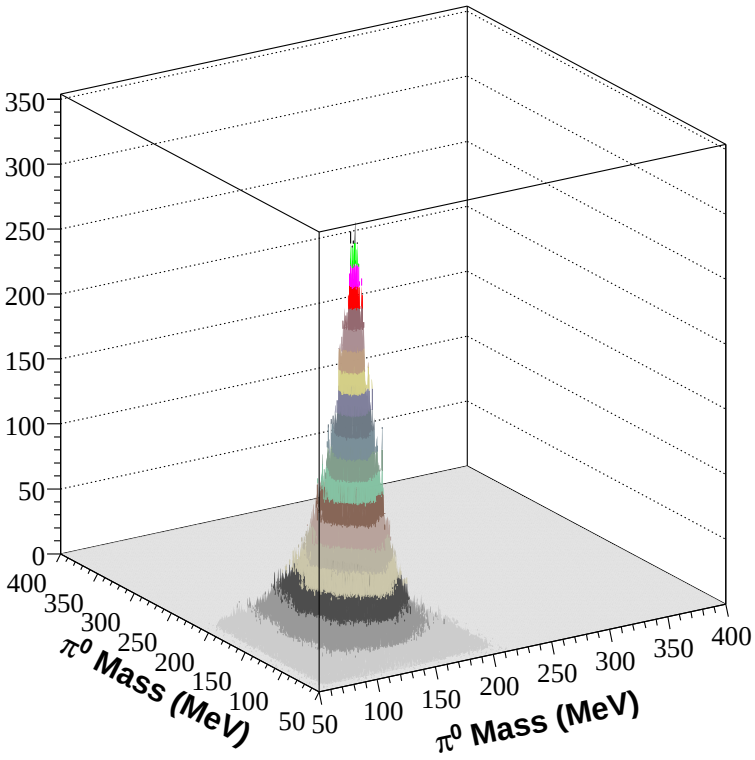

Figure 4.17: Two-dimensional plot of invariant masses of the reconstructed π^0 pairs from the decay of K^0 as $K^0 \to 2\pi^0 \to 4\gamma$ for $\gamma n \to K^0\Lambda$ events.

4.8 Monte Carlo simulation

There are two main objectives of using the Monte Carlo simulation: first, to determine the efficiencies of the detector system for $\gamma n \to K^0\Lambda$ and second, to estimate the major background contributions to the measurements from other possible reactions such as $\gamma p \to K^0\Sigma^+$, $\gamma N \to \eta N$, and $\gamma N \to 3\pi^0 N$.

The Monte Carlo simulation package for our analysis consists of two parts: one part that generates the events, and the other part that tracked the particles through the experimental set-up.

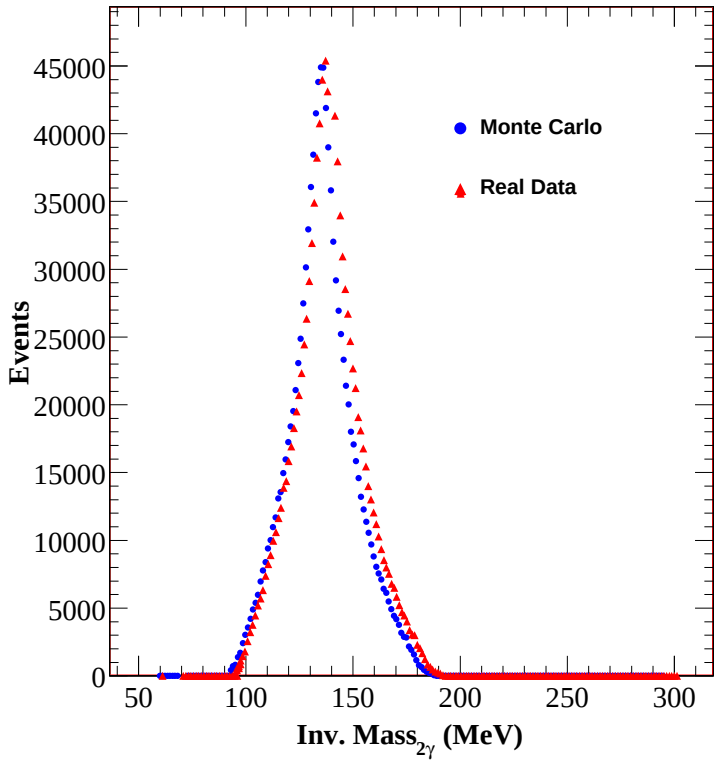

Figure 4.18: The distribution of invariant mass for the two photons identified as coming from $K_S^0 \rightarrow 2\pi^0$ followed by $\pi^0 \rightarrow 2\gamma$. The peak is near the mass (135.0 MeV) of the neutral pion.

For the first step, a code is used to generate the kinematics of the reactions, or reaction chains. For the incident photon, the actual beam parameters were obtained from the real beam events of real experimental data. The beam parameters are beam energy of incident photon, target dimension, spot size at the target, the beam divergence, the final state of the particles, whether they decay or not, and what they decay into. The output of this step is a file that contains the vertex position, the kinematic variables of the beam particle, and the kinematic variables of all the final-state particles for each event.

For the next step, a code based on the simulation package from CERN, GEANT version-3.21, was used for the purpose of tracking [55]. The output from the first event generation process was an input file to this tracking code. The tracking parameters in the code were optimized so that the simulated data mimicked as closely as possible the real data. The geometry of all the detectors of the real experimental set-up such as CB, TAPS, PID, and target, were added in the tracking package. Figure 4.19 shows the design of the CB and TAPS geometry in the Monte Carlo simulation. Because there is no real photon to be tagged for simulation, the Tagger was not included in the package and moreover, it did not directly affect the detection efficiency. The final output of the tracking step was fed to the code "AcquRoot" [47], for the final analysis process. The same code was used to analyze both real and simulated data.

4.9 Estimation of background

As mentioned earlier, we can investigate the experimental background for $\gamma n \rightarrow K^0\Lambda$ using a Monte Carlo analysis. For this purpose we simulated data for various other reactions and analyzed these data using the fitting hypothesis of the reaction $\gamma n \rightarrow K^0\Lambda$. Those events that survived the selection tests for $\gamma n \rightarrow K^0\Lambda$ were counted as backgrounds. (In order for a real event to be accepted as viable $\gamma n \rightarrow K^0\Lambda$ candidate, it should have the highest confidence level for this hypothesis compared to any other hypothesis. Finally,

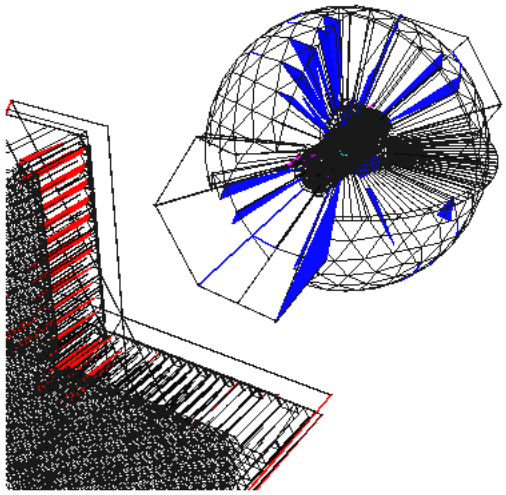

Figure 4.19: Geometry of the CB and TAPS in the Monte Carlo simulation. Figure from Ref. [46].

to be acceptable, it should have CL $>$ 0.15.)

We considered the following possible background reactions: (i) $\gamma p \to K^0\Sigma^+$, (ii) $\gamma n \to K^0\Sigma^0$, (iii) $\gamma N \to \eta N$, and (iv) $\gamma N \to 3\pi^0 N$. The average survival probabilities that the simulated events satisfied the selection tests for $\gamma n \to K^0\Lambda$ are summarized in Table 4-1. By comparison, the average survival probability that simulated $\gamma n \to K^0\Lambda$ events satisfied the selection criteria was about 17%.

4.9.1 Background from $\gamma p \to K^0\Sigma^+$

Events for $\gamma p \to K^0\Sigma^+$ were simulated using the Monte Carlo analysis. The threshold photon energy for this reaction in the laboratory frame is 1.0475 GeV. Since the threshold photon energy for $\gamma n \to K^0\Lambda$ is 0.914 GeV, the background from $\gamma p \to K^0\Sigma^+$ is expected at slightly higher photon energies in the data set. The $K^0\Sigma^+$ final state is obtained through the following sequential decays:

$$\gamma + p \to K^0_S + \Sigma^+ \tag{4.28a}$$

background channels	**survival probability**
$\gamma p \to K^0\Sigma^+$	2.15%
$\gamma n \to K^0\Sigma^0$	0.76%
$\gamma N \to \eta N$	0.38%
$\gamma N \to 3\pi^0 N$	1.02%

Table 4-1: Survival probability for several background reactions to $\gamma n \to K^0\Lambda$ calculated from Monte Carlo analysis.

and K_S^0 further decays into $2\pi^0$, which ultimately produces four photons exactly in the same way as for $K_S^0\Lambda$:

$$K_S^0 \to \pi^0\pi^0 \to 4\gamma. \tag{4.28b}$$

Similarly, the Σ^+ further decays to a π^0 and a proton, and the π^0 further decays to 2γ as:

$$\Sigma^+ \to \pi^0 p \to 2\gamma + p. \tag{4.28c}$$

Thus, the decay chain for this background reaction is:

$$\gamma p \to K_S^0\Sigma^+ \to (\pi^0\pi^0)(\pi^0 p) \to 6\gamma p. \tag{4.29}$$

We therefore identified this reaction as the 6-cluster events in which the final state consisted of six photons and a missing proton, and the missing mass of the K_S^0 corresponded to the Σ^+ mass.

In addition to studying $\gamma p \to K^0\Sigma^+$ as a background for $\gamma n \to K^0\Lambda$, we also analyzed 6-cluster events in our data to measure the cross section for $\gamma p \to K^0\Sigma^+$. Since published

cross-section data for this reaction are available [52, 56–58], we could compare our results with previous measurements. Consequently, we used this comparison to check our technique for analyzing $\gamma n \to K^0\Lambda$ events. The analysis of $\gamma p \to K^0\Sigma^+$ was carried out in a similar way as for $\gamma n \to K^0\Lambda$. Details of our analysis of $\gamma p \to K^0\Sigma^+$ are described in Appendix A.

4.9.2 Background from $\gamma n \to K^0\Sigma^0$

Events for $\gamma n \to K^0\Sigma^0$ were simulated using the Monte Carlo analysis. The threshold photon energy for this reaction in the laboratory frame is 1.050 GeV. The background from this reaction is expected at slightly higher photon energies in the data set. The $K^0\Sigma^0$ final state is obtained through the following sequential decays:

$$\gamma + n \to K^0_S + \Sigma^0 \tag{4.30a}$$

and K^0_S further decays into $2\pi^0$, which ultimately produces four photons:

$$K^0_S \to \pi^0\pi^0 \to 4\gamma. \tag{4.30b}$$

Similarly, the Σ^0 further decays to a Λ and a γ, and the Λ further decays to a proton and a γ as

$$\Sigma^0 \to \Lambda\gamma \to \pi^0\gamma p. \tag{4.30c}$$

Thus, the decay chain for this background reaction is

$$\gamma p \to K^0_S\Sigma^0 \to (\pi^0\pi^0)(\Lambda\gamma) \to (\pi^0\pi^0)(\pi^0 n\gamma) \to 7\gamma p. \tag{4.31}$$

This reaction should then produce 7-cluster events in which the final state consists of seven photons with a missing neutron. Most of these events did not survive the selection criteria for $\gamma p \to K^0_S\Lambda$ due to the multiplicity cut requiring six detected photons only. For the 6-cluster events, we required that we could reconstruct three π^0s, with two identified as coming from decay of a K^0_S and their corresponding missing mass consistent with the Σ^0 mass.

4.9.3 Background from $\gamma N \rightarrow \eta N$

Events for $\gamma N \rightarrow \eta N$ were simulated using the Monte Carlo analysis. Since the threshold photon energy for this reaction is 0.706 GeV, the background from this reaction is expected to extend throughout the entire data set. The ηN final state was identified through the following sequential decays:

$$\gamma + N \rightarrow \eta + N, \tag{4.32a}$$

and η further decays into $3\pi^0$, which ultimately produces six photons:

$$\eta \rightarrow \pi^0\pi^0\pi^0 \rightarrow 6\gamma. \tag{4.32b}$$

Thus, the decay chain for this background reaction is

$$\gamma N \rightarrow \eta N \rightarrow (\pi^0\pi^0\pi^0)N \rightarrow 6\gamma N. \tag{4.33}$$

This reaction should then produce 6-cluster events in which the final state consists of six photons coming from the decay of three π^0s with a missing nucleon. These were rejected by removing all events with a 6γ invariant mass in the range 510-580 MeV.

4.9.4 Background from $\gamma N \rightarrow 3\pi^0 N$

Events were also simulated for the direct $3\pi^0$ production reaction $\gamma N \rightarrow 3\pi^0 N$. As the threshold photon energy of this reaction is 0.492 GeV, background from this reaction is expected in the entire range of the data set. The reaction chain for this background reaction is

$$\gamma N \rightarrow \pi^0\pi^0\pi^0 N \rightarrow 6\gamma N \tag{4.34}$$

This reaction should then produce 6-cluster events in which the final state consists of six photons coming from the decays of three π^0s with a missing nucleon. Unlike for $\gamma N \rightarrow \eta N$, these events could not be rejected on the basis of the $3\pi^0$ invariant mass.

4.10 Some methods for background subtraction

In order to extract good $K^0_S\Lambda$ events from the kinematically fitted data, as much background as possible needed to be removed. The next two subsections describe the methods that we used to extract good events in our analysis.

4.10.1 Selection of the highest probability among all reaction channels

As already mentioned in Sec. 4.6, the kinematic-fitting technique was applied to test various hypotheses. Each event was tested simultaneously for five hypotheses: (i) that the event was from $\gamma n \to K^0\Lambda$, (ii) that it was from $\gamma p \to K^0\Sigma^+$, (iii) that it was from $\gamma n \to K^0\Sigma^0$, (iv) that it was from $\gamma N \to \eta N$, and (v) that it was from $\gamma N \to 3\pi^0 N$. The selection of good events was made by comparing the confidence level (CL) of each hypothesis. The events having the highest CL for a given hypothesis were selected as good events for the corresponding reaction. The events surviving these cuts were passed on for further analysis.

4.10.2 Final background subtraction method

All considered background reactions have at least a 6γ final state so all of these reactions were considered as 6-cluster events in the analysis. For the real data, the backgrounds due to these reactions were estimated using a Monte Carlo simulation and the measured number of $K^0\Sigma^+$, $K^0\Sigma^0$, ηN, and $3\pi^0 N$ events.

Let us define a constant ratio factor $\varepsilon_{\rm MC}(XY/SP)$ known as **contamination ratio** for the determination of background subtraction using the Monte Carlo simulation as:

$$\varepsilon_{\rm MC}(XY/SP) = \frac{N(SP)_{\{\gamma N \to XY\}}}{N(SP)_{\{\gamma N \to SP\}}}, \tag{4.35}$$

where

$$
\begin{aligned}
N(SP)_{\{\gamma N \to XY\}} &= \text{number of Monte Carlo events generated for } \gamma\mathrm{N} \to \mathrm{SP} \\
&\quad \text{that satisfied the selection tests for the hypothesis} \\
&\quad \gamma N \to XY, \\
N(SP)_{\{\gamma N \to SP\}} &= \text{number of Monte Carlo events generated for } \gamma\mathrm{N} \to \mathrm{SP} \\
&\quad \text{that satisfied the selection tests for the hypothesis} \\
&\quad \gamma N \to SP.
\end{aligned}
$$

Thus, we can define $\varepsilon_{MC}(K^0_S\Lambda/K^0_S\Sigma^+)$ as the ratio of the fraction of Monte Carlo simulated events for $\gamma p \to K^0\Sigma^+$ that survived the selection tests for $\gamma n \to K^0_S\Lambda$ to the fraction of Monte Carlo simulated events for $\gamma p \to K^0_S\Sigma^+$ analyzed as $\gamma p \to K^0_S\Sigma^+$. Ratios for other reactions can be defined similarly. These ratios are defined for specified energy and angle $(\cos\theta)$ bins. Let us suppose that $N^{K^0_S\Lambda}_{\text{data}}$, $N^{K^0_S\Sigma^+}_{\text{data}}$, $N^{K^0_S\Sigma^0}_{\text{data}}$, $N^{\eta N}_{\text{data}}$, and $N^{3\pi^0 N}_{\text{data}}$ are the corresponding known numbers of $K^0_S\Lambda$, $K^0_S\Sigma^+$, $K^0_S\Sigma^0$, ηN, and $3\pi^0 N$ (correctly identified) in the real data. Then the number of real signal $N^{K^0_S\Lambda}_{\text{signal}}$ events for $\gamma n \to K^0_S\Lambda$ [54] is:

$$
\begin{aligned}
N^{K^0_S\Lambda}_{\text{signal}} = N^{K^0_S\Lambda}_{\text{data}} - N^{K^0_S\Sigma^+}_{\text{data}}\varepsilon_{\text{MC}}(K^0_S\Lambda/K^0_S\Sigma^+) - N^{K^0_S\Sigma^0}_{\text{data}}\varepsilon_{\text{MC}}(K^0_S\Lambda/K^0_S\Sigma^0) - \\
N^{\eta N}_{\text{data}}\varepsilon_{\text{MC}}(K^0_S\Lambda/\eta N) - N^{3\pi^0 N}_{\text{data}}\varepsilon_{\text{MC}}(K^0_S\Lambda/3\pi^0 N).
\end{aligned}
\tag{4.36}
$$

I.e., we can subtract the background events from our analysis and compute the actual number of $\gamma n \to K^0\Lambda$ events.

In addition to the above mentioned background sources, there is another source due to empty target data. It arises due to the interaction of incident photons with the target cell. The method for the empty target subtraction is described in Sec. 4.14.

4.11 Secondary vertex and decay correction for K^0_S and Λ

In our experiment, it was assumed that the initial electromagnetic interaction occurs at the primary vertex where K^0_S and Λ are produced in the reaction $\gamma n \to K^0_S\Lambda$. Because

of their lifetimes, $\tau_{\Lambda} = 0.2632$ ns for Λ and $\tau_{K^0_S} = 0.08935$ ns for K^0_S, these particles can travel a few centimeters from the point at which they were produced before they undergo a weak decay. In order to find the position of the secondary vertex [**?**, 34] (where these particles decay), their momenta must be known. In our analysis, the positions of the secondary vertexes for K^0_S and Λ were reconstructed by using the kinematic fit. If the coordinate of the primary vertex is $(x_{\rm prim}, y_{\rm prim}, z_{\rm prim})$ and the corresponding co-ordinate of the secondary vertex is $(x_{\rm second}, y_{\rm second}, z_{\rm second})$, then the distance traveled by a particle before decay is

$$d = \sqrt{(x_{\rm second} - x_{\rm prim})^2 + (y_{\rm second} - y_{\rm prim})^2 + (z_{\rm second} - z_{\rm prim})^2}. \tag{4.37}$$

The reconstructed distributions of the distance traveled by K^0_S and Λ after their production at the primary vertex are shown in Figs. 4.21 (a) and (c). The lifetime of each particle can be calculated as

$$t[10^{-10}\ \text{s}] = \frac{d[\text{cm}] \times m[\text{GeV}/c^2]}{|\mathbf{p}|[\text{GeV}/c]}, \tag{4.38}$$

where d is the distance traveled by the particle, m is the mass of the particle, and $\mathbf{p}$ is the three-momentum of the particle. The distribution of the lifetime is shown in Figs. 4.21 (b) and (d) and in both of the plots, linear fits are drawn. The reciprocal of the slope of these fits provides the respective mean lifetimes of the K^0_S and Λ. The PDG values [4]of the mean lifetime for K^0_S and Λ are $(0.8958 \pm 0.0005) \times 10^{-10}$ s and $(2.631 \pm 0.020) \times 10^{-10}$ s, respectively. The values from our fit are $(0.864 \pm 0.032) \times 10^{-10}$ s for K^0_S and $(2.865 \pm 0.046) \times 10^{-10}$ s for Λ.

4.12 Acceptance and efficiency determination

The acceptance for $\gamma n \to K^0\Lambda$ was determined from a Monte Carlo simulation of the experimental set-up. Approximately 25 million events for K^0_S with a phase-space distribution of energy and momenta were simulated in the energy range E_γ = (925 - 1430) MeV.

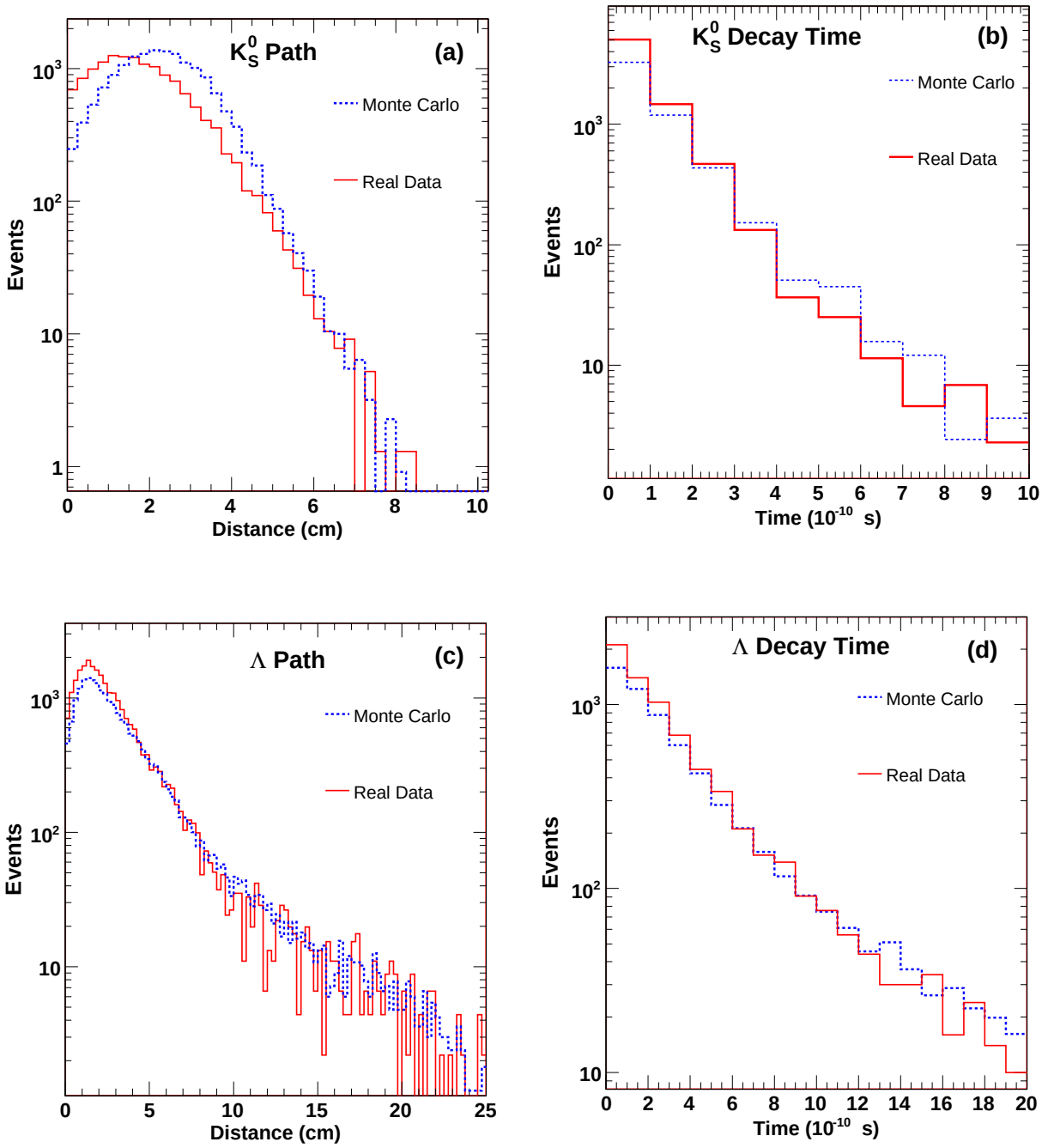

Figure 4.20: (a) The distributions of the distance traveled by K^0_S before its decay for Monte Carlo simulation (blue dashed line) and for real data (red solid line). (b) The distribution of the lifetime of K^0_S for Monte Carlo simulation (blue dashed line) and for real data (red solid line). (c) The distribution of the distance traveled by Λ before its decay for Monte Carlo simulation (blue dashed line) and for real data (red solid line). (d) The distribution of the lifetime of Λ for Monte Carlo simulation (blue dashed line) and for real data (red solid line).

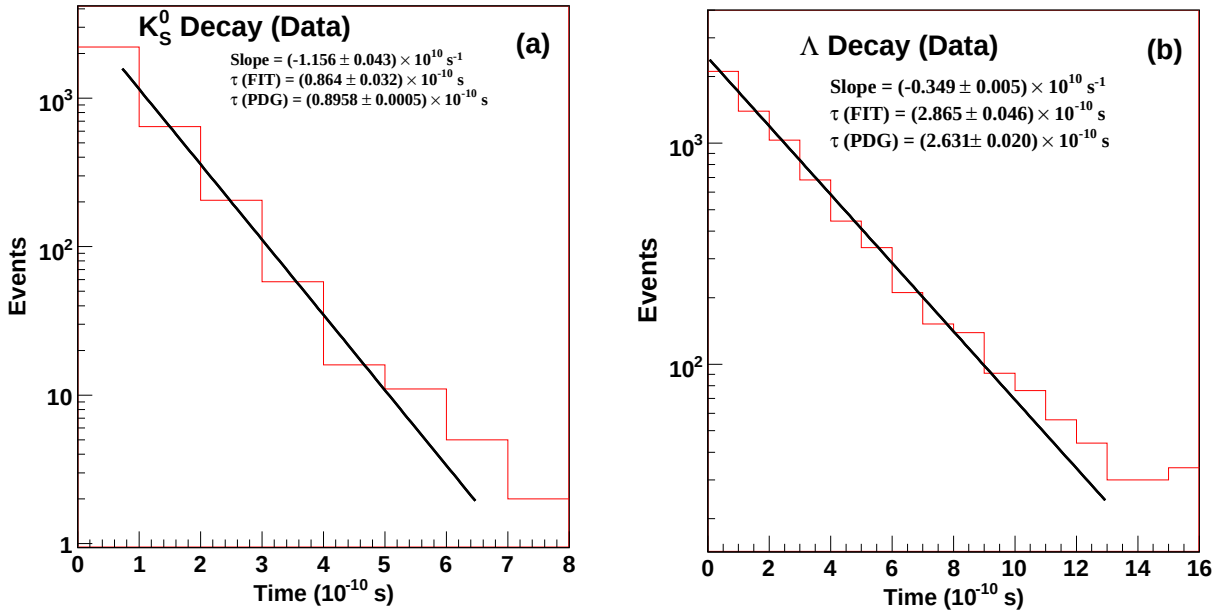

Figure 4.21: (a) The distribution of the lifetime for the K^0_S with fit values $(0.864 \pm 0.0320) \times 10^{-10}$ s and the PDG values [4], $(0.8958 \pm 0.0005) \times 10^{-10}$ s. (b) The distribution of the lifetime for the Λ with fit values $(2.865 \pm 0.046) \times 10^{-10}$ s and the PDG values [4], $(2.631 \pm 0.020) \times 10^{-10}$ s.

The simulated data were treated in exactly the same manner as the experimental data, both running through the same analysis code. In general, acceptance is the ratio of the number of events reconstructed to the number of events generated. Let us consider the angular variation of K^0_S for different energy bins E_γ, then the acceptance $\varepsilon(E_\gamma, \theta_{K^0_S})$ for each $(E_\gamma, \theta_{K^0_S})$ bin is given as

$$\epsilon(E_\gamma, \theta_{K^0_S}) = \frac{\text{number of } \mathrm{K^0_S} \text{ observed in the } \mathrm{E_\gamma}, \theta_{\mathrm{K^0_S}} \text{ bin}}{\text{number of } \mathrm{K^0_S} \text{ thrown in the } \mathrm{E_\gamma}, \theta_{\mathrm{K^0_S}} \text{ bin}}. \tag{4.39}$$

Figure 4.22 shows the calculated acceptance for $\gamma n \to K^0\Lambda$ plotted as a function of the center-of-mass angle of the K^0_S ($\Theta^{\mathrm{CM}}_{\mathrm{K^0}}$) for different energy bins. At backward angles the acceptance for $\gamma n \to K^0\Lambda$ is better than at forward angles because of the beam exit opening.

When we consider the variation of the acceptance only with the beam energy of photon E_γ, it gives the mean detector efficiency $\epsilon_{\mathrm{det}}(E_\gamma)$. Figure 4.23 shows the detector efficiency for $\gamma n \to K^0\Lambda$ as a function of the incident photon energy. It indicates that the efficiency remains about 17% for incident photon energies below 1200 MeV, and falls to about 8% at a photon energy of 1400 MeV. At energies close to threshold ($E_\gamma = 925$ MeV), the efficiency remains high. All six final-state photons come out with a very low momentum at such low energies. As E_γ increases, the final-state particles gain more and more momentum, which increases the chance that they will be lost from the beam exit tunnel. In addition, at higher incident photon energies, it is more likely that cluster mergers will occur at forward angles, and such events will not survive the multiplicity cut. This effect contributes to the decrease in acceptance at forward angles and at the largest values of E_γ.

4.13 Photon flux determination

For the correct measurement of the cross section, it is essential to know the number of beam photons that are incident on the target. We have described the tagging efficiency in

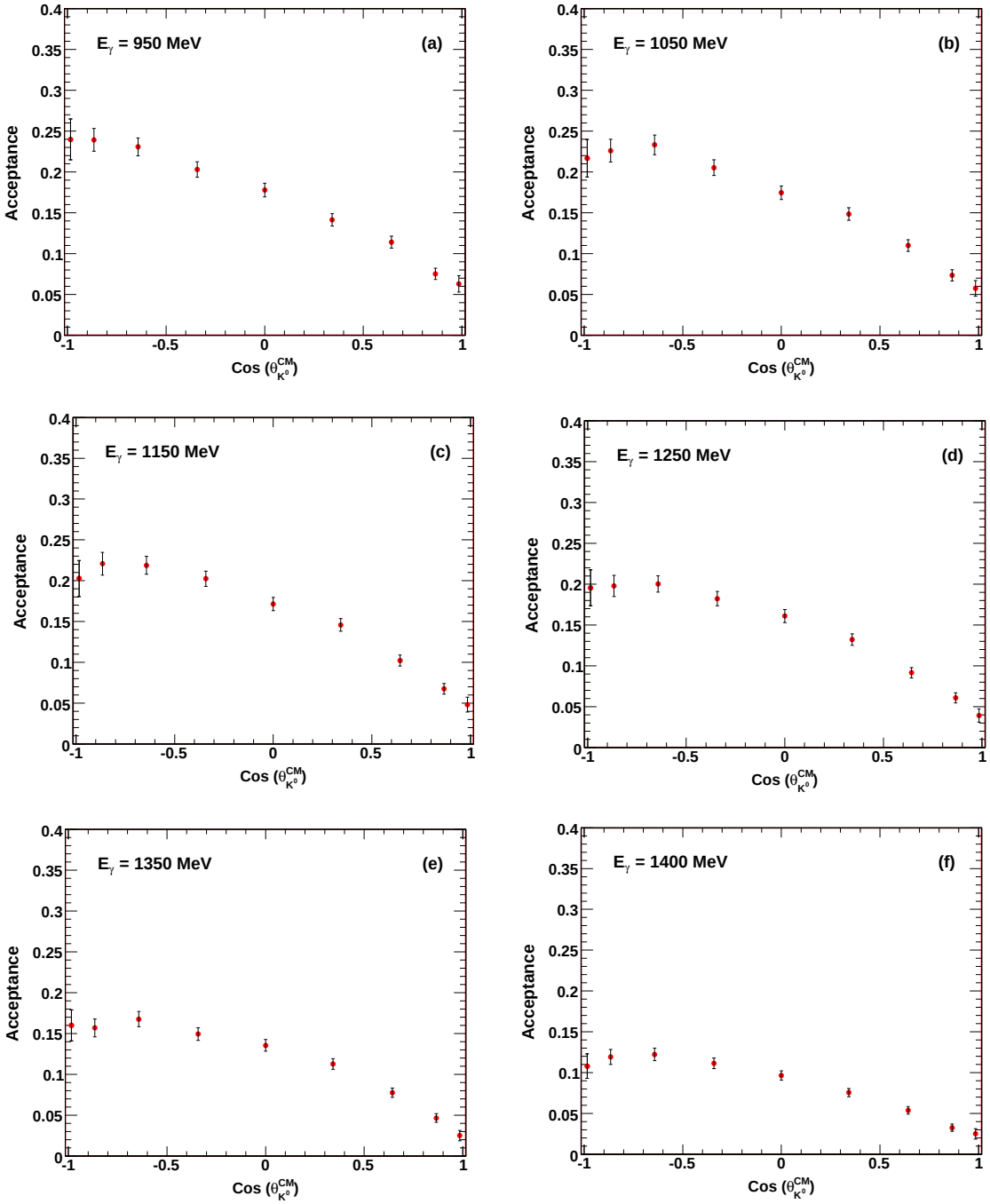

Figure 4.22: The acceptance for $\gamma n \to K^0\Lambda$ as a function of $\cos(\theta^{\mathrm{CM}}_{\mathrm{K}^0})$ for beam energies between 950 and 1400 MeV.

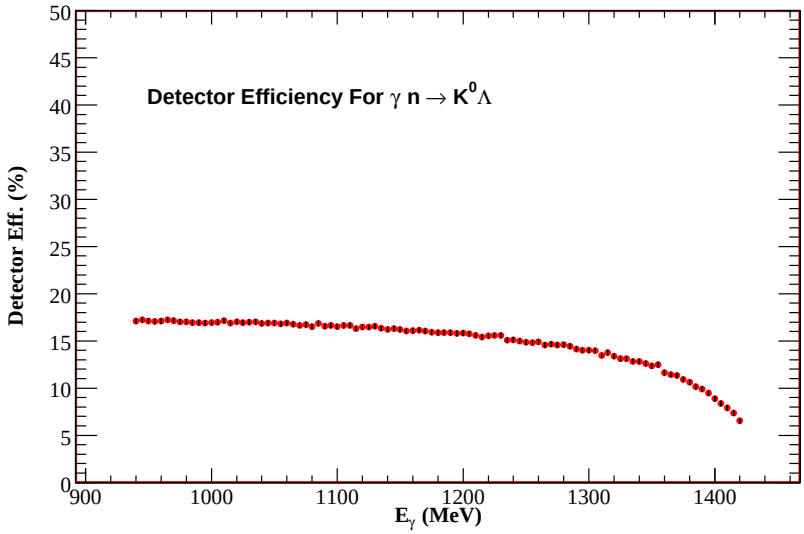

Figure 4.23: Detector efficiency for $\gamma n \rightarrow K^0\Lambda$ events as a function of incident photon energy.

Sec. 3.2. As tagging efficiency depends on how well the beam is aligned, its measurement should be done during the MAMI beam optimization. For this experiment, tagging efficiency measurements were performed on a daily basis. The running of the accelerator for a long time causes a buildup of background radiation. In order to account for this, **beam off** measurements were made of the background counts in the tagger scalers (without any radiator) before and after each tagging efficiency measurement.

After subtracting this background from the "beam off" measurement, Eq. (3.3) can be rewritten as

$$\epsilon_{\text{tagg}}[i] = \frac{N_\gamma[i]}{N_e[i] - N_{\text{backgd}}[i]}, \tag{4.40}$$

where i stands for each tagger channel in the focal plane ladder, N_γ is the number of photons that passed through the collimator, and N_e is the number of electrons detected in the tagger ladder. Using this equation, one can compute the tagging efficiency for each individual channel. The tagging efficiency during our experiment is shown in Fig. 4.24.

Once we have determined the tagging efficiency for each channel, it is trivial to

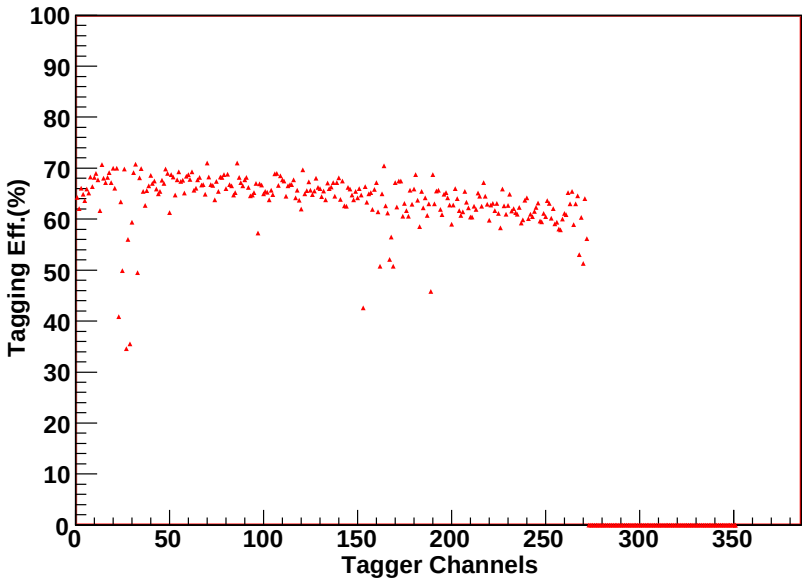

Figure 4.24: The tagging efficiency during our measurements.

calculate the corresponding photon flux for each tagger channel as

$$\mathrm{Flux}[i] = \varepsilon_{\mathrm{tagg}}[i] \times N_e[i]. \tag{4.41}$$

This equation gives the flux for each channel as a product of the tagging efficiency of each channel and the corresponding number of incident electrons on those channels. Figure 4.25 shows the photon flux, which is related to the number of incident photons on the target. The fitted curve in the figure shows that the photon flux is inversely proportional to the incident photon energy.

4.14 Empty target background subtraction

As mentioned in Sec. 3.7, the liquid deuterium target was kept inside a cylindrical cell made of Kapton (Fig. 3.14). During the experiment this Kapton cell might contribute to the prompt background events by the processes of pair production and Compton scattering. In order to correct for this background, data were taken with an empty target cell for several hours. The empty target subtraction was performed by subjecting the empty-target

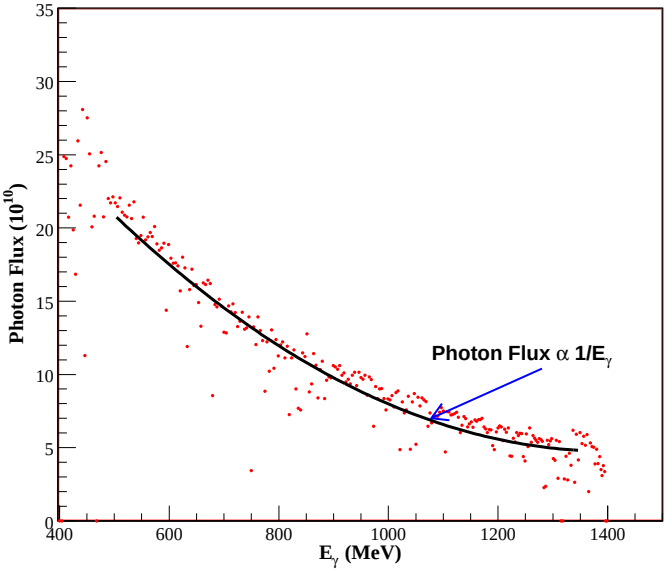

Figure 4.25: The photon flux, which is related to the number of incident photons on the target.

data to the same analysis procedures as the full-target data. The subtraction was done by normalizing the target-empty counts by the photon flux so that, for each tagger channel and energy bin, the yield (Y_{subt}) is [59]

$$Y_{\text{subt}} = Y_{\text{full}} - r_{\text{f}_\text{e}} \times Y_{\text{empty}}, \tag{4.42}$$

where Y_{full} and Y_{empty} are respective counts for the full and empty target runs, and r_{f_e} is the ratio of the photon flux for the full and the empty runs:

$$r_{\text{f}_\text{e}} = \frac{\text{PhotonFlux}_{\text{full}}}{\text{PhotonFlux}_{\text{empty}}}.$$

As the photon flux is the product of the tagging efficiency $(\varepsilon_{\text{tagg}})$ and the electron flux ElectronFlux, r_{f_e} can be further written as

$$r_{\text{f}_\text{e}} = \frac{\epsilon_{\text{tagg}} \times \text{ElectronFlux}_{\text{full}}}{\epsilon_{\text{tagg}} \times \text{ElectronFlux}_{\text{empty}}} = \frac{\text{ElectronFlux}_{\text{full}}}{\text{ElectronFlux}_{\text{empty}}}.$$

The uncertainty associated with the subtraction yield (σ_Y) is

$$\sigma_Y = (\sigma_{Y^2_{\text{full}}} + r^2_{\text{fe}}\sigma_{Y^2_{\text{empt}}})^{\frac{1}{2}},$$

where $\sigma_{Y_{\text{full}}}$ and $\sigma_{Y_{\text{empt}}}$ are the statistical uncertainties corresponding to the full and empty yields and are given by their square roots.

.

Chapter 5

Result and Discussions

This chapter describes how numerical values for the differential cross section $d\sigma/d\Omega$ and the total cross section $\sigma_{\rm tot}$ for $\gamma n \to K^0\Lambda$ were calculated. A discussion is provided for how the statistical uncertainties in these quantities were determined. Our results for $\gamma n \to K^0\Lambda$ are presented graphically and these results are compared with the theoretical predictions discussed in Chapter 2. We also discuss an expansion of our results for $d\sigma/d\Omega$ in terms of Legendre polynomials.

5.1 Calculation of differential cross section

The differential cross section is a measurable quantity that describes the likelihood of an interaction for a given set of kinematics. In general, the differential cross section is related to the probability of detecting the scattered particle at center-of-mass angles $\theta_{\rm CM}$ and ϕ, where $\theta_{\rm CM}$ is the polar angle with respect to the incident photon and ϕ is the azimuthal angle. For our work, $\frac{d\sigma}{d\Omega}$ was only a function of $\theta_{\rm CM}$ as the liquid deuterium target was unpolarized. The differential cross section was calculated by using the formula:

$$\frac{d\sigma}{d\Omega}(E_\gamma, \theta_{\rm CM}) = \frac{N_{\rm events}(E_\gamma, \theta_{\rm CM})}{N_\gamma(E_\gamma) \times \varepsilon_{\rm accept}(E_\gamma, \theta_{\rm CM}) \times N_{\rm target} \times \mathcal{BR} \times [2\pi\Delta\cos\theta_{\rm CM}]}, \tag{5.1}$$

where:

- $\mathbf{N}_{\rm events}(\mathbf{E}_\gamma, \theta_{\mathbf{CM}})$ is the absolute number of reconstructed events and it is also known as the detected yield of the experiment.

- $\mathbf{N}_\gamma(\mathbf{E}_\gamma)$ is the number of photons incident on the target and it is also called the incident photon flux, which is given as the product of the tagging efficiency $(\varepsilon_{\rm tagg})$ and the number of electrons (N_{e^-}) as in Eq. (4.41).

- $\varepsilon_{\mathbf{accept}}(\mathbf{E}_\gamma, \theta_{\mathrm{CM}})$ is the acceptance of the detector calculated from Monte Carlo simulation as described in Sec. 4.12.

- $\mathcal{BR}$ is the product of branching ratios for our considered reaction.

  We define,

$$\begin{aligned}\mathcal{BR}(\gamma n \to K^0_S\Lambda \to \pi^0\pi^0\pi^0 n \to 6\gamma n) = \mathcal{B}(K^0 \to K^0_S)\times \\ \mathcal{B}(K^0_S \to 2\pi^0) \times \mathcal{B}(\Lambda \to \pi^0 n) \times \mathcal{B}(\pi^0 \to \gamma\gamma)^3,\end{aligned} \tag{5.2}$$

  where [4]:

$$\begin{aligned}\mathcal{B}(K^0 \to K^0_S) &= 0.5, \\ \mathcal{B}(K^0_S \to 2\pi^0) &= 0.3069 \pm 0.0005, \\ \mathcal{B}(\Lambda \to \pi^0 n) &= 0.3580 \pm 0.0050, \\ \mathcal{B}(\pi^0 \to \gamma\gamma) &= 0.9879 \pm 0.0003.\end{aligned}$$

  Thus, numerically

$$\begin{aligned}\mathcal{BR}(\gamma n \to K^0_S\Lambda \to \pi^0\pi^0\pi^0 n \to 6\gamma n) &= (0.5) \times (0.3069 \pm 0.0005) \times \\ &\quad (0.3580 \pm 0.0050) \times (0.9879 \pm 0.0003)^3 \\ &= 0.0529 \pm 0.0007.\end{aligned}$$

- $\mathbf{N}_{\mathrm{target}}$ is the number of protons in the target per cm^2, which is calculated by using the formula:

$$N_{\mathrm{target}} = \frac{\rho_d \times N_A \times L^{\mathrm{eff}}_{\mathrm{target}}}{M_d}, \tag{5.3}$$

with:

$$\begin{aligned}
\rho_d &= 0.162 \text{ g/cm}^{-3} \text{ is the density of liquid deuterium,} \\
N_A &= 6.022 \times 10^{23} \text{ mol}^{-1} \text{ is Avogadro's number,} \\
M_d &= 2.0141 \text{ g mol}^{-1} \text{ is a molar mass of liquid deuterium,} \\
L_{\text{target}}^{\text{eff}} &= 4.76 \text{ cm is the effective length of the target.}
\end{aligned}$$

Using all these values, we get

$$N_{\text{target}} = \frac{0.162 \times 6.022 \times 10^{23} \times 4.76}{2.0141} = 2.275 \times 10^{23} \text{ cm}^{-2}.$$

- $\Delta \cos\theta_{\text{CM}}$ is the corresponding size of the bin for $\cos\theta_{\text{CM}}$ the center-of-mass angle variation. In our analysis there were nine bins of equal width spanning $\cos\theta_{CM}$= -0.95 to +0.95.

5.1.1 Legendre polynomial fitting

The measured differential cross sections for all reactions can be expanded with a series of Legendre polynomials as:

$$\frac{d\sigma}{d\Omega} = \sum_{i=0}^{i_{\max}} A_i P_i(\cos\theta), \tag{5.4}$$

where P_i is the i-th order Legendre polynomial and $i_{\max}$ was the highest order used in the series. The choice of $i_{\max}$ was made in such a way that for all $i > i_{\max}$, A_i was consistent with zero. The coefficients A_i have dimensions of area. For fitting purposes, it was useful to rewrite Eq. (5.4) as

$$\frac{d\sigma}{d\Omega} = A_0 \left[1 + \sum_{i=0}^{i_{\max}} B_i P_i(\cos\theta) \right], \tag{5.5}$$

where $B_i = A_i/A_0$. The corresponding ratios, A_i/A_0 are then independent of any systematic uncertainty in the normalization of our cross-section measurements.

The total cross sections, $\sigma_{\rm tot}(E_\gamma)$, were calculated by integrating the fitted differential cross section as:

$$\sigma_{\rm tot} = \int \frac{d\sigma}{d\Omega} d\Omega = 4\pi A_0. \tag{5.6}$$

5.2 Background subtractions

As described in Sec. 4.9, $\gamma p \to K^0\Sigma^+$, $\gamma n \to K^0\Sigma^0$, $\gamma N \to \eta N$, and $\gamma N \to 3\pi^0 N$ are background reactions to our considered reaction $\gamma n \to K^0\Lambda$. Our Monte Carlo studies show that these reactions contribute a significant number of events that look like $\gamma n \to K^0\Lambda$. By using Eq. (4.35), the number of events due to each of the background reactions can be estimated in the experimental data. It is essential to evaluate the contamination ratio $\varepsilon_{\rm MC}$ for each of these background reactions. Following the notation in Sec. 4.10.2, $\varepsilon_{\rm MC}(K^0_S\Lambda/K^0_S\Sigma^+)$, $\varepsilon_{\rm MC}(K^0_S\Lambda/K^0_S\Sigma^0)$, $\varepsilon_{\rm MC}(K^0_S\Lambda/\eta N)$, and $\varepsilon_{\rm MC}(K^0_S\Lambda/3\pi^0 N)$ represent the contamination ratios for $\gamma p \to K^0_S\Sigma^+$, $\gamma n \to K^0_S\Sigma^0$, $\gamma N \to \eta N$, and $\gamma N \to 3\pi^0 N$, respectively. In order to determine the differential cross section for $\gamma n \to K^0\Lambda$, it is necessary to find the angular distribution of $\varepsilon_{\rm MC}$ in each E_γ bin. For the real data, knowing the values of $\varepsilon_{\rm MC}$ and the corresponding number of events (such as $K^0_S\Lambda$, $K^0_S\Sigma^+$, ηN, and $3\pi^0 N$) that are identified in the real data, the background corrected events for $\gamma n \to K^0_S\Lambda$ can be evaluated using Eq. (4.36). Figure 5.1 shows the angular distributions of the contamination ratios $\varepsilon_{\rm MC}$ at E_γ = 1250 MeV for the various background reactions to $\gamma n \to K^0\Lambda$. A comparison of the value of $\varepsilon_{\rm MC}$ with the background contributions listed in Table 4-1 shows that the magnitude of $\varepsilon_{\rm MC}$ for each background reaction depends on its contribution to $\gamma n \to K^0\Lambda$. The angular variations and magnitudes of $\varepsilon_{\rm MC}$ for each of the background channels are not similar. For $\gamma p \to K^0\Sigma^+$, the contamination ratio increases in going from backward to forward angles; for other background reactions, the contamination ratios have a less pronounced angular variation. The angular variations of $\varepsilon_{\rm MC}$ follow similar trends in other energy bins.

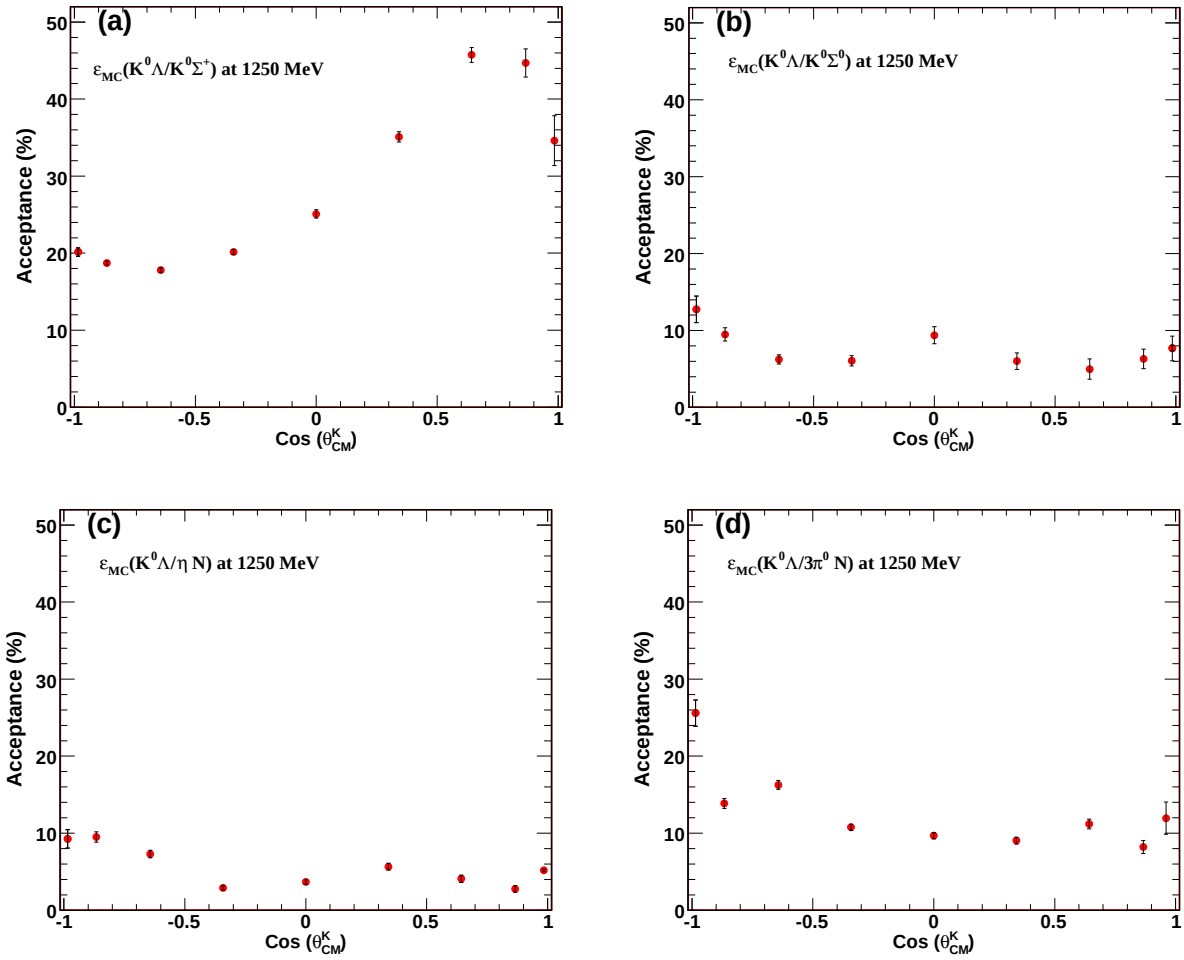

Figure 5.1: Angular distributions of contamination ratio $\varepsilon_{\mathrm{MC}}$ for the reaction $\gamma n \to K^0\Lambda$ at E_γ= 1250 MeV due to (a) $\gamma p \to K^0\Sigma^+$, (b) $\gamma n \to K^0\Sigma^0$, (c) $\gamma N \to \eta N$, and (d) $\gamma N \to 3\pi^0 N$. The angular distributions for other energy bins are similar.

5.3 Differential cross section for $\gamma n \rightarrow K^0\Lambda$

As described in Sec. 5.1, the differential cross section for $\gamma n \rightarrow K^0\Lambda$ at a given photon energy, E_γ, and center-of-mass angle, $\theta_{\rm CM}$, was calculated by using Eq. (5.1). Determination of the corresponding uncertainties is discussed in Sec. 5.5.

We extracted $d\sigma/d\Omega$ at 19 incident photon energies: 925, 950, 975, 1000, 1025, 1050, 1075, 1100, 1125, 1150, 1175, 1200, 1225, 1250, 1275, 1300, 1325, 1350, and 1375 MeV. Figure 5.2 shows $d\sigma/d\Omega$ for each of these energy bins; our numerical values for $d\sigma/d\Omega$ are tabulated in Appendix C. For each value of E_γ, we extracted $d\sigma/d\Omega$ in nine $\cos(\theta_{\rm CM})$ bins ranging from $\cos(\theta_{\rm CM}) = -0.95$ to 0.95.

In general, we observe that the magnitude of the differential cross section increases with the value of the photon energy. The differential cross section between 925 and 1000 MeV is almost flat in shape (isotropic), which suggests that this region is s-wave dominated. At energies above 1075 MeV, the differential cross section has a slight convex shape.

5.3.1 Comparison with model predictions

There are no published experimental results of the differential cross section for $\gamma n \rightarrow K^0\Lambda$ with which we can compare our results. However, we are able to compare our results with the KAON-MAID and SLA predictions described in Chapter 2. Figure 5.3 compares our results for $d\sigma/d\Omega$ at $E_\gamma = 1100$ MeV with predictions from these two models. Our differential cross section at this energy is more similar to the Kaon-MAID prediction in that both have a slight convex shape and about the same magnitude.

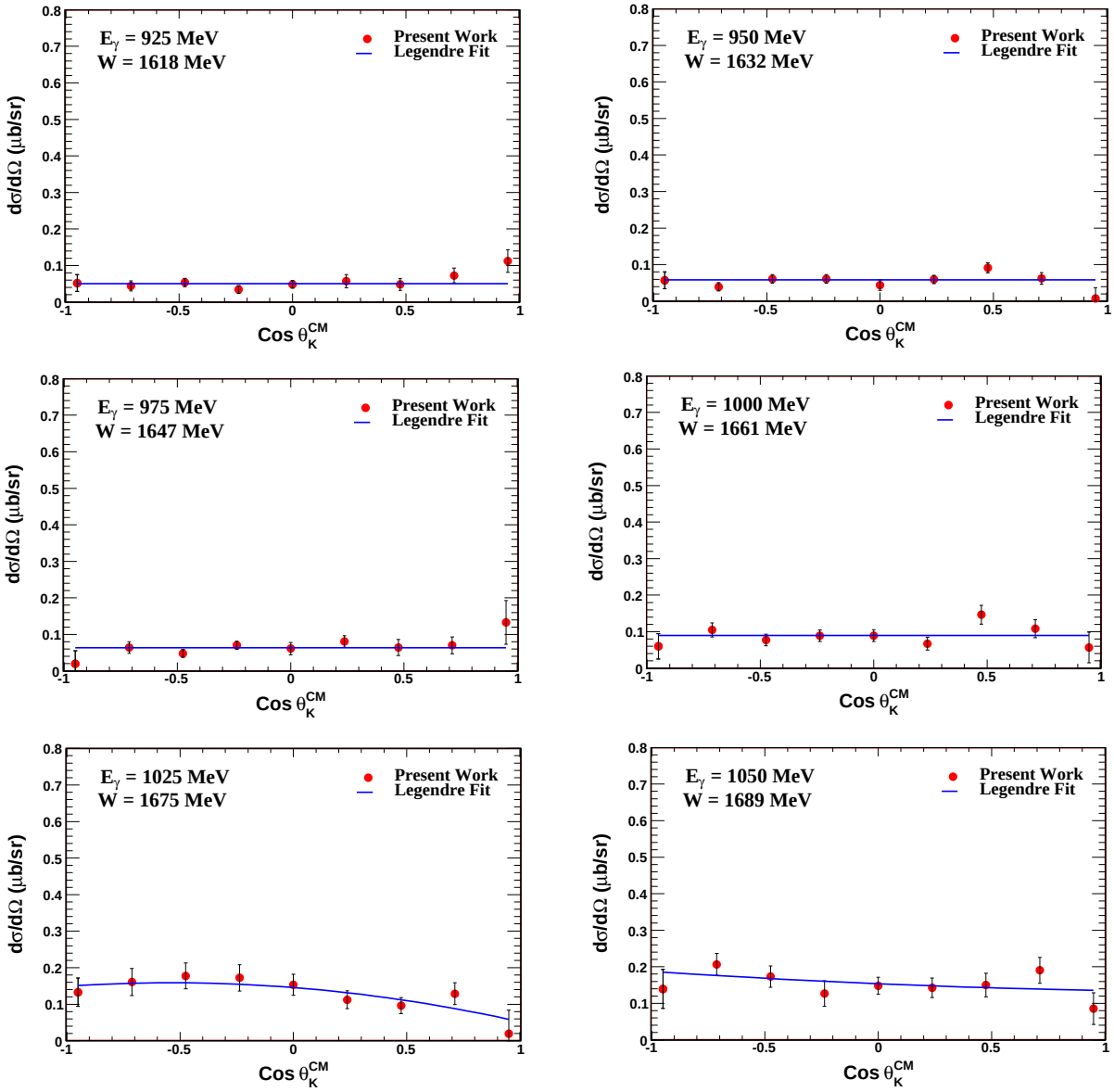

Figure 5.2: Differential cross section in the center-of-mass system for the reaction $\gamma n \rightarrow K^0\Lambda$ at incident photon energies, E_γ, from 925 to 1375 MeV. The plots also show the corresponding center-of-mass energy W. The solid curves are from the Legendre polynomial fits to our data.

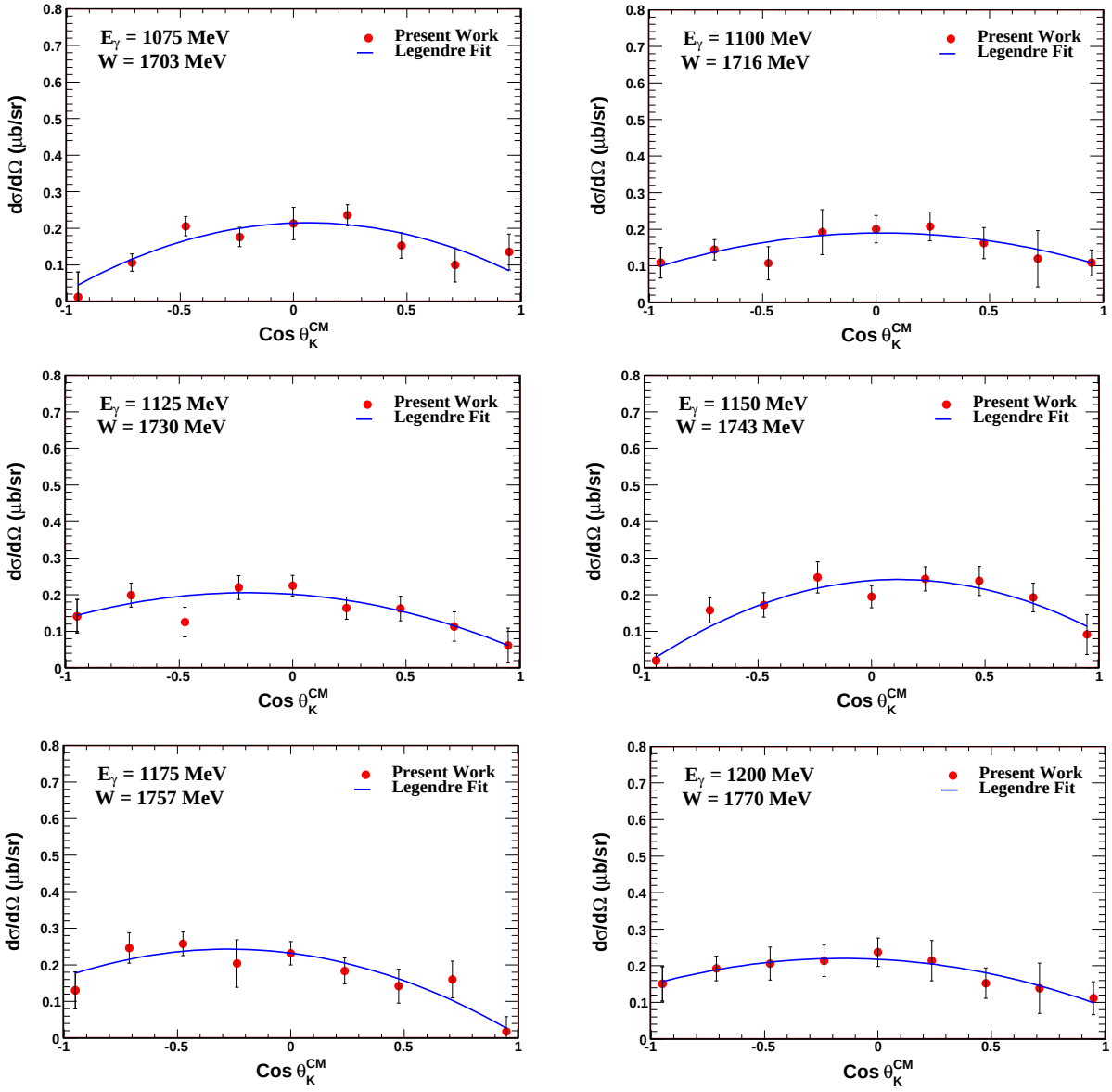

Figure 5.2: Continued.

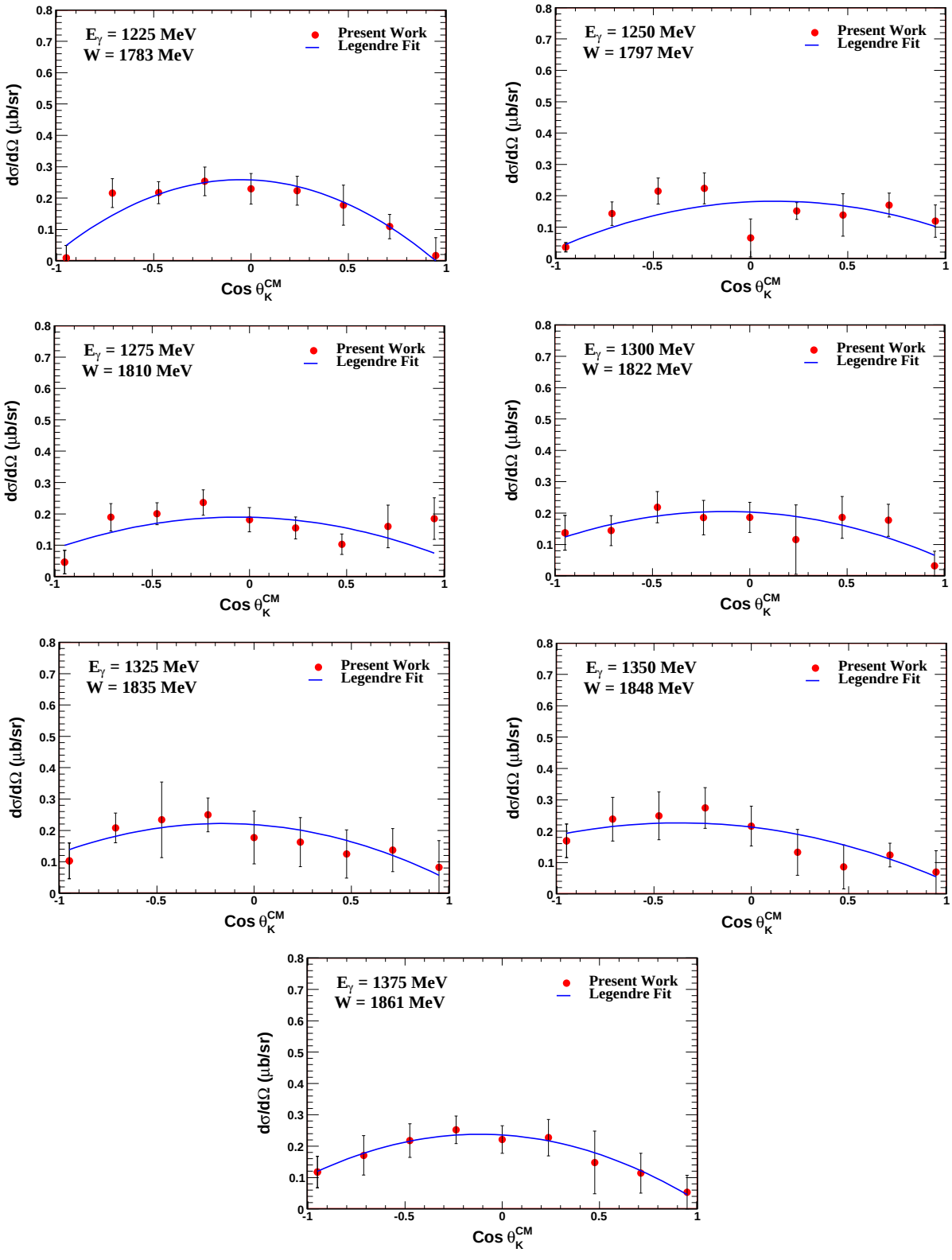

Figure 5.2: Continued.

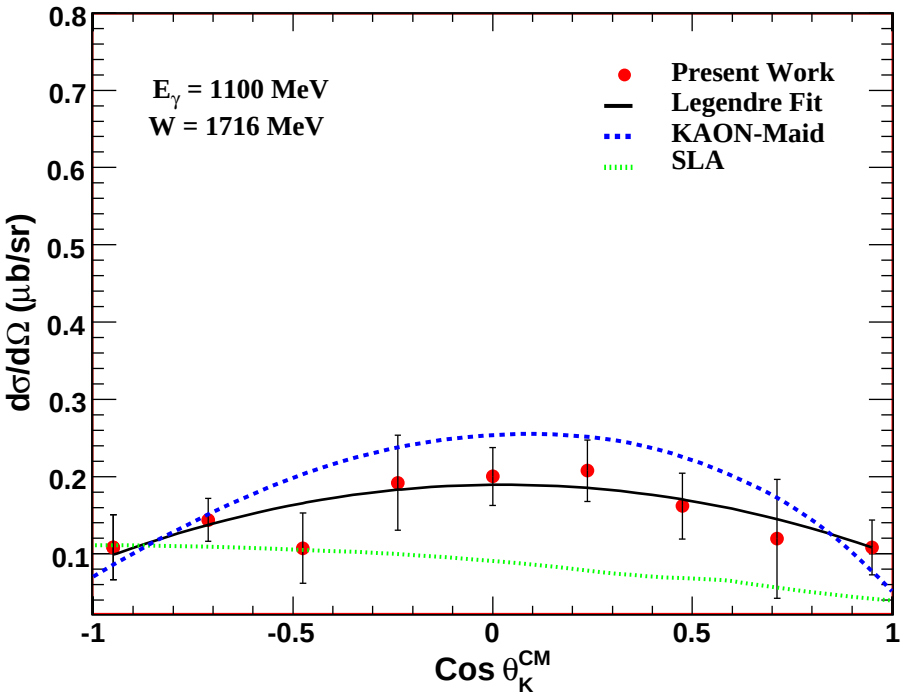

Figure 5.3: Comparison of our results (red filled circles) for the differential cross section of $\gamma n \to K^0\Lambda$ at $E_\gamma = 1100$ MeV with predictions of the Kaon-MAID model [31] (blue dashed curve) and the SLA model [26] (green dotted curve). The solid curve is the result of the Legendre polynomial fit to our data.

5.3.2 Legendre fitting coefficients

The Legendre coefficients for the fit of $d\sigma/d\Omega$ for the reaction $\gamma n \to K^0\Lambda$ are plotted in Fig. 5.4 and tabulated in Appendix D. The Legendre fits were obtained for maximum values of n between 2 and 4. Fitted values of A_3/A_0 and A_4/A_0 were found to be consistent with zero over the entire energy range. Therefore, our final fits used a maximum value of $n = 2$ and these are the results displayed in Fig. 5.2. As exceptional cases, the values of A_1/A_0 and A_2/A_0 were found to be consistent with zero for $E_\gamma = 925$ to 1000 MeV; thus, data at these energies were fitted only with A_0. A_1/A_0 was found to be small over the entire energy range. A_2/A_0 is generally negative for energies above $\sim$1050 MeV.

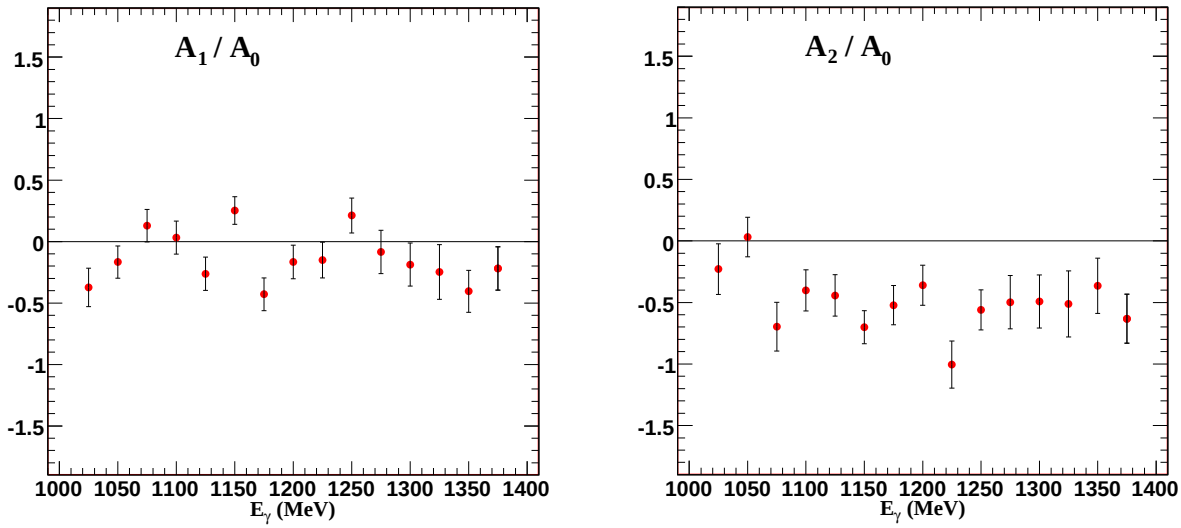

Figure 5.4: Legendre fitting coefficients for $d\sigma/d\Omega$ of the reaction $\gamma n \to K^0\Lambda$.

5.4 Total cross section for $\gamma n \to K^0\Lambda$

The amount of background to be subtracted from $\gamma n \to K^0\Lambda$ can be calculated using the values of the contamination ratios as described in Sec. 5.2 and Eq. (4.35). Figure 5.5 shows the measured total cross section for $\gamma n \to K^0\Lambda$ without background subtraction and the estimated background stemming from all the background reactions ($\gamma p \to K^0\Sigma^+$, $\gamma n \to K^0\Sigma^0$, $\gamma N \to \eta N$, and $\gamma N \to 3\pi^0 N$) and the empty target. The background contributions were computed on a bin-by-bin basis. Figure 5.6 shows $\sigma_{\rm tot}(\gamma n \to K^0\Lambda)$ obtained after the background subtraction as a function of center-of-mass energy W. The values of $\sigma_{\rm tot}$ are tabulated in Appendix C. The total cross section increases rapidly from threshold up to 1700 MeV and from there it gradually increases with W. Because of the low photon flux at higher energies, we could not extract the total cross section beyond 1870 MeV. The statistical uncertainties in the measured cross section are about 5% at the lowest energies and increase to about 13% at the highest energies.

The percentage background contributions to $\sigma_{\rm tot}(\gamma n \to K^0\Lambda)$ stemming from all four background reactions and the empty target are tabulated in Appendix G. The empty target

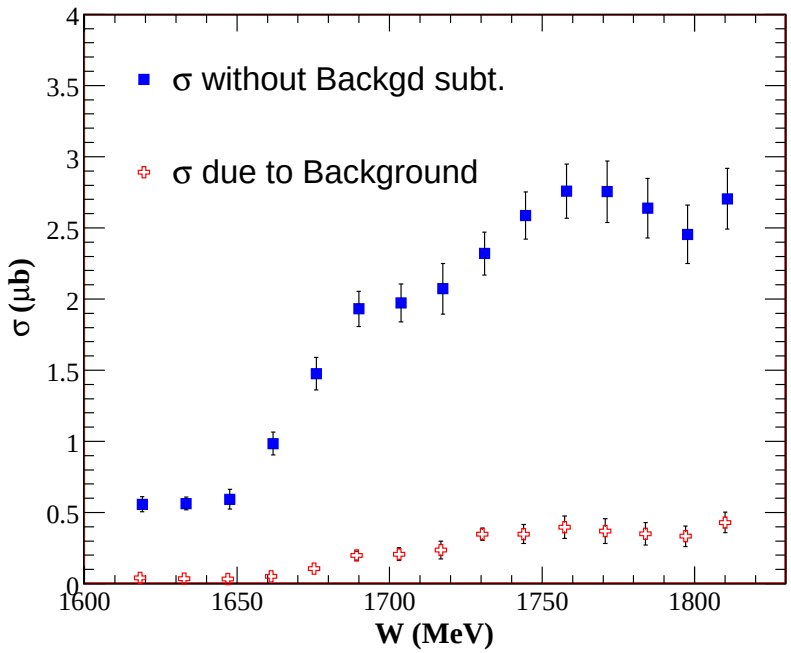

Figure 5.5: The total cross section for $\gamma n \to K^0\Lambda$ without subtraction of background (filled squares) and estimation of the total contribution of background stemming from the background reactions and the empty target (open crosses) as described in the text.

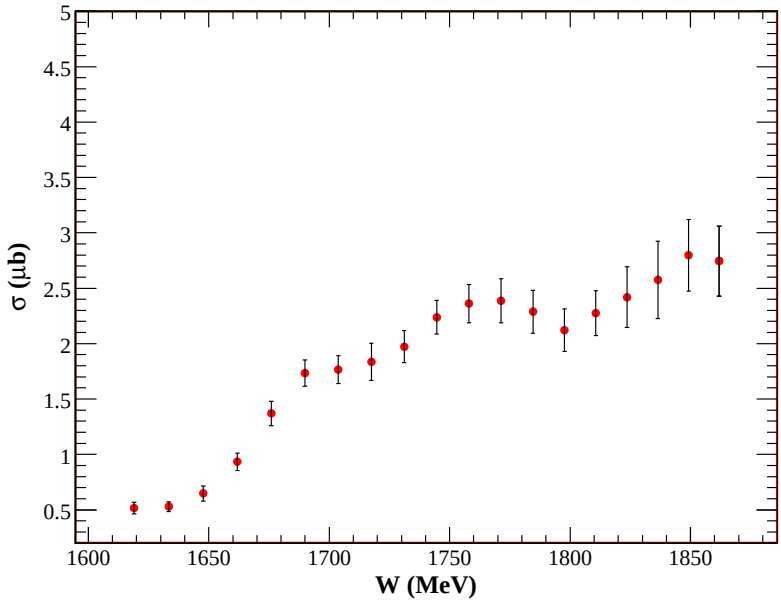

Figure 5.6: The total cross section for $\gamma n \to K^0\Lambda$ after background subtractions as a function of center-of-mass energy W. The error bars shown are due only to counting statistics.

contributes about ∼1% to the total background. The total percentage background contribution varies from about 5-20%. The individual reactions $\gamma p \to K^0\Sigma^+$, $\gamma n \to K^0\Sigma^0$, $\gamma N \to \eta N$, and $\gamma N \to 3\pi^0 N$ contribute 7-10%, 2-3%, 3-4%, and 1-2% to the total background, respectively. For energies below $W \sim$ 1690 MeV, the only background contributions are from the reactions $\gamma N \to \eta N$ and $\gamma N \to 3\pi^0 N$, and the empty target. At higher energies, there are also contributions to the background from $\gamma p \to K^0\Sigma^+$ and $\gamma n \to K^0\Sigma^0$.

As mentioned in Chapter 2, there are no published experimental results with which we can compare our measurements. However, we may compare our results with model predictions. Figure 5.7 compares our results, represented by the red solid circles, to the KAON-MAID [31] predictions as indicated by the blue solid curve and to the SLA [26] prediction with $r_{KK_1} = -2.09$ by the green dashed curve. Our results are in fairly good agreement with the Kaon-MAID prediction up to W = 1700 MeV, but above this energy,

our measured cross section is smaller than the Kaon-MAID prediction. Compared with the SLA prediction, our measurements are systematically larger across the entire energy range.

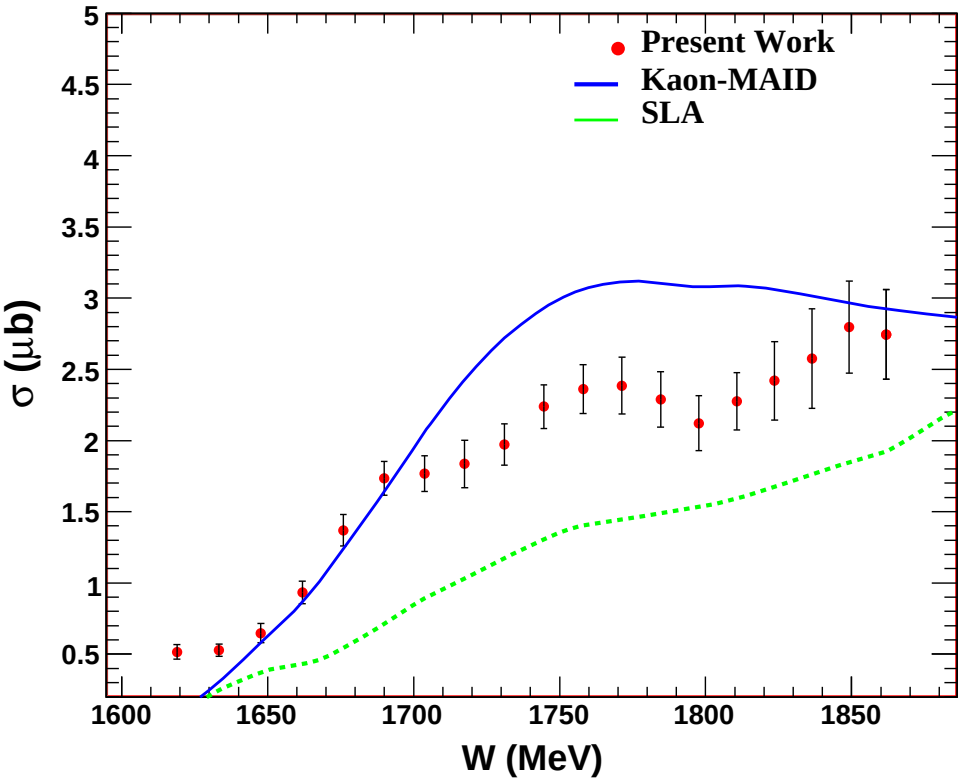

Figure 5.7: Comparison of our results (red filled circles) for $\sigma_{\rm tot}(\gamma n \rightarrow K^0\Lambda)$ after background subtraction with predictions of the Kaon-MAID model [31] (blue solid curve) and SLA model [26] (green dashed curve).

5.5 Uncertainties in $d\sigma/d\Omega$

In Sec. 4.10.2 the background subtraction procedure for $\gamma n \rightarrow K^0\Lambda$ has been described. The major statistical uncertainty in $d\sigma/d\Omega$ comes from the number of events obtained from the background subtraction. In addition to the background subtraction, an empty target subtraction must be made in order to determine the final number of $\gamma n \rightarrow K^0\Lambda$ events.

For simplicity, Eq. (4.36) can be rewritten as

$$N_{\rm event}^{K^0} = N_{\rm data}^{K^0\Lambda} - N_{\rm empty} - N^{\gamma p\to K^0\Sigma^+} - N^{\gamma n\to K^0\Sigma^0} - N^{\gamma N\to \eta N} - N^{\gamma N\to 3\pi^0 N}. \tag{5.7}$$

The statistical uncertainty in each number of events is computed as the square root of the number of events. As the uncertainties in all the contributions are independent to each other, the uncertainty $\Delta N_{\rm event}^{K^0}$ in the total number of extracted $\gamma n \to K^0\Lambda$ events is

$$\Delta N_{\rm event}^{K^0} = \Big[(\Delta N_{\rm data}^{K^0\Lambda})^2 + (\Delta N^{\gamma p\to K^0\Sigma^+})^2 + (\Delta N^{\gamma n\to K^0\Sigma^0})^2 + (\Delta N^{\gamma n\to \eta N})^2 + (\Delta N^{\gamma N\to 3\pi^0 N})^2\Big]^{1/2}. \tag{5.8}$$

We have seen the differential cross section in Eq. (5.1) is obtained by dividing the absolute number of reconstructed events $N_{\rm event}^{K^0}$ for a specific bin by the photon flux N_γ, the acceptance $\varepsilon_{\rm accept}$, the surface target density $N_{\rm target}$, and branching ratios $\mathcal{BR}$. Thus, the uncertainty in the extracted cross section depends upon the uncertainties in the number of reconstructed events, photon flux, acceptance, target density, and the branching ratios. The general formula for the differential cross section can be rewritten as

$$\frac{d\sigma}{d\Omega} = \frac{N_{\rm events}^{K^0}}{N_\gamma \times \varepsilon_{\rm accept} \times N_{\rm target} \times \mathcal{BR} \times \otimes}, \tag{5.9}$$

where Ω is the solid angle for the bin and the other symbols carry the usual meanings as defined here and in Sec. 5.1.

As all the factors in Eq. (5.9) are independent, the statistical uncertainty in $d\sigma/d\Omega$ is determined by summing each contribution in quadrature:

$$\Delta d\sigma/d\Omega = d\sigma/d\Omega \times \left[\left(\frac{\Delta N_{\rm events}^{K^0}}{N_{\rm events}^{K^0}}\right)^2 + \left(\frac{\Delta N_\gamma}{N_\gamma}\right)^2 + \left(\frac{\Delta \varepsilon_{\rm accept}}{\varepsilon_{\rm accept}}\right)^2 + \left(\frac{\Delta N_{\rm target}}{N_{\rm target}}\right)^2 + \left(\frac{\Delta \mathcal{BR}}{\mathcal{BR}}\right)^2\right]^{1/2}. \tag{5.10}$$

In our experiment, the average fractional uncertainty in the final number of selected events, $N_{\rm events}^{K^0}$, is about 25%. The second term is related to the tagging efficiency measurements.

Using Eq. (4.41), we estimate the fractional uncertainty in N_γ to be 3 to 4%. The third term is due to the Monte Carlo simulation of the detection efficiency. As shown in Fig. 4.22 the average uncertainty in $\varepsilon_{\text{accept}}$ is about 2%. The target length was measured at a temperature of 21 K with a precision of $\pm$1% [60], which introduces a 1% uncertainity in N_{target}. From Sec. 5.1, it can be inferred that the uncertaintity in $\mathcal{BR}$ is about 1.3%. Now keeping these respective values of uncertaintity in Eq. (5.10), it can be concluded that the statistical uncertainity in the number of selected events dominates the total uncertaintity in $d\sigma/d\Omega$.

Chapter 6

Summary and Conclusions

In this dissertation, we have described our cross-section measurements for the reaction $\gamma n \to K^0\Lambda$. Our experiment was performed at the Mainz Microtron (MAMI-C) using the Crystal Ball (CB) multiphoton spectrometer as a central detector and the TAPS calorimeter as a forward wall. Unpolarized photon beams were produced by bremsstrahlung in the energy range up to 1400 MeV by passing the electron beam through a 10-μm copper radiator. The deflected electrons were momentum analyzed by the Glasgow Tagger, which consists of a momentum-dispersing magnetic spectrometer that diverts electrons onto a focal plane detector comprised of 353 half-overlapping plastic scintillators. The energetic photons impinged on a liquid deuterium target of length 4.76 cm located at the center of the Crystal Ball. The experimental trigger consisted of two main requirements: (i) the total energy deposited in the Crystal Ball had to exceed a threshold of 350 MeV, and (ii) the sector multiplicity in the CB had to be greater than or equal to 2.

We identified the reaction $\gamma n \to K^0\Lambda$ by the decay chain, $\gamma n \to K^0\Lambda \to (\pi^0\pi^0)(\pi^0 n) \to 6\gamma n$. The combination of the CB and TAPS covering almost 4π of solid angle was well suited for reliably measuring the 6-photon final state. Because the efficiency for detecting neutrons is relatively low, we assumed that the clusters of deposited energy in the Crystal Ball were due only to photons. The technique of kinematic fitting was used to analyze the 6-cluster events. Since the neutral kaon and Λ were not produced at rest, they propagate away from the primary vertex before they under go weak decays. Kinematic fitting was necessary to calculate where they decayed in the Crystal Ball.

Each 6-cluster event was tested for five possible hypotheses:

- that the event was from $\gamma n \to K^0\Lambda$;
- that the event was from $\gamma p \to K^0\Sigma^+$, where the Σ^+ was identified from its weak decay $\Sigma^+ \to \pi^0 p$;
- that the event was from $\gamma n \to K^0\Sigma^0$ (most of these events produced 7-cluster events that were immediately excluded from further analysis);
- that the event was from from $\gamma N \to \eta N$; and
- that the event was from $\gamma N \to 3\pi^0 N$, where the final-state pions were assumed to be produced at the primary vertex.

Events selected as coming from the reaction $\gamma n \to K^0\Lambda$ were required to have the highest likelihood (confidence level) out of these hypotheses. We also imposed a cut of 15% on the confidence level (CL) to the final selected events, which led to a much cleaner event sample. The angle-averaged detection efficiency for $\gamma n \to K^0\Lambda$ events using this criterion was found to be about 17% over almost our entire energy range.

The relative survival contributions of the background reactions were estimated using Monte Carlo (MC) generated events. For each generated background event, those that survived the selection tests for $\gamma n \to K^0\Lambda$ events were counted as background. In order to estimate and subtract background contributions, MC data for each of the five hypotheses were simulated and analyzed using the same criteria as for the real data. The backgrounds from direct $3\pi^0$ and η production were suppressed within our analysis, with the main background to $\gamma n \to K^0\Lambda$ coming from $\gamma p \to K^0\Sigma^+$ events. This problem is easily understood as being caused by our inability to resolve Λ and Σ events clearly in our K^0 missing mass spectra.

The details of the $\gamma n \to K^0\Lambda$ event selection criteria were as follows: (1) We required that the invariant mass of four of the photon clusters was consistent with the mass of

K_S^0 meson and that their corresponding missing mass was consistent with the mass of the Λ hyperon. (2) For the four photons identified as coming from the decay of a K_S^0 meson, we required that we could reconstruct the two neutral pions coming from the decay $K_S^0 \to 2\pi^0 \to 4\gamma$. (3) For the two photons identified as coming from the decay of a Λ hyperon, we required that their invariant mass was consistent with that of a π^0 and that their missing mass was consistent with that of a neutron.

We simultaneously measured events for the reaction $\gamma p \to K^0\Sigma^+$, which we identified by the decay channel with six photons and a proton in the final state. We required that the invariant mass of four of the photon clusters was consistent with the mass of the K_S^0 meson and that their corresponding missing mass was consistent with the mass of the Σ^+ hyperon. Events selected as coming from $\gamma p \to K^0\Sigma^+$ were required to have the highest likelihood out of the same hypotheses used to select $\gamma n \to K^0\Lambda$ events. The angle-averaged acceptance for $\gamma p \to K^0\Sigma^+$ events using this criterion was about 5% over almost our entire energy range. We determined differential and total cross sections for $\gamma p \to K^0\Sigma^+$, which were compared with prior measurements (see Appendix A). The good agreement of our results for $\gamma p \to K^0\Sigma^+$ with prior measurements provides support for our analysis procedures for both $\gamma p \to K^0\Sigma^+$ and $\gamma n \to K^0\Lambda$.

This dissertation reports the world's first measurements of $d\sigma/d\Omega$ and $\sigma_{\rm tot}$ for $\gamma n \to K^0\Lambda$. Our results were compared with predictions of the Kaon-MAID [31] and SLA [26] models. Our results for $\sigma_{\rm tot}$ are in fairly good agreement with the Kaon-MAID prediction up to W = 1700 MeV but above this energy, our measured cross section is smaller. Our measurements are systematically larger than the SLA prediction across the entire energy range.

Some final comments about our work are listed below.

- This dissertation reports the world's first experimental measurements of $d\sigma/d\Omega$ and $\sigma_{\rm tot}$

for $\gamma n \to K^0\Lambda$. We identified approximately 40,000 background-subtracted $\gamma n \to K^0\Lambda$ events.

- Our results for $\sigma_{\rm tot}(\gamma n \to K^0\Lambda)$ are similar in shape with the prediction of the Kaon-MAID model up to W= 1700 MeV but are lower at higher energies; in comparison to the SLA model, our results are higher over the entire energy range.

- In the energy range E_γ = 1000 to 1400 MeV, our results for $\sigma_{\rm tot}(\gamma p \to K^0\Sigma^+)$ are in good agreement with prior measurements. We identified about 3,400 background-subtracted final $\gamma p \to K^0\Sigma^+$ events. By comparison, Goers *et al.* [34] (at E_γ up to 1.55 GeV), SAPHIR [58] (E_γ up to 2.6 GeV), CB-ELSA [52] (E_γ up to 2.3 GeV), CLAS [56] (E_γ up to 2.35 GeV) identified 405, 3,310, 10,000, and 15,650 final events of $\gamma p \to K^0\Sigma^+$, respectively.

- Results from the high statistics $g13$ experiment at JLab should eventually be published, which will provide experimental data with which to compare our results.

- Our results hopefully will be included in future partial-wave analysis and will lead to an improved understanding of isospin-$\frac{1}{2}$ N^* resonances in the third resonance region ($W \sim$ 1700 MeV).

- In principle, P_Λ (polarization of the final-state Λ) could be determined by measuring the angular distribution of the π^0 emitted in the decay $\Lambda \to \pi^0 n$, in the Λ's rest frame, but such a measurement needs better statistics.

Bibliography

[1] M. Gell-Mann, Phys. Lett. **8**, 214 (1964).

[2] J. H. Christenson, J. W. Cronin, V. L. Fitch, and R. Turlay, Phys. Rev. Lett. **13**, 138 (1980).

[3] I. H. Hleiqawi, Ph. D. Thesis, Ohio University (2006).

[4] C. Amsler *et al.* (Particle Data Group), Review of Particle Physics, Phys. Lett. B **667**, 1 (2008).

[5] physics Division Annual Report 2000, Argonne National Laboratory (ANL) (http://www.phy.anl.gov/division/publications/annualreport/2000/IVMedium.pdf.)

[6] M. Wolf *et al.*, Eur. Phys. J. A **9**, 5 (2000).

[7] M. Kotulla *et al.*, Phys. Lett. B **578**, 63 (2003).

[8] F. Renard *et al.*, Phys. Lett. B **528**, 215 (2002).

[9] M. Dugger *et al.*, Phys. Rev. Lett. **89**, 222002 (2002).

[10] S. Prakhov *et al.*, Phys. Rev. C **79**, 035204 (2009).

[11] K. H. Glander *et al.*, Eur. Phys. J. A **19**, 251 (2004).

[12] M. Sumihama *et al.*, Phys. Rev. C **73**, 035214 (2006).

[13] J. W. C. McNabb *et al.*, CLAS Collaboration, Phys. Rev. C 69, 042201 (2004).

[14] R. G. T. Zegers *et al.*, Phys. Rev. Lett. **91**, 092001 (2003).

[15] M. Q. Tran *et al.*, Phys. Lett. B **445**, 20 (1998).

[16] M. Bockhorst *et al.*, Z. Phys. C **63**, 37 (1994).

[17] R. Bradford *et al.* Phys. Rev. C **73**, 035202 (2006).

[18] E. Munevar, B. L. Berman, and P. Naddel-Turonski, (CLAS Collaboration), AIP Conf. Proc. **947**, 146 (2007).

[19] T. Watanabe *et al.*, Phys. Lett. B **651**, 269 (2007).

[20] A. Salam *et al.*, Phys. Rev. C **74**, 044004 (2006).

[21] T. Mart and C. Bennhold, Phys. Rev. C **61**, 12201 (2000).

[22] J. D. Jackson, Classical Electrodynamics, Wiley, New York (1999).

[23] H. Thom, Phys. Rev. **151**, 1322 (1966).

[24] R. A. Adelseck, C. Bennhold, and L. E. Wright, Phys. Rev. C **32**, 1681 (1985).

[25] R. A. Adelseck *et al.*, Phys. Rev. C **38**, 1965 (1988).

[26] J. C. David *et al.*, Phys. Rev. C **53**, 2613 (1996).

[27] R. L. Workman *et al.*, Phys. Rev. C **44**, 552 (1991).

[28] T. Mizutani *et al.*, Phys. Rev. C **58**, 75 (1998).

[29] R. A. Adelseck *et al.*, Phys. Rev. C **42**, 108 (1990).

[30] C. Bennhold *et al.*, Phys. Rev. C **39**, 927 (1989).

[31] F. X. Lee *et al.*, Nucl. Phys. A **695**, 237 (2001).

[32] T. Feuster and U. Mosel, Phys. Rev. C **59**, 460 (1999).

[33] P. Bydzovsky *et al.*, Nucl. Phys. A **754**, 243, (2005); P. Bydzovsky *et al.*, arXiv:nucl-th/0412035 (2004).

[34] M. Q. Tran *et al.*, Phys. Lett. B **464**, 331 (1999).

[35] C. Bennhold *et al.*, Nucl. Phys. A **639**, 209c (1998).

[36] K. Tsukada *et al.*, Phys. Rev. C **78**, 014001 (2008).

[37] H. Yamazaki *et al.*, Phys. Rev. C **52**, (1995) R1157.

[38] A. Jankowiak *et al.*, EPAC 2002, Paris, 1085 (2002).

[39] A. Jankowiak *et al.*, EPAC 2006, Edinburgh, Scottland, p. 834 (2006).

[40] A. Jankowiak *et al.*, EPAC 2008, Genoa, Italy, p. 51 (2008).

[41] J. C. McGeorge *et al.*, Eur. Phys. J. A **37**, 129 (2008).

[42] E. D. Bloom and C. W. Peck, Ann. Rev. Nucl. Part. Sci. **33**, 143 (1983).

[43] J. Albert, Diploma Thesis, Institute für Kernphysik, Johannes Gutenberg Universität Mainz, 2003.

[44] R. Novotny, IEEE Trans. Nucl. Sci. **33**, 379 (1991).

[45] D. Watts, Calorimetry in particle physics (pp 116-123), Proceedings of the Eleventh International Conference, Perugia, Italy (2004).

[46] C. Tarbert, Ph. D. Thesis, University of Edinburgh (2007); C. Tarbert *et al.*, Phys. Rev. Lett. **100**, 132301 (2008).

[47] J. R. M. Annand, Data Analysis within an AcquRoot Framework, University of Glasgow (2008).

[48] R. Brun and F. Rademakers *et al.*, ROOT User's Guide 4.16 CERN, (2006).

[49] F. Zehr, PhD Thesis, Universität Basel, (2008).

[50] J. W. Brudvik, Ph. D. Thesis, University of California, Los Angeles (2007).

[51] Constrained Least Square and Error Propagation, source code at http://www.desy.de/ blobel.

[52] R. J. J. Castelijins, Ph. D. Thesis, Kernfysisch Versneller Instituut, Rijksuniversiteit Groningen, Groningen (2006); R. Castelijns *et al.*, Eur. phys. J. A **35**, 39 (2008).

[53] S. Brandt, Data Analysis, Statistical and Computational Methods for Scientists and Engineers, Third Edition, Springer-Verlag (1998).

[54] N. Phaisangittisakul, Ph. D. Thesis, University of California, Los Angeles, (2001).

[55] GEANT - *Detector Description and Simulation Tool*, 1994. Application and Software Group, Computing and Network Division, CERN.

[56] B. Carnahan, Ph. D. Thesis, Catholic University of America, Washington (2003).

[57] S. V. Shende, Ph. D. Thesis, Kernfysisch Versneller Instituut, Rijksuniversiteit Groningen, Groningen (2007)

[58] R. Lawall *et al.*, Eur. Phys. J. A **24**, 275 (2005).

[59] D. L. Hornidge, Ph. D. Thesis, University of Saskatchewan, (1999).

[60] E. J. Downie, Ph. D. Thesis, University of Glasgow, (2006).

Appendix A

Analysis of $\gamma p \to K^0\Sigma^+$

In this appendix we describe our analysis of the reaction $\gamma p \to K^0\Sigma^+$. Some details that are similar to those described in Chapter 4 for the reaction $\gamma n \to K^0\Lambda$ are not repeated here. The differential cross section and the total cross section for $\gamma p \to K^0\Sigma^+$ will be presented and compared with prior results. The generally good agreement of our $\gamma p \to K^0\Sigma^+$ results with prior measurements provides support for our analysis procedures and therefore provides credibility to our results for $\gamma n \to K^0\Lambda$. Numerical results are tabulated in Appendix B.

A.1 Tagger random subtraction

The Tagger TDC (TimeOR) spectrum for this analysis is shown in Fig. 4.4, which shows that the prompt peak is at $\sim$105 ns and a nearly flat background of random coincidences spreads for the whole 200-ns-wide event window. Figure A.1 shows a timing spectrum for Tagger channel 25. (See Fig. 4.6 to compare at the same channel for the reaction $\gamma n \to K^0\Lambda$.) Random background subtraction for the K^0_S missing mass spectrum at photon energy $E_\gamma = 1300.9$ MeV is shown in Fig. A.2. The contribution of random events is represented by the red-filled histogram and the contribution of the coincident events is given by the green-filled histogram. The subtraction of these two histograms is shown fitted with a Gaussian distribution.

A.2 Confidence level and the number of degrees of freedom (NDF)

The analysis procedure used the same kinematic fit methods for event selection as for the reaction $\gamma n \to K^0\Lambda$ described in Sec. 4.6. Here, for a 6-cluster event to be identified as a candidate $\gamma p \to K^0\Sigma^+$ event, it had to have the largest confidence level (CL) for

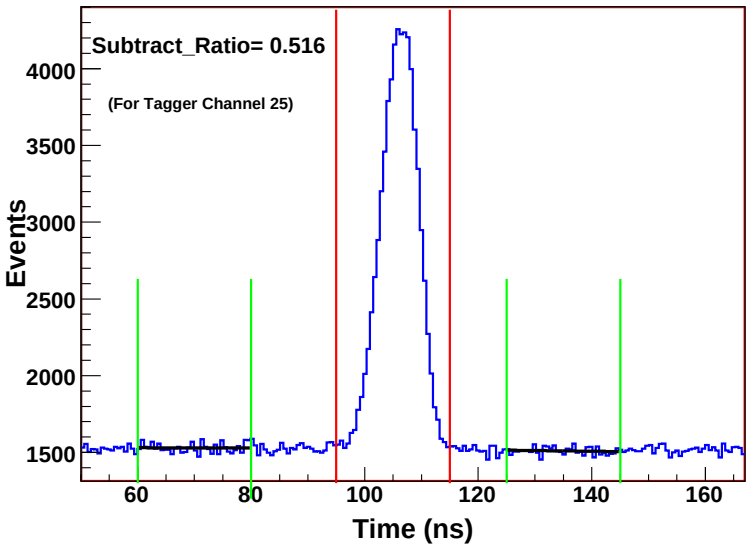

Figure A.1: Tagger timing spectrum for channel 25 for which the calculated ratio of the random-prompt areas was $r_{\mathrm{pr}} = 0.516$.

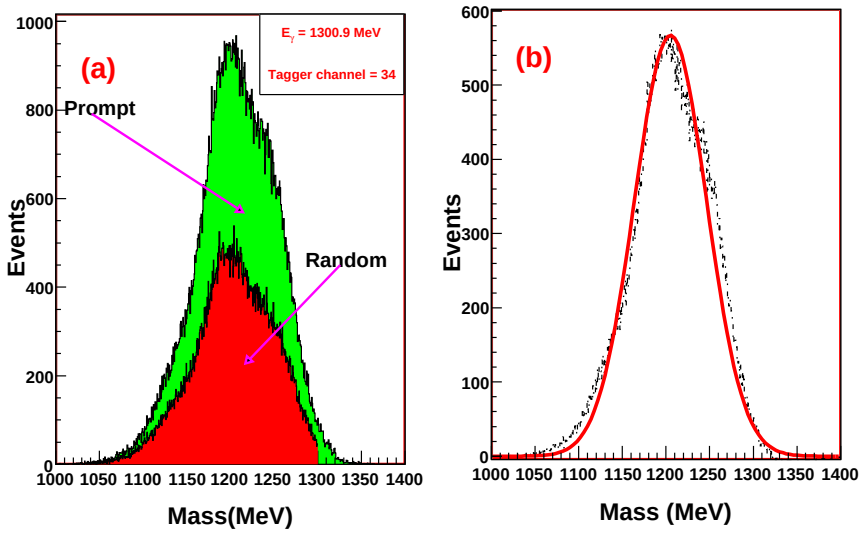

Figure A.2: Example of random background subtraction of missing mass of K^0 for Tagger channel 34 and incident photon energy 1300.9 MeV. (a) The red-filled histogram corresponds to random background events and the green-filled histogram is for the prompt coincident events. (b) The resulting histogram fitted with a Gaussian distribution after the subtraction of the two previous histograms using Eq. (4.2).

$\gamma p \to K^0\Sigma^+$, as compared with CL values for the other hypotheses tested. Figure A.3 shows the CL distribution for all identified $\gamma p \to K^0\Sigma^+$ events in our measured data. The events having largest values of χ^2 in the fit are located near the peak region close to CL = 0 whereas those with low χ^2 values are distributed close to CL = 1. The rest of the events are in the intermediate flat region. As the events near CL = 0 do not satisfy the constraint equations, those events are not of interest. A cut was placed on the confidence level as shown in the figure, so that events with CL < 0.15 were discarded.

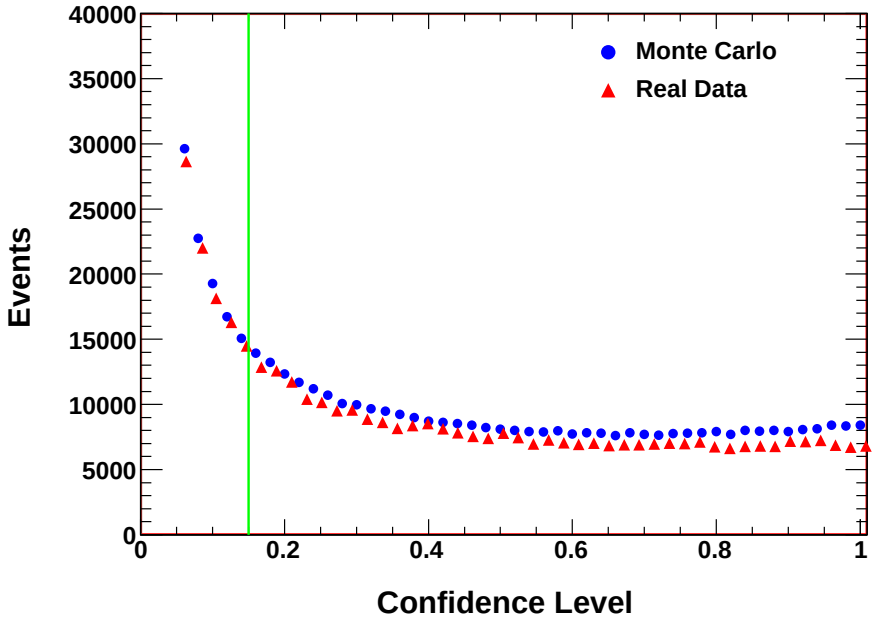

Figure A.3: Confidence level distributions for Monte Carlo simulation (blue circles) and for real data (red triangles) in the reaction $\gamma p \to K^0\Sigma^+$. The vertical line shows a CL cut placed at 0.15 for the selection of good events. This cut reduces 33% misidentified events from the real data.

As the momentum of each incident photon lies along the z-axis, the γp interaction point inside the target was a free variable in the kinematic fit. Figure A.4 shows the measured distribution of the z-coordinate of the interaction point inside the target, which is also considered as the **primary vertex**. Because of the short lifetimes of the Σ^+ and K^0_S, their decay lengths are comparable to the size of the target, and thus these were also

considered as free parameters in the kinematic fit.

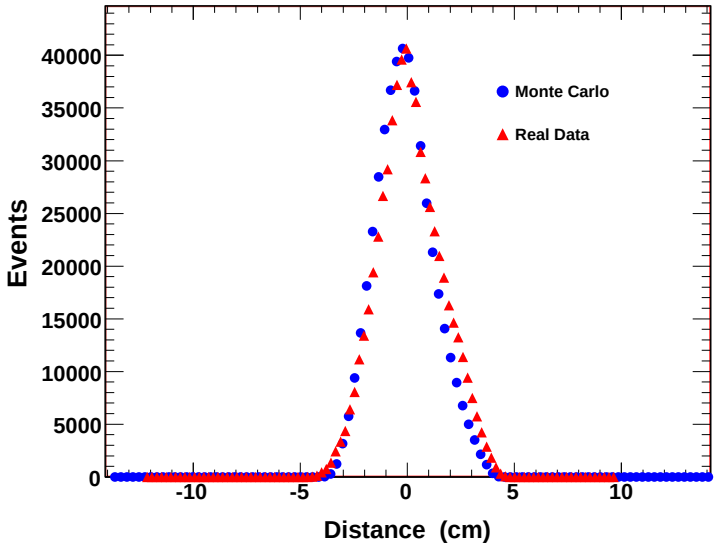

Figure A.4: The z coordinate of the incident beam for Monte Carlo simulation (blue circles) and for real data (red triangles) in the reaction $\gamma p \to K^0\Sigma^+$. It is considered as the **primary vertex** in our analysis.

The decay chain used to identify $\gamma p \to K^0\Sigma^+$ events was $\gamma p \to K^0_S\Sigma^+ \to (\pi^0\pi^0)(\pi^0 p) \to 6\gamma p$. The number of unmeasured quantities for the six-cluster $\gamma p \to K^0\Lambda$ events was six: the z coordinate of the vertex position, the Σ^+ and K^0_S decay lengths, energy, and the two angles (θ and ϕ) of the final-state protons. There are nine constraints: four for momentum (p_x, p_y, p_z) and energy conservation, three for the mass of each π^0, one for the K^0 mass, and one for the Σ^+ mass. Therefore, the NDF in our analysis of $\gamma p \to K^0\Sigma^+$, which supposes that the final-state proton is undetected, is NDF = $9 - 6 = 3$.

A.3 Event selection

The neutral mesons (π^0, K^0_S) and baryons (Σ^+) have a very short lifetime, so only the photons resulting from their decays were detected (e.g., $K^0_S \to 2\pi^0, \Sigma^+ \to \pi^0 p, \pi^0 \to 2\gamma$). When a particle decays, its momentum four-vector is conserved. Consequently, the

momentum four-vector of a neutral meson is equal to the sum of the momentum four-vectors of the photons resulting from its decay.

Figure A.5 shows the invariant mass distribution of 2γ for all possible combinations of six photons in the final state for $\gamma p \rightarrow K_S^0\Sigma^+ \rightarrow 3\pi^0 p \rightarrow 6\gamma p$ to produce a peak around the mass of π^0.

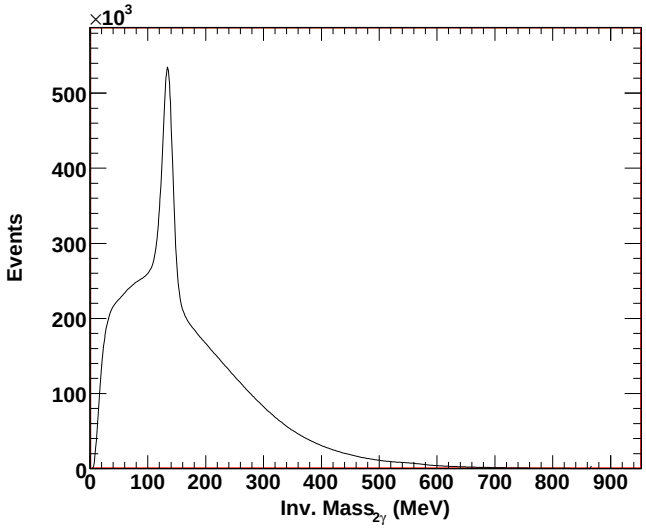

Figure A.5: The invariant mass distribution of 2γ for all combinations of two out of six photons in the final state for $\gamma p \rightarrow K_S^0\Sigma^+ \rightarrow 3\pi^0 p \rightarrow 6\gamma p$.

The identification of the different particles (e.g., K_S^0, Σ^+, proton) was made by following the same process described in Sec. 4.7. The invariant mass distribution of the four photons from a K_S^0 decay should be centered at 497 MeV, the mass of the K_S^0, as shown in Fig. A.6. These four photons are assumed to be from the decay of two π^0s and are determined by applying the **best pion combination** as described in Sec. 4.7.4. A two-dimensional view of the invariant mass of the selected pion pairs obtained from the decay of K_S^0 is shown in Fig. A.8, and a one-dimensional view of the invariant mass of these selected pion pairs is shown in Fig. A.9.

The missing mass distribution of the four photons that came from the K_S^0 decay should be centered around the mass of the Σ^+ (at 1189 MeV), as shown in Fig. A.7.

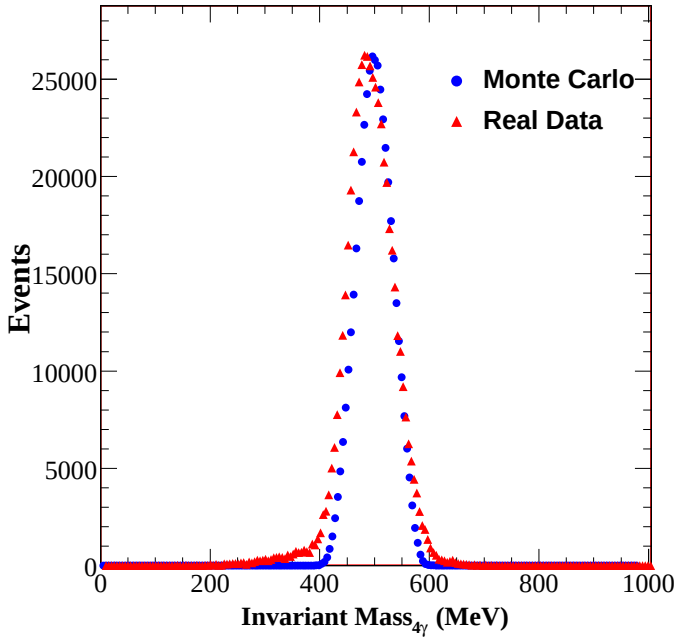

Figure A.6: The distribution of invariant mass for the four photons identified as coming from $\gamma p \to K^0\Sigma^+$ followed by $K_S^0 \to 2\pi^0 \to 4\gamma$. The peak is near the mass (497.6 MeV) of the neutral kaon.

Figure A.10 shows the missing mass of the six photons identified as coming from $\gamma p \to K_S^0\Sigma^+ \to 3\pi^0 p \to 6\gamma p$. There is a distinct peak at the mass of the proton (938 MeV) as expected.

A.4 Background subtraction

As mentioned in Sec. 4.9, we can investigate the experimental background for $\gamma p \to K^0\Sigma^+$ using a Monte Carlo analysis. For this purpose we simulated data for various reactions and analyzed these data using the fitting hypothesis of the reaction $\gamma p \to K^0\Sigma^+$. Those events for other reactions that survived the selection tests for $\gamma p \to K^0\Sigma^+$ were counted as backgrounds. In order for a real event to be accepted as a viable $\gamma p \to K^0\Sigma^+$

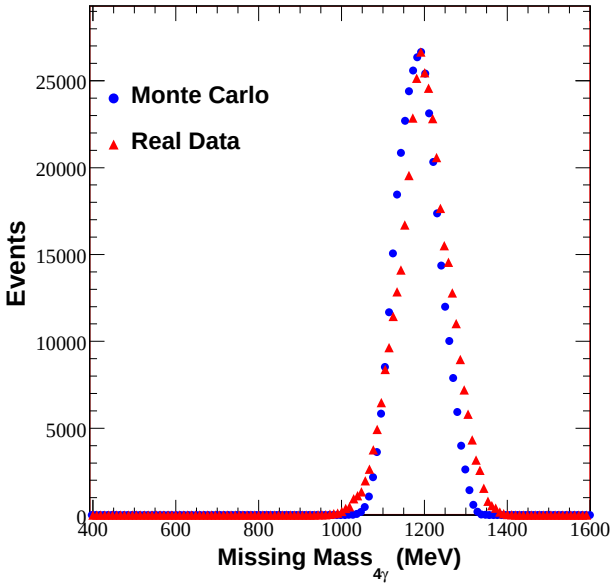

Figure A.7: The distribution of missing mass for the four photons identified as coming from $\gamma p \to K^0\Sigma^+$ followed by $K^0_S \to 2\pi^0 \to 4\gamma$. The peak is near the mass (1189 MeV) of the Σ^+ hyperon.

candidate, it should have the highest confidence level for this hypothesis compared to any other hypothesis. Finally, to be acceptable, it should have CL $>$ 0.15.

We considered the following possible background reactions: (i) $\gamma n \to K^0\Lambda$, (ii) $\gamma n \to K^0\Sigma^0$, (iii) $\gamma N \to \eta N$, and (iv) $\gamma N \to 3\pi^0 N$. The average survival probabilities that the simulated events satisfied the selection tests for $\gamma p \to K^0\Sigma^+$ are summarized in Table A-1.

All considered background reactions have at least a 6γ final state so all of these reactions were considered as 6-cluster events in the analysis, the same as for the reaction $\gamma n \to K^0\Lambda$. For the real data, the backgrounds due to these reactions were estimated using a Monte Carlo simulation and the measured number of $K^0\Lambda$, $K^0\Sigma^0$, ηN, and $3\pi^0 N$ events in the real data. Let us suppose that $N^{K^0_S\Sigma^+}_{\rm data}$, $N^{K^0_S\Lambda}_{\rm data}$, $N^{K^0_S\Sigma^0}_{\rm data}$, $N^{\eta N}_{\rm data}$, and $N^{3\pi^0 N}_{\rm data}$ are the corresponding known numbers of $K^0_S\Sigma^+$, $K^0_S\Lambda$, $K^0_S\Sigma^0$, ηN, and $3\pi^0 N$ events in the real data. As described in Sec. 4.10.2, the number of real signal $N^{K^0_S\Sigma^+}_{\rm signal}$ events for

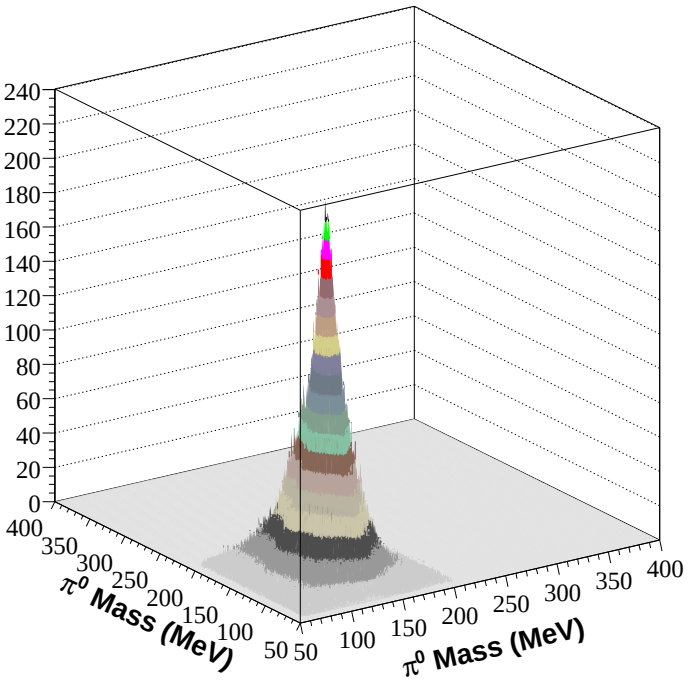

Figure A.8: Two-dimensional plot of invariant masses of the reconstructed π^0 pairs from the decay of K^0_S as $K^0_S \to 2\pi^0 \to 4\gamma$ for $\gamma p \to K^0\Sigma^+$ events.

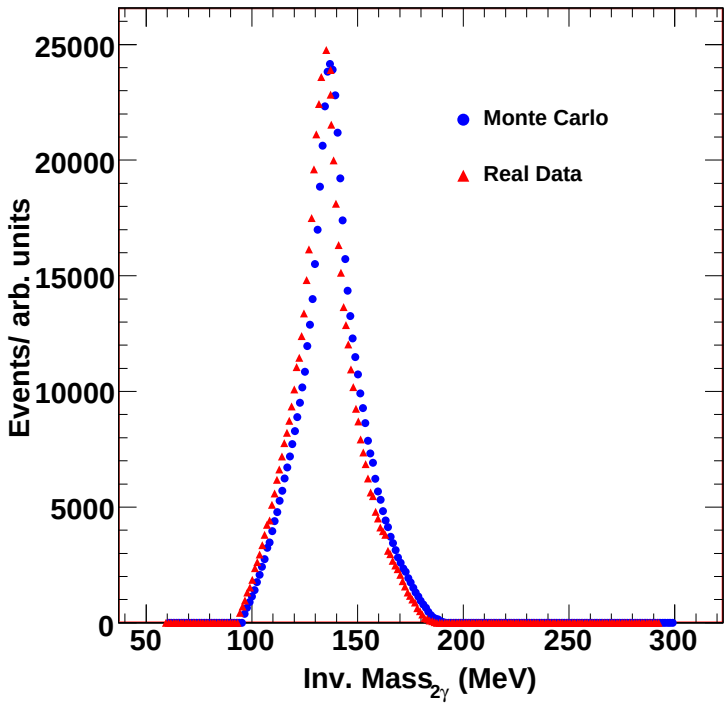

Figure A.9: The distribution of invariant mass for the two photons identified as coming from $K_S^0 \to 2\pi^0$ followed by $\pi^0 \to 2\gamma$. The peak is near the mass (135.0 MeV) of the neutral pion.

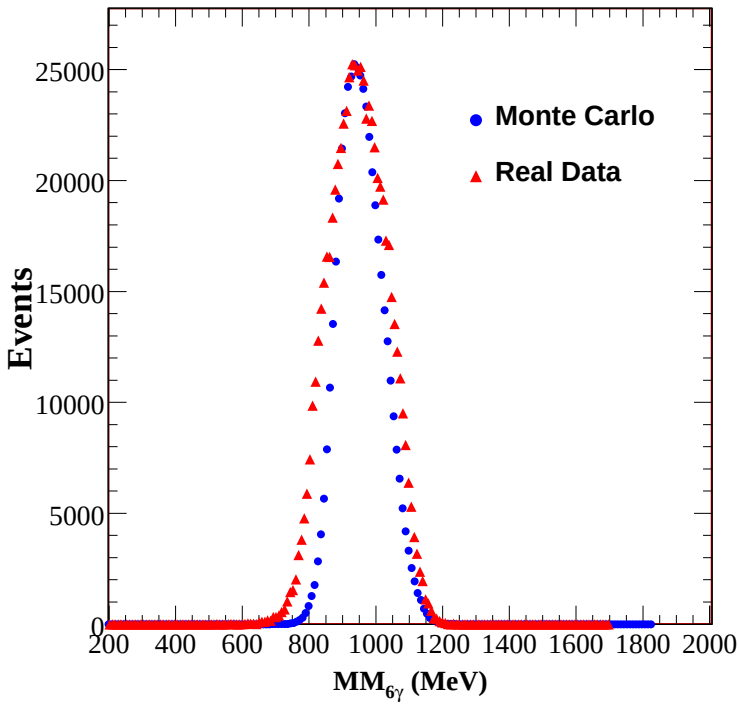

Figure A.10: The distribution of missing mass of the six photons identified as coming from $\gamma p \to K^0_S \Sigma^+ \to 3\pi^0 p \to 6\gamma p$. The peak is near the mass (938.3 MeV) of the proton.

background channels	**survival probability**
$\gamma n \to K_S^0 \Lambda$	0.99%
$\gamma n \to K_S^0 \Sigma^0$	0.74%
$\gamma N \to \eta N$	0.17%
$\gamma N \to 3\pi^0 N$	0.30%

Table A-1: Survival probability for several background reactions to $\gamma p \to K^0\Sigma^+$ calculated from Monte Carlo analysis.

$\gamma p \to K_S^0\Sigma^+$ is given as

$$N_{\rm signal}^{K_S^0\Sigma^+} = N_{\rm data}^{K_S^0\Sigma^+} - N_{\rm data}^{K_S^0\Lambda}\varepsilon_{\rm MC}(K_S^0\Sigma^+/K_S^0\Lambda) - N_{\rm data}^{K_S^0\Sigma^0}\varepsilon_{\rm MC}(K_S^0\Sigma^+/K_S^0\Sigma^0) - N_{\rm data}^{\eta N}\varepsilon_{\rm MC}(K_S^0\Sigma^+/\eta N) - N_{\rm data}^{3\pi^0 N}\varepsilon_{\rm MC}(K_S^0\Sigma^+/3\pi^0 N). \quad \text{(A.1)}$$

I.e., we can subtract the background events from our analysis and compute the actual number of $\gamma p \to K^0\Sigma^+$ events. In addition to the above mentioned background sources, there is another source due to empty target data. The method of the empty target subtraction is described in Sec. 4.14.

A.5 Secondary vertex and decay correction for K_S^0 and Σ^+

As described in Chapter 4, it was assumed that the initial electromagnetic interaction occurs at the primary vertex where K_S^0 and Σ^+ are produced in the reaction $\gamma p \to K^0\Sigma^+$. Because of their lifetimes, $\tau_{\Sigma^+} = 0.08018$ ns for Σ^+ and $\tau_{K_S^0} = 0.08935$ ns for K_S^0, these particles can travel a few centimeters from the point at which they were produced before

they undergo a weak decay. In order to find the positions of the secondary vertices (where these particles decay), their momenta must be known. The positions of the secondary vertexes for K^0 and Σ^+ were reconstructed by using the kinematic fit as described in Sec 4.11.

The reconstructed distributions of the distance traveled by K^0 and Σ^+ after their production at the primary vertex are shown in Figs. A.11(a) and (c). The lifetimes of these particles were calculated by using Eq. (4.37). The distributions of the lifetime are shown in Figs. A.11(b) and (d). Linear fits of the lifetime distributions are shown in Figs. A.12(a) and (b). The reciprocal of the slope of these fits provides the respective mean lifetimes of the K^0_S and Σ^+. The PDG values [4] of the mean lifetime for K^0_S and Σ^+ are $(0.895 \pm 0.0005) \times 10^{-10}$ s and $(0.8018 \pm 0.0026) \times 10^{-10}$ s, respectively. The values from our fit are $(0.961 \pm 0.032) \times 10^{-10}$ s for K^0_S and $(0.973 \pm 0.024) \times 10^{-10}$ s for Σ^+.

A.6 Acceptance and efficiency determination

The acceptance for $\gamma p \to K^0\Sigma^+$ was determined from a Monte Carlo simulation as described in Sec. 4.12. Approximately 17 million events for K^0_S with a phase-space distribution of energy and momentum were simulated in the energy range E_γ = (1050 - 1430) MeV. The simulated data were treated in exactly the same manner as the experimental data with both analyzed using the same code. Figure A.13 shows the calculated acceptance for $\gamma p \to K^0\Sigma^+$ plotted as a function of the center-of-mass angle of the K^0_S ($\Theta^K_{\rm CM}$) for different energy bins. Figure A.14 shows the detector efficiency for $\gamma p \to K^0\Sigma^+$ as a function of the incident photon energy. It indicates that the efficiency remains about a 5% for incident photon energies below 1200 MeV, and falls to about 2% at a photon energy of 1400 MeV.

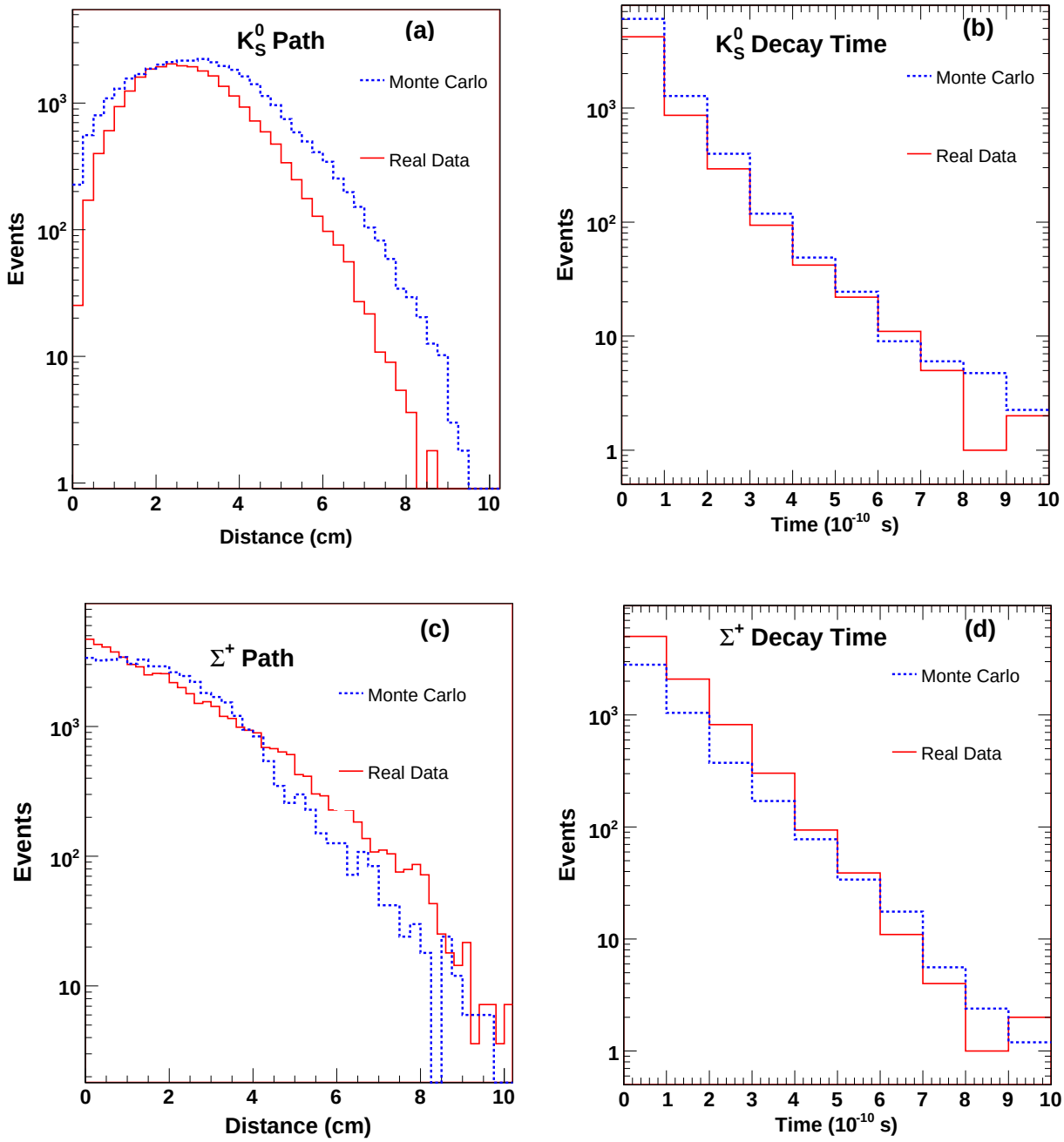

Figure A.11: (a) The distributions of the distance traveled by K^0 before its decay for Monte Carlo simulation (blue dashed line) and for real data (red solid line). (b) The distribution of the lifetime of K^0_S for Monte Carlo simulation (blue dashed line) and for real data (red solid line). (c) The distribution of the distance traveled by Σ^+ before its decay for Monte Carlo simulation (blue dashed line) and for real data (red solid line). (d) The distribution of the lifetime of Σ^+ for Monte Carlo simulation (blue dashed line) and for real data (red solid line).

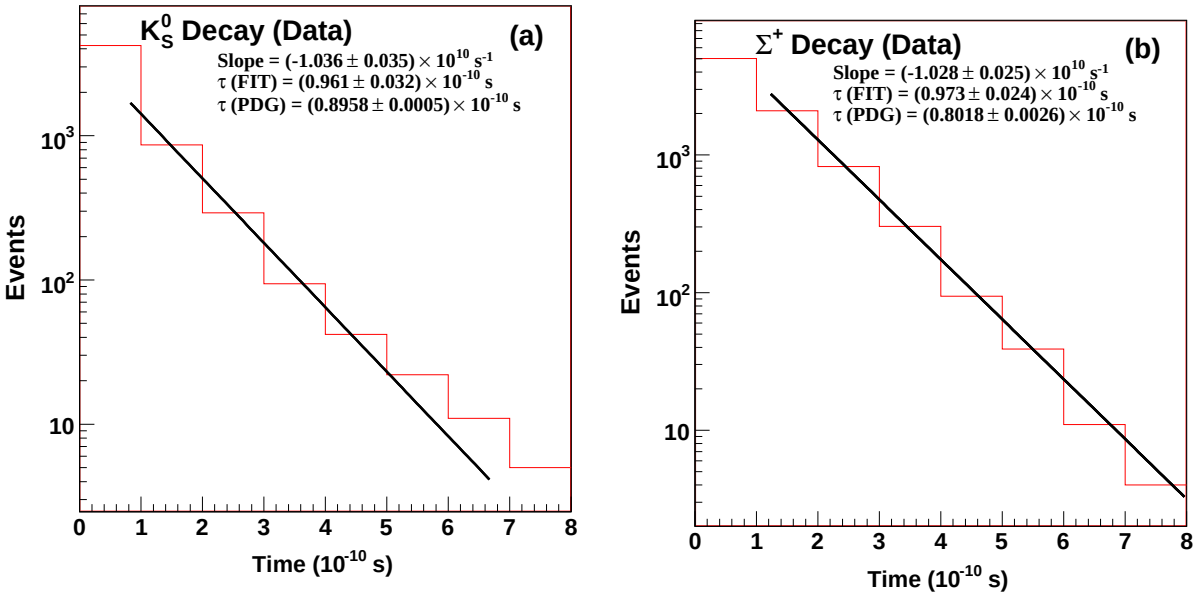

Figure A.12: (a) The distribution of the lifetime for the K^0_S with fit values $(0.961 \pm 0.032) \times 10^{-10}$ s and the PDG values [4], $(0.895 \pm 0.0005) \times 10^{-10}$ s. (b) The distribution of the lifetime for the Σ^+ with fit values $(0.973 \pm 0.024) \times 10^{-10}$ s and the PDG values [4], $(0.8018 \pm 0.0026) \times 10^{-10}$ s.

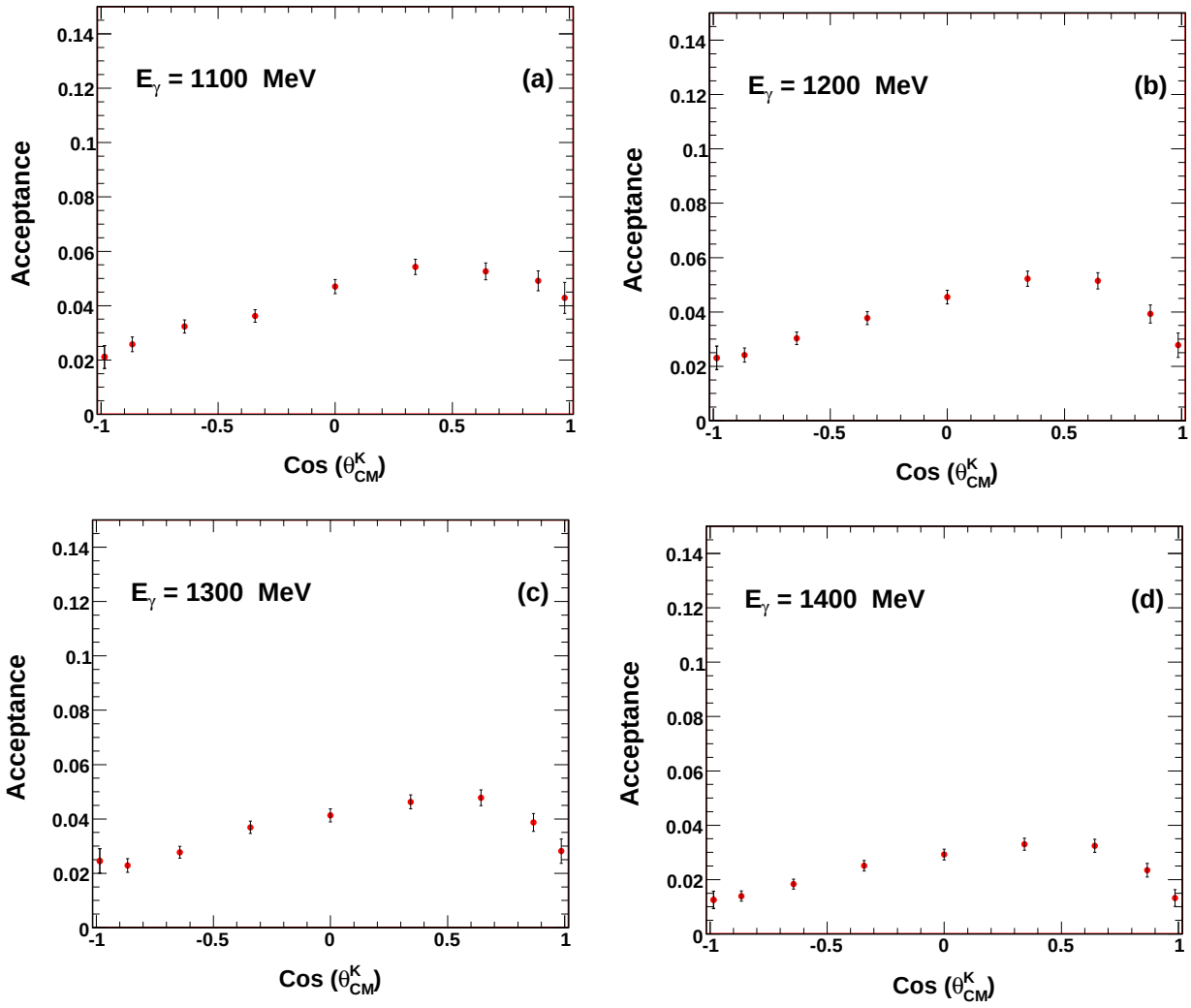

Figure A.13: The acceptance for $\gamma p \to K^0\Sigma^+$ as a function of $\cos(\theta^K_{\rm CM})$ at beam energies between 1100 and 1400 MeV.

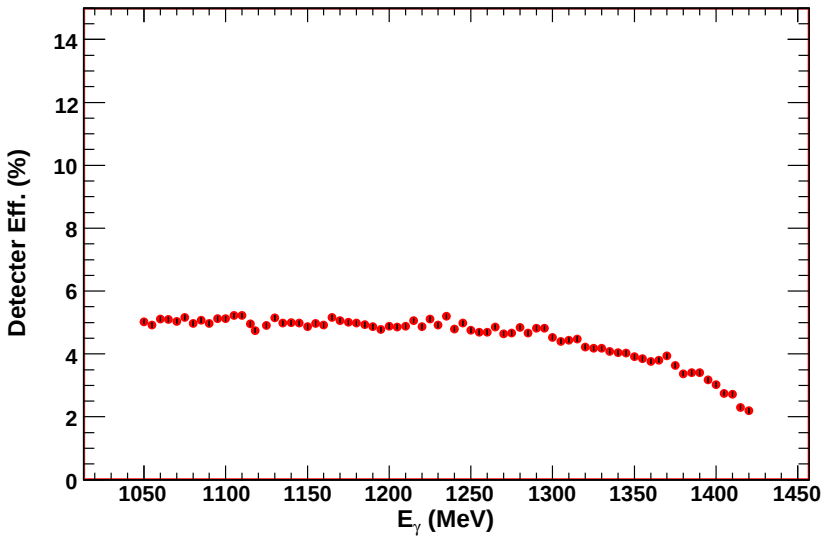

Figure A.14: Detector efficiency for $\gamma p \to K^0\Sigma^+$ events as a function of incident photon energy.

A.7 Result of background subtraction

Table A-1 lists several background reactions ($\gamma n \to K^0\Lambda$, $\gamma n \to K^0\Sigma^0$, $\gamma N \to \eta N$, and $\gamma N \to 3\pi^0 N$) to the reaction $\gamma p \to K^0\Sigma^+$. These reactions contribute a significant number of events that look like $\gamma p \to K^0\Sigma^+$. By using Eq. (4.35), the number of background events due to each of these reactions can be estimated in the experimental data. As defined in Sec. 4.10.2, $\varepsilon_{\rm MC}(K^0_S\Sigma^+/K^0_S\Lambda)$, $\varepsilon_{\rm MC}(K^0_S\Sigma^+/K^0_S\Sigma^0)$, $\varepsilon_{\rm MC}(K^0_S\Sigma^+/\eta N)$, and $\varepsilon_{\rm MC}(K^0_S\Sigma^+/3\pi^0 N)$ represent the contamination ratio for the corresponding background reactions $\gamma n \to K^0_S\Lambda$, $\gamma n \to K^0_S\Sigma^0$, $\gamma N \to \eta N$, and $\gamma N \to 3\pi^0 N$.

In order to determine the differential cross section for $\gamma p \to K^0\Sigma^+$, it was necessary to find the angular distributions of $\varepsilon_{\rm MC}$ in each E_γ bin. Figure A.15 shows the angular distributions of the contamination ratios $\varepsilon_{\rm MC}$ at E_γ = 1200 MeV for the various background reactions to $\gamma p \to K^0\Sigma^+$. The angular variations of $\varepsilon_{\rm MC}$ for each of the background channels are not similar. For $\gamma p \to K^0\Sigma^+$, the ratio increases at forward angles. The angular variations of the $\varepsilon_{\rm MC}$ ratios show similar trends at other energies.

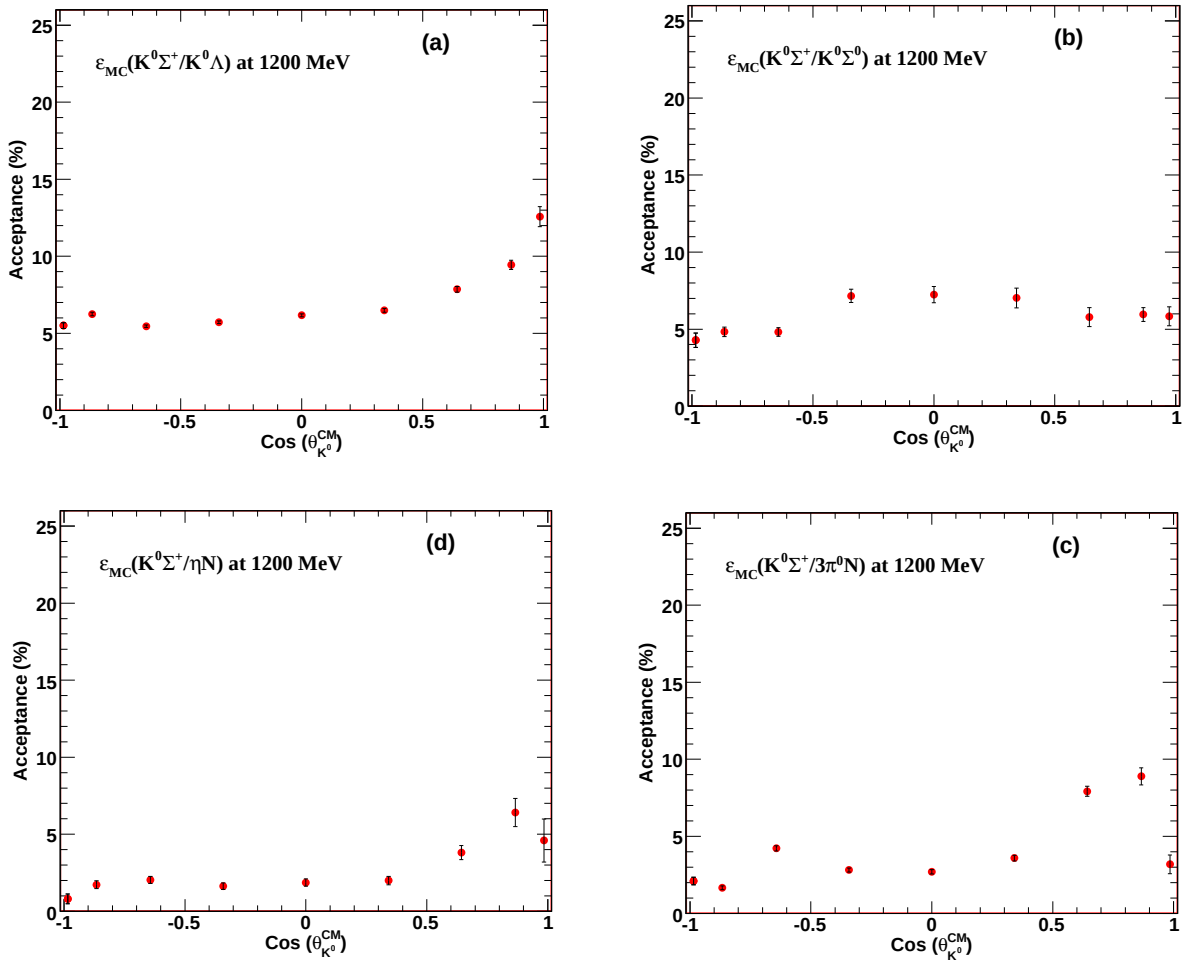

Figure A.15: Angular distributions of contamination ratio $\varepsilon_{\rm MC}$ for the reaction $\gamma p \to K^0\Sigma^+$ at E_γ = 1200 MeV due to (a) $\gamma n \to K^0\Lambda$, (b) $\gamma n \to K^0\Sigma^0$, (c) $\gamma N \to \eta N$, and (d) $\gamma N \to 3\pi^0 N$. The angular distributions for other energy bins are similar.

A.8 The differential cross section for $\gamma p \to K^0\Sigma^+$

The differential cross section for $\gamma p \to K^0\Sigma^+$ was calculated using Eq. A.2 for a given photon energy, E_γ, and center-of-mass kaon angle, $\theta^K_{\rm CM}$, as

$$\frac{d\sigma}{d\Omega}(E_\gamma,\theta_{\rm CM}) = \frac{N_{\rm events}(E_\gamma,\theta_{\rm CM})}{N_\gamma(E_\gamma)\times\varepsilon_{\rm accept}(E_\gamma,\theta_{\rm CM})\times N_{\rm target}\times\mathcal{BR}\times[2\pi\Delta\cos\theta_{\rm CM}]}. \quad \text{(A.2)}$$

Most of these symbols were defined in Sec. 5.1. Here, the product of branching ratios $\mathcal{BR}$ for the reaction $\gamma p \to K^0\Sigma^+$ is given as

$$\mathcal{BR}(\gamma p \to K^0_S\Sigma^+ \to \pi^0\pi^0\pi^0 p \to 6\gamma p) = \mathcal{B}(K^0 \to K^0_S)\times \\ \mathcal{B}(K^0_S \to 2\pi^0) \times \mathcal{B}(\Sigma^+ \to \pi^0 p) \times \mathcal{B}(\pi^0 \to \gamma\gamma)^3, \tag{A.3}$$

where [4]:

$$\begin{aligned} \mathcal{B}(K^0 \to K^0_S) &= 0.05, \\ \mathcal{B}(K^0_S \to 2\pi^0) &= 0.3069 \pm 0.0005, \\ \mathcal{B}(\Sigma^+ \to \pi^0 p) &= 0.5157 \pm 0.0030, \\ \mathcal{B}(\pi^0 \to \gamma\gamma) &= 0.98798 \pm 0.00032. \end{aligned}$$

Thus, numerically

$$\begin{aligned} \mathcal{BR}(\gamma p \to K^0_S\Sigma^+ \to \pi^0\pi^0\pi^0 p \to 6\gamma p) &= (0.5) \times (0.3069 \pm 0.0005) \times \\ &\quad (0.5157 \pm 0.0030) \times (0.98798 \pm 0.00032)^3 \\ &= 0.07629 \pm 0.00046 \end{aligned}$$

$\varepsilon_{\rm accept}(E_\gamma, \theta^K_{\rm CM})$ is the acceptance calculated from Monte Carlo simulation as described in Sec. A.6. Similarly, the terms $N_\gamma(E_\gamma)$, and $N_{\rm target}$ were evaluated as described in Sec. 5.1.

The differential cross section was measured at 14 incident photon energies: 1050, 1175, 1100, 1125, 1150, 1175, 1200, 1225, 1250, 1275, 1300, 1325, 1350, and 1375 MeV. In each energy bin, $d\sigma/d\Omega$ was evaluated in nine angular bins that ranged from -0.95 to 0.95 in $\cos\theta^K_{CM}$.

Figure A.16 shows $d\sigma/d\Omega$ at each of the 14 energy bins. Numerical results are tabulated in Appendix B. The curves through the data points were obtained by fitting the data with a series of Legendre polynomials using coefficients A_n up to n = 2. The error bars include statistical uncertainties only. The differential cross section at the lowest energies is nearly isotropic, which indicates that the threshold region is s-wave dominated. Between 1075

MeV and 1275 MeV, the angular distribution has a concave bowl shape, which changes to a convex bowl shape between 1300 and 1375 MeV.

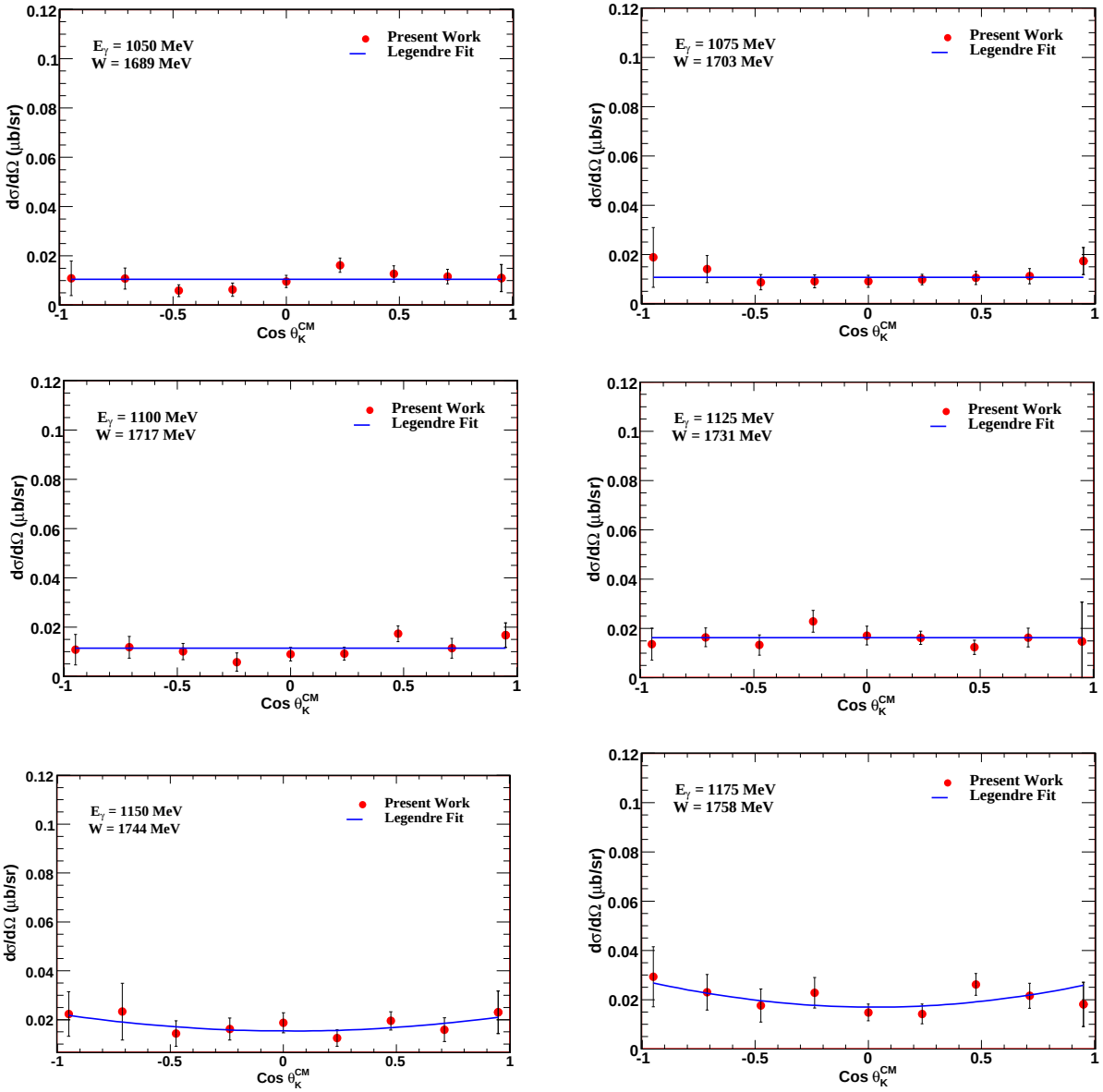

Figure A.16: Differential cross section in the center-of-mass system for the reaction $\gamma p \rightarrow K^0\Sigma^+$ at incident photon energies E_γ between 1050 and 1375 MeV. The solid curves are the results of the Legendre polynomial fits to our data.

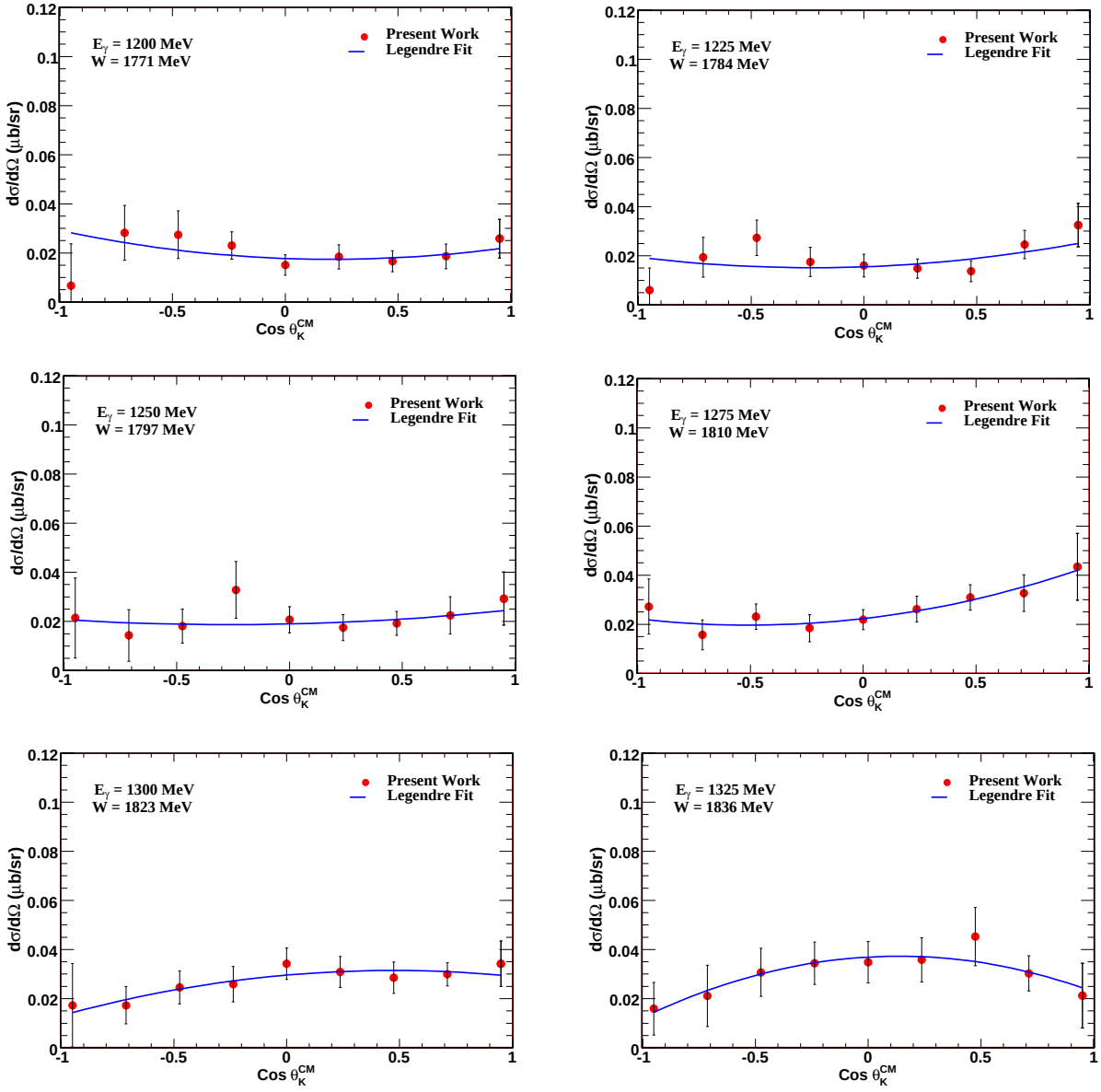

Figure A.16: Continued.

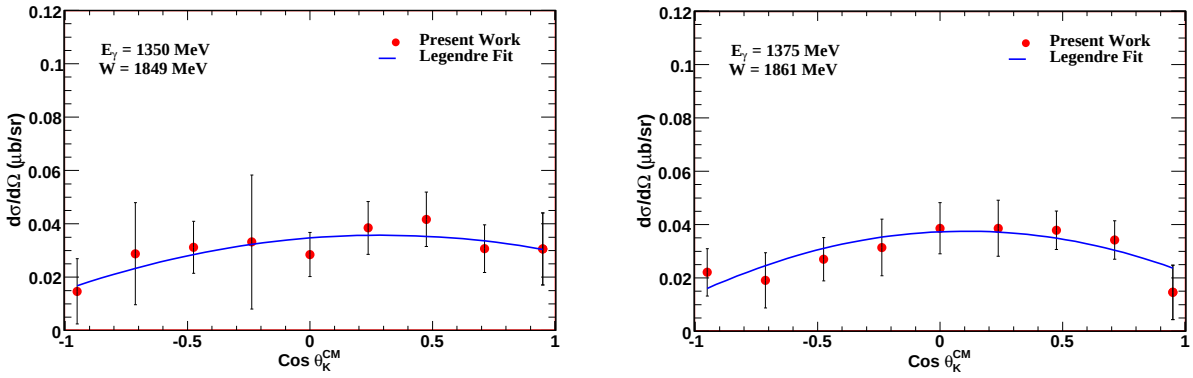

Figure A.16: Continued.

A.8.1 Comparison with prior results

Figure A.17 shows a comparison of our $d\sigma/d\Omega$ measurements at E_γ bins of 1100, 1200, and 1300 MeV with the CB-ELSA/TAPS data, which were measured using a liquid hydrogen target [52]. In general, the two sets of measurements are in good agreement, but our results have smaller statistical uncertainties.

A.8.2 Legendre fitting coefficients

The Legendre coefficients obtained by fitting $d\sigma/d\Omega$ for the reaction $\gamma p \to K^0\Sigma^+$ are plotted in Fig. A.18 and tabulated in Appendix D. The Legendre fits were obtained for maximum values of n between 2 and 4. Fitted values of A_3/A_0 and A_4/A_0 were found to be consistent with zero over the entire energy range. Therefore, our final fits used a maximum value of n = 2 and these are the results displayed in Fig. A.16. As exceptional cases, the values of A_1/A_0 and A_2/A_0 were found to be consistent with zero for $E_\gamma =$ 1050 to 1125 MeV; thus, data at these energies were fitted only with A_0. A_1/A_0 was found to be positive for energies above $\sim$ 1200 MeV, while A_2/A_0 is positive for 1125 MeV $\leq E_\gamma \leq$ 1290 MeV and negative for $E_\gamma \geq$ 1290 MeV.

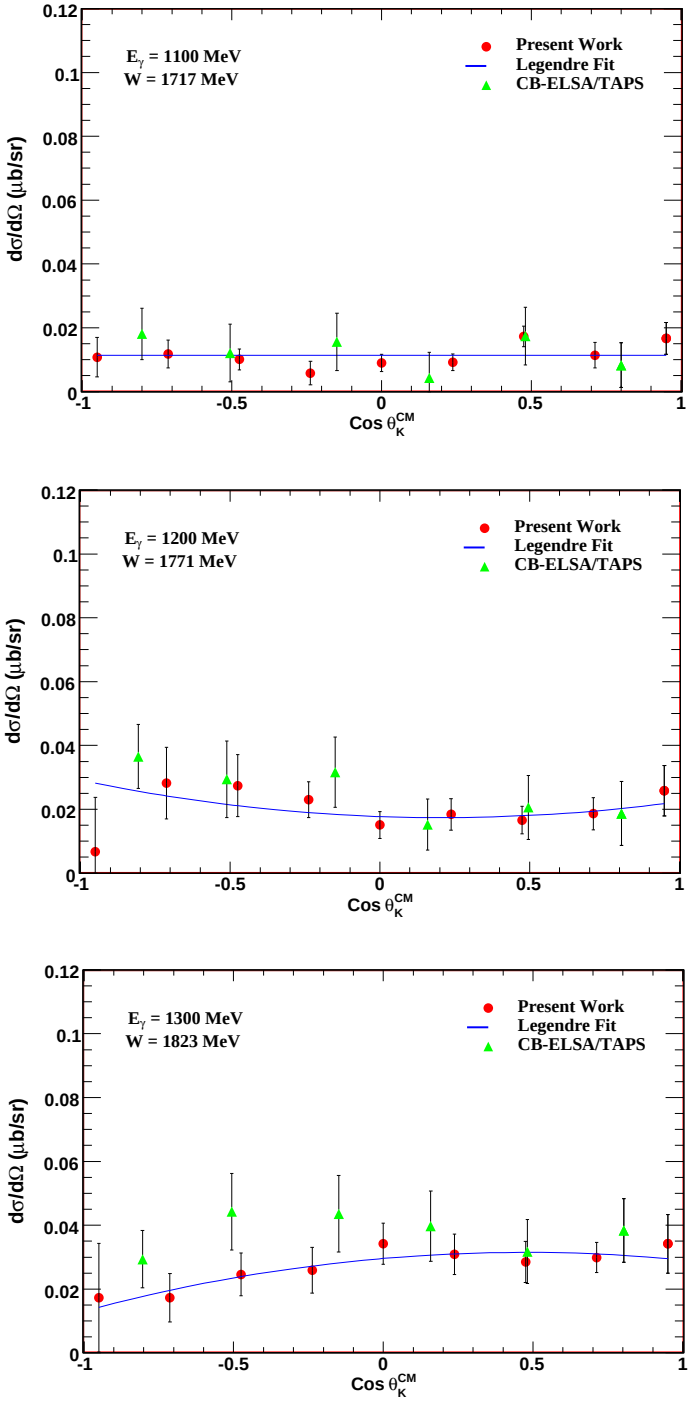

Figure A.17: Differential cross section for the reaction $\gamma p \to K^0\Sigma^+$ from this work (red solid circles) compared to measurements by CB-ELSA/TAPS [52] (green triangles) at incident photon energies of E_γ = 1100, 1200, and 1300 MeV. The solid curves are the results of Legendre polynomial fits to our data. Only statistical uncertainties are displayed.

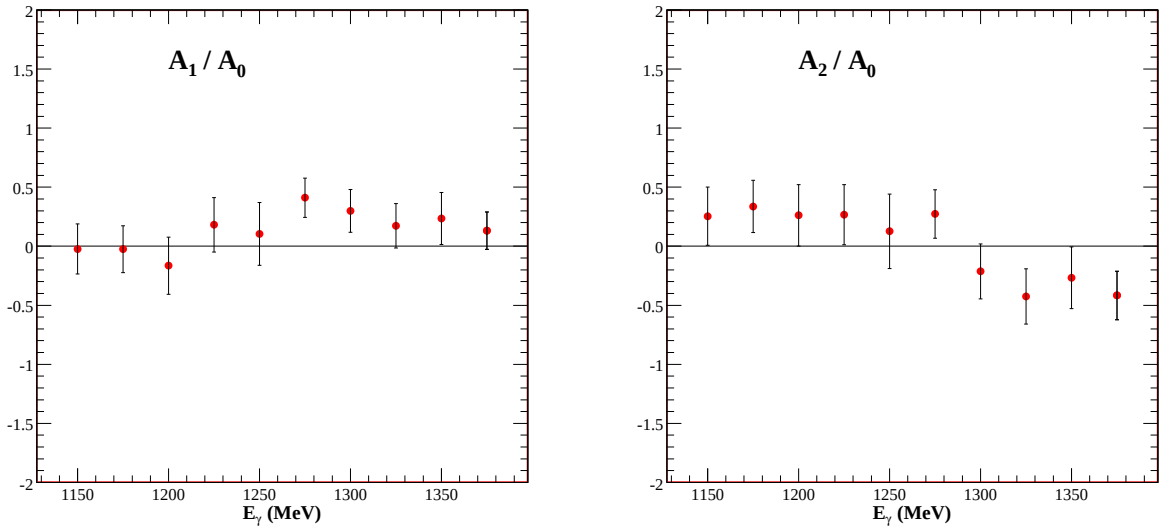

Figure A.18: Legendre coefficients obtained by fitting $d\sigma/d\Omega$ for $\gamma p \to K^0\Sigma^+$.

A.8.3 Total cross section for $\gamma p \to K^0\Sigma^+$

The amount of background to be subtracted from $\gamma p \to K^0\Sigma^+$ can be calculated using the values of the contamination ratios as described in Sec. A.7 and Eq. (4.35). Figure A.19 shows the measured total cross section for $\gamma p \to K^0\Sigma^+$ without background subtraction and the estimated background stemming from all the background reactions ($\gamma n \to K^0\Lambda$, $\gamma n \to K^0\Sigma^0$, $\gamma N \to \eta N$, and $\gamma N \to 3\pi^0 N$) and the empty target. The background contributions were computed on a bin-by-bin basis. Figure A.20 shows $\sigma_{\rm tot}(\gamma p \to K^0\Sigma^+)$ obtained after the background subtraction as a function of center-of-mass energy W. The values of $\sigma_{\rm tot}$ are tabulated in Appendix B. The total cross section gradually increases as E_γ increases. Because of limitations of the photon flux, we could not extract the total cross section beyond 1870 MeV. The statistical uncertainties associated with $\sigma_{\rm tot}$ in our work vary from 5 to 15%.

The percentage background contributions to $\sigma_{\rm tot}(\gamma p \to K^0\Sigma^+)$ stemming from all four background reactions and the empty target are tabulated in Appendix E. The empty target contributes about 1-2% to the total background. The total percentage background

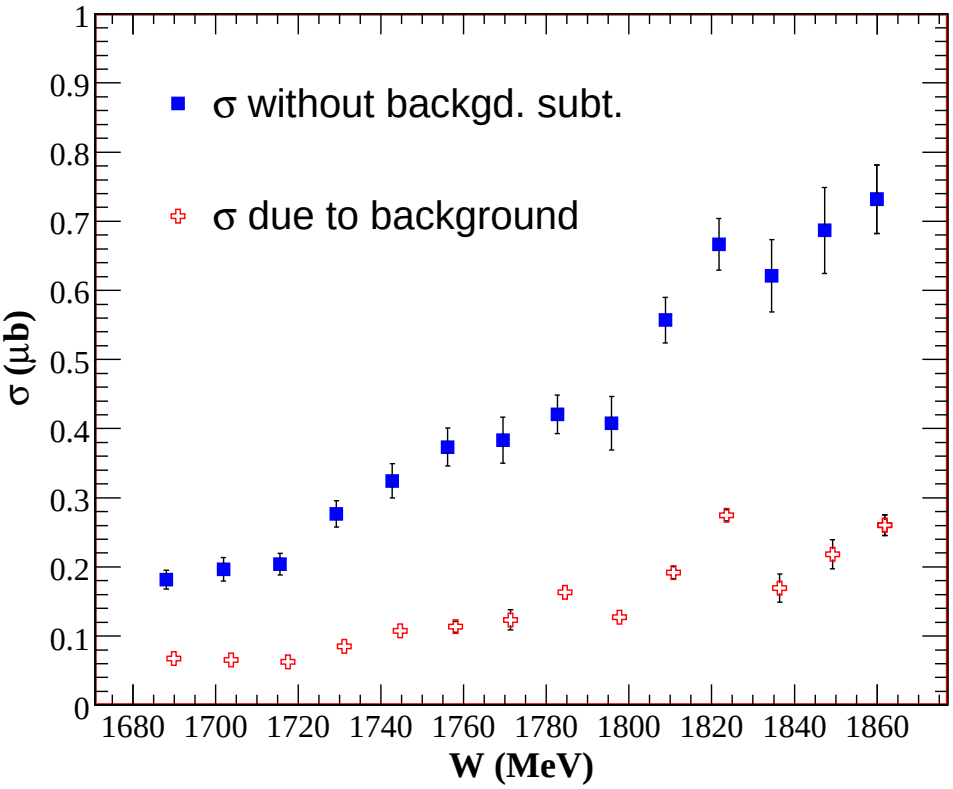

Figure A.19: The total cross section for $\gamma p \to K^0\Sigma^+$ without subtraction of background (filled squares) and estimation of the total contribution of background stemming from the background reactions and the empty target (open crosses) as described in the text.

contribution varies from about 32-47%. The individual reactions $\gamma p \to K^0\Lambda$, $\gamma n \to K^0\Sigma^0$, $\gamma N \to \eta N$, and $\gamma N \to 3\pi^0 N$ contribute 25-35%, 4-6%, 2-3%, and 1-2% to the total background, respectively.

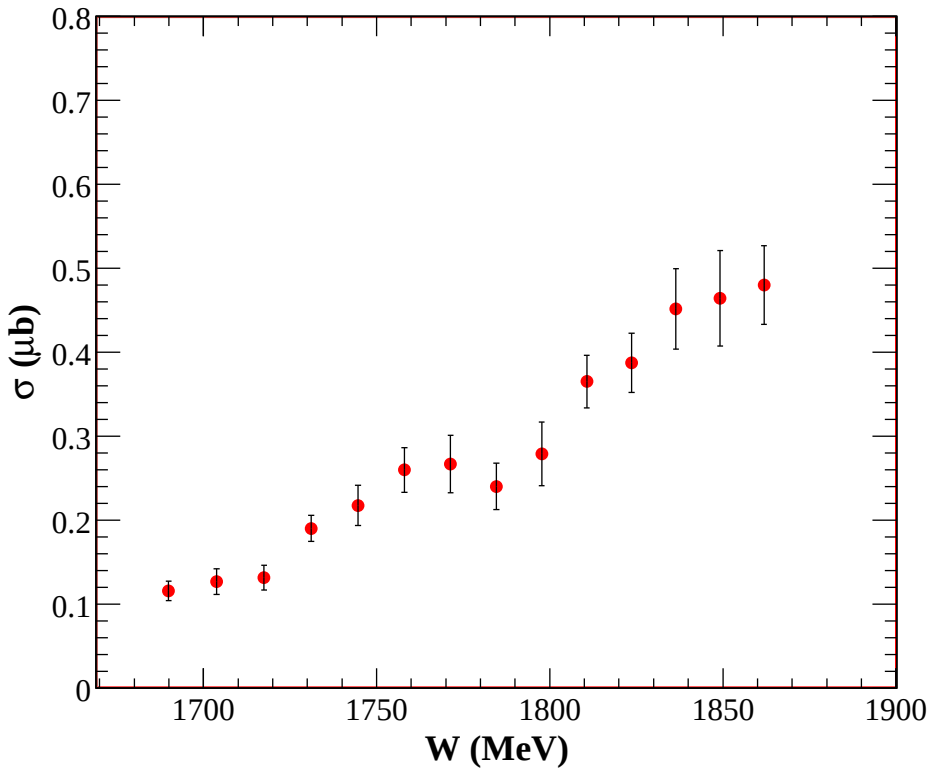

Figure A.20: The total cross section for $\gamma p \to K^0\Sigma^+$ after background subtractions as a function of c.m. energy W. The uncertainties shown are due only to counting statistics.

There are some published results (CB-ELSA/TAPS [52], SAPHIR [58], and CLAS [56] Collaborations) with which our measurements can be compared. The CB-ELSA/TAPS Collaboration made measurements of $\gamma p \to K^0\Sigma^+$ using a liquid hydrogen target and identified events with the same decay chain as in our analysis:

$$\gamma p \to K^0\Sigma^+ \to (\pi^0\pi^0)(\pi^0 p) \to 6\gamma p. \tag{A.4}$$

On the other hand, the CLAS and SAPHIR Collaborations made measurements of $\gamma p \to K^0\Sigma^+$ using a liquid hydrogen target but identifying the K^0_S by its $K^0_S \to \pi^+\pi^-$

decay mode. For the decay of the Σ^+, both decay modes, $\Sigma^+ \to p\pi^0$ and $\Sigma^+ \to n\pi^+$ were analyzed. Thus their analysis were carried out using two decay chains:

$$\begin{aligned} \gamma p &\to K^0\Sigma^+ \to (\pi^+\pi^-)(\pi^0 p), \\ \gamma p &\to K^0\Sigma^+ \to (\pi^+\pi^-)(\pi^+ n), \end{aligned} \tag{A.5}$$

In addition, measurements of $\gamma p \to K^0\Sigma^+$ on a liquid deuterium target were carried out by Shende (CB-ELSA/TAPS Collaboration) [57]. The reaction chain considered was

$$\gamma d \to K^0\Sigma^+ n \to (\pi^0\pi^0)(\pi^0 pn) \to 6\gamma pn, \tag{A.6}$$

in which the final state consists of six photons, a detected proton, and a neutron.

Figure $A.21$ compares our results for $\sigma_{\rm tot}(\gamma p \to K^0\Sigma^+)$ with those of previous experiments that used both liquid hydrogen and deuterium targets. The previous experiments extended to higher incident photon energies than our experiment. Thus, the plot has a range in the c.m. energy W from 1700 to 2200 MeV. Although the results of these experiments show disagreement with each other, their general trends are similar. Prior measurements obtained with a deuterium target are about 40% lower than those measured with liquid hydrogen targets. Our results are in good agreement with the CB-ELSA measurements obtained with a liquid hydrogen target, although our measurements have slightly smaller values, but also smaller statistical uncertainties.

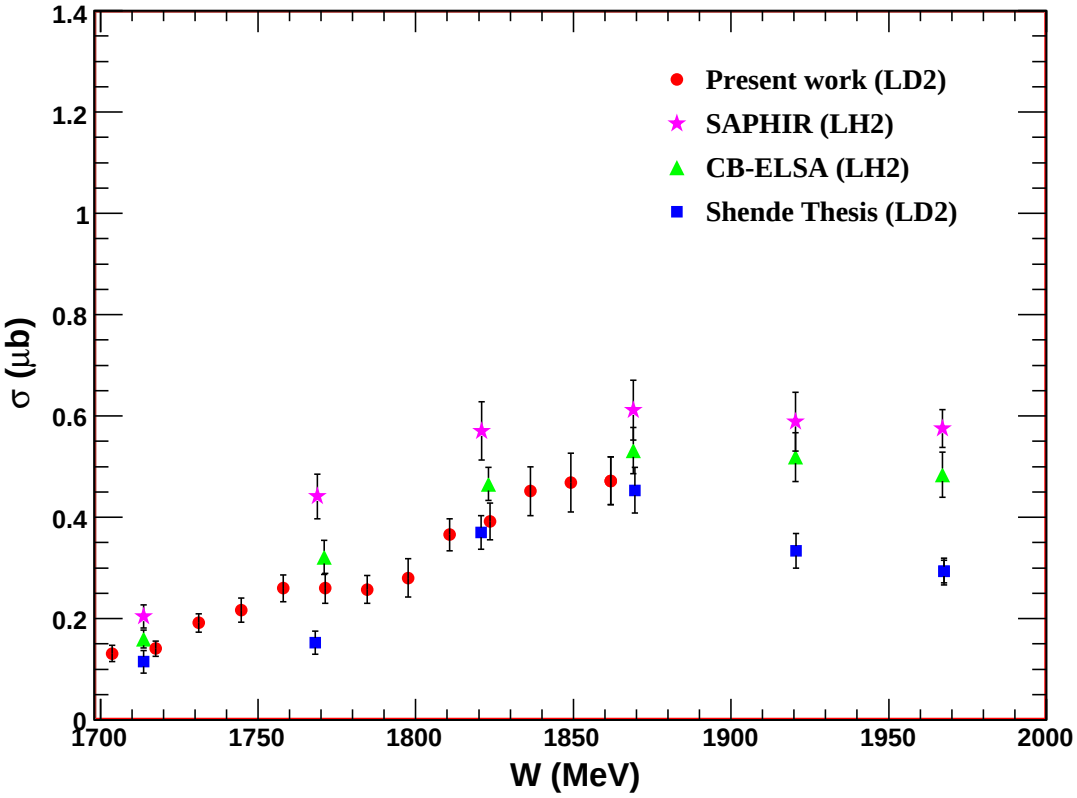

Figure A.21: The total cross section for $\gamma p \to K^0\Sigma^+$ measured after background subtractions in this work (black circles) compared with results of prior experiments. Measurements by the SAPHIR Collaboration [58] using a liquid hydrogen (LH2) target are shown as pink stars, measurements by the CB-ELSA Collaboration [52] using a LH2 target are shown as green triangles, and measurements by Shende (CB-ELSA/TAPS Collaboration) [57] using a liquid deuterium target are shown as blue squares.

Appendix B

Tables of $d\sigma/d\Omega$ and $\sigma_{\rm tot}$ for $\gamma p \to K^0\Sigma^+$

$\cos\theta_{\rm CM}$	E_γ (MeV)			
	1050	1075	1100	1125
-0.9500	0.011 ± 0.007	0.019 ± 0.012	0.011 ± 0.006	0.013 ± 0.006
-0.7125	0.011 ± 0.004	0.014 ± 0.005	0.012 ± 0.004	0.016 ± 0.004
-0.4750	0.006 ± 0.002	0.009 ± 0.003	0.010 ± 0.003	0.013 ± 0.004
-0.2375	0.006 ± 0.003	0.009 ± 0.003	0.006 ± 0.004	0.023 ± 0.004
0.0000	0.010 ± 0.003	0.009 ± 0.002	0.009 ± 0.003	0.017 ± 0.004
$+0.2375$	0.016 ± 0.003	0.010 ± 0.002	0.009 ± 0.003	0.016 ± 0.003
$+0.4750$	0.013 ± 0.003	0.011 ± 0.003	0.017 ± 0.003	0.012 ± 0.003
$+0.7125$	0.012 ± 0.003	0.011 ± 0.003	0.011 ± 0.004	0.016 ± 0.004
$+0.9500$	0.011 ± 0.005	0.017 ± 0.006	0.017 ± 0.005	0.012 ± 0.011

Table B-1: $d\sigma/d\Omega$ for $\gamma p \to K^0\Sigma^+$.

$\cos\theta_{\rm CM}$	E_γ (MeV)			
	1150	1175	1200	1225
-0.9500	0.022 ± 0.009	0.029 ± 0.012	0.007 ± 0.006	0.006 ± 0.004
-0.7125	0.023 ± 0.012	0.023 ± 0.007	0.028 ± 0.011	0.019 ± 0.008
-0.4750	0.014 ± 0.005	0.018 ± 0.007	0.027 ± 0.010	0.027 ± 0.007
-0.2375	0.016 ± 0.005	0.023 ± 0.006	0.023 ± 0.006	0.018 ± 0.006
0.0000	0.019 ± 0.004	0.015 ± 0.003	0.015 ± 0.004	0.016 ± 0.005
$+0.2375$	0.012 ± 0.003	0.014 ± 0.004	0.018 ± 0.005	0.015 ± 0.004
$+0.4750$	0.019 ± 0.004	0.026 ± 0.004	0.017 ± 0.004	0.014 ± 0.004
$+0.7125$	0.016 ± 0.005	0.022 ± 0.005	0.019 ± 0.005	0.023 ± 0.006
$+0.9500$	0.023 ± 0.009	0.018 ± 0.009	0.026 ± 0.008	0.033 ± 0.009

Table B-1: Continued.

$\cos\theta_{\rm CM}$	E_γ (MeV)			
	1250	1275	1300	1325
-0.9500	0.021 ± 0.016	0.027 ± 0.011	0.017 ± 0.017	0.016 ± 0.011
-0.7125	0.014 ± 0.011	0.016 ± 0.006	0.017 ± 0.008	0.021 ± 0.012
-0.4750	0.018 ± 0.007	0.023 ± 0.005	0.025 ± 0.007	0.031 ± 0.010
-0.2375	0.033 ± 0.012	0.018 ± 0.005	0.026 ± 0.007	0.034 ± 0.009
0.0000	0.021 ± 0.005	0.022 ± 0.004	0.034 ± 0.006	0.039 ± 0.008
$+0.2375$	0.018 ± 0.005	0.026 ± 0.005	0.031 ± 0.006	0.036 ± 0.009
$+0.4750$	0.019 ± 0.005	0.031 ± 0.005	0.029 ± 0.006	0.045 ± 0.012
$+0.7125$	0.022 ± 0.008	0.033 ± 0.008	0.030 ± 0.005	0.030 ± 0.007
$+0.9500$	0.029 ± 0.011	0.043 ± 0.001	0.034 ± 0.009	0.021 ± 0.013

Table B-1: Continued.

$\cos\theta_{\mathrm{CM}}$	E_γ (MeV)	
	1350	1375
-0.9500	0.015 ± 0.012	0.022 ± 0.009
-0.7125	0.029 ± 0.019	0.019 ± 0.010
-0.4725	0.031 ± 0.010	0.027 ± 0.008
-0.2375	0.033 ± 0.025	0.031 ± 0.011
0.0000	0.029 ± 0.008	0.039 ± 0.009
$+0.2375$	0.039 ± 0.010	0.039 ± 0.010
$+0.4750$	0.042 ± 0.010	0.038 ± 0.007
$+0.7125$	0.031 ± 0.009	0.034 ± 0.007
$+0.9500$	0.031 ± 0.014	0.015 ± 0.010

Table B-1: Continued.

W (MeV)	$\sigma_{\rm tot}$ $(\mu{\rm b})$
1689.93	0.114 ± 0.013
1703.77	0.131 ± 0.016
1717.50	0.140 ± 0.015
1731.12	0.191 ± 0.018
1744.64	0.227 ± 0.024
1758.08	0.260 ± 0.027
1771.36	0.260 ± 0.029
1784.57	0.257 ± 0.027
1797.69	0.280 ± 0.037
1810.70	0.365 ± 0.031
1823.63	0.391 ± 0.036
1836.47	0.451 ± 0.048
1849.21	0.468 ± 0.058
1861.87	0.472 ± 0.047

Table B-2: Total cross section for $\gamma p \to K^0\Sigma^+$.

Appendix C

Tables of $d\sigma/d\Omega$ and $\sigma_{\rm tot}$ for $\gamma n \to K^0\Lambda$

$\cos\theta_{\rm CM}$	E_γ (MeV)			
	925	950	975	1000
-0.9500	0.052 ± 0.023	0.057 ± 0.022	0.020 ± 0.016	0.060 ± 0.035
-0.7125	0.044 ± 0.014	0.040 ± 0.011	0.064 ± 0.016	0.150 ± 0.019
-0.4750	0.054 ± 0.011	0.061 ± 0.012	0.048 ± 0.011	0.078 ± 0.019
-0.2375	0.034 ± 0.010	0.061 ± 0.012	0.070 ± 0.011	0.089 ± 0.016
0.0000	0.048 ± 0.010	0.040 ± 0.014	0.061 ± 0.017	0.089 ± 0.017
$+0.2375$	0.057 ± 0.018	0.059 ± 0.012	0.081 ± 0.016	0.067 ± 0.018
$+0.4750$	0.048 ± 0.016	0.091 ± 0.014	0.064 ± 0.022	0.147 ± 0.026
$+0.7125$	0.073 ± 0.020	0.062 ± 0.016	0.070 ± 0.002	0.108 ± 0.025
$+0.9500$	0.112 ± 0.031	0.005 ± 0.023	0.133 ± 0.076	0.057 ± 0.042

Table C-1: $d\sigma/d\Omega$ for $\gamma n \to K^0\Lambda$.

$\cos\theta_{\mathrm{CM}}$	E_γ (MeV)			
	1025	1050	1075	1100
-0.9500	0.133 ± 0.039	0.139 ± 0.053	0.012 ± 0.064	0.108 ± 0.042
-0.7125	0.161 ± 0.037	0.207 ± 0.030	0.106 ± 0.024	0.144 ± 0.028
-0.4750	0.177 ± 0.035	0.173 ± 0.029	0.206 ± 0.026	0.107 ± 0.045
-0.2375	0.172 ± 0.036	0.127 ± 0.035	0.176 ± 0.027	0.192 ± 0.061
0.0000	0.153 ± 0.029	0.148 ± 0.023	0.213 ± 0.044	0.200 ± 0.038
$+0.2375$	0.112 ± 0.024	0.143 ± 0.027	0.024 ± 0.029	0.021 ± 0.039
$+0.4750$	0.096 ± 0.022	0.150 ± 0.032	0.153 ± 0.035	0.162 ± 0.043
$+0.7125$	0.129 ± 0.029	0.190 ± 0.035	0.099 ± 0.047	0.119 ± 0.077
$+0.9500$	0.019 ± 0.064	0.085 ± 0.043	0.135 ± 0.049	0.108 ± 0.035

Table C-1: Continued.

$\cos\theta_{\mathrm{CM}}$	E_γ (MeV)			
	1125	1150	1175	1200
-0.9500	0.141 ± 0.046	0.157 ± 0.019	0.130 ± 0.051	0.151 ± 0.047
-0.7125	0.199 ± 0.033	0.157 ± 0.034	0.246 ± 0.042	0.193 ± 0.034
-0.4750	0.125 ± 0.040	0.172 ± 0.034	0.258 ± 0.032	0.206 ± 0.045
-0.2375	0.220 ± 0.032	0.248 ± 0.043	0.204 ± 0.065	0.214 ± 0.043
0.0000	0.225 ± 0.029	0.195 ± 0.031	0.238 ± 0.033	0.237 ± 0.038
$+0.2375$	0.163 ± 0.030	0.243 ± 0.033	0.183 ± 0.036	0.214 ± 0.055
$+0.4750$	0.163 ± 0.034	0.238 ± 0.039	0.142 ± 0.046	0.152 ± 0.042
$+0.7125$	0.113 ± 0.040	0.192 ± 0.039	0.153 ± 0.050	0.139 ± 0.067
$+0.9500$	0.061 ± 0.047	0.091 ± 0.054	0.011 ± 0.047	0.112 ± 0.045

Table C-1: Continued.

$\cos\theta_{\rm CM}$	E_γ (MeV)			
	1225	1250	1275	1300
-0.9500	0.010 ± 0.040	0.033 ± 0.015	0.146 ± 0.037	0.137 ± 0.055
-0.7125	0.216 ± 0.046	0.143 ± 0.038	0.189 ± 0.044	0.144 ± 0.048
-0.4750	0.218 ± 0.035	0.215 ± 0.042	0.200 ± 0.035	0.219 ± 0.046
-0.2375	0.253 ± 0.046	0.224 ± 0.049	0.236 ± 0.041	0.185 ± 0.055
0.0000	0.230 ± 0.049	0.066 ± 0.060	0.182 ± 0.039	0.186 ± 0.048
$+0.2375$	0.224 ± 0.046	0.151 ± 0.029	0.155 ± 0.035	0.116 ± 0.011
$+0.4750$	0.177 ± 0.064	0.139 ± 0.068	0.103 ± 0.033	0.186 ± 0.067
$+0.7125$	0.109 ± 0.039	0.179 ± 0.038	0.160 ± 0.068	0.177 ± 0.051
$+0.9500$	0.017 ± 0.056	0.120 ± 0.051	0.185 ± 0.066	0.032 ± 0.047

Table C-1: Continued.

$\cos\theta_{\mathrm{CM}}$	E_γ (MeV)		
	1325	1350	1375
-0.9500	0.103 ± 0.057	0.169 ± 0.053	0.112 ± 0.050
-0.7125	0.208 ± 0.048	0.238 ± 0.069	0.171 ± 0.063
-0.4750	0.234 ± 0.120	0.249 ± 0.077	0.218 ± 0.054
-0.2375	0.250 ± 0.054	0.274 ± 0.065	0.252 ± 0.044
0.0000	0.177 ± 0.084	0.216 ± 0.063	0.221 ± 0.044
$+0.2375$	0.163 ± 0.079	0.133 ± 0.073	0.227 ± 0.058
$+0.4750$	0.125 ± 0.077	0.086 ± 0.070	0.148 ± 0.100
$+0.7125$	0.137 ± 0.067	0.124 ± 0.038	0.114 ± 0.064
$+0.9500$	0.082 ± 0.085	0.069 ± 0.078	0.053 ± 0.054

Table C-1: Continued.

W (MeV)	$\sigma_{\rm tot}$ $(\mu{\rm b})$
1618.94	0.52 ± 0.05
1633.38	0.53 ± 0.04
1647.70	0.65 ± 0.07
1661.89	0.93 ± 0.08
1675.97	1.37 ± 0.11
1689.93	1.74 ± 0.12
1703.77	1.77 ± 0.13
1717.50	1.84 ± 0.17
1731.12	1.97 ± 0.14
1744.64	2.24 ± 0.15
1758.08	2.36 ± 0.17
1771.36	2.38 ± 0.20
1784.57	2.29 ± 0.19
1797.69	2.12 ± 0.19
1810.70	2.27 ± 0.20
1823.63	2.42 ± 0.28
1836.47	2.57 ± 0.35
1849.21	2.79 ± 0.32
1861.87	2.75 ± 0.32

Table C-2: Total cross section for $\gamma n \to K^0\Lambda$.

Appendix D

Legendre fitting coefficients for $\gamma p \to K^0\Sigma^+$

A_n	E_γ (MeV)			
	1050	1075	1100	1125
A_0	0.009 ± 0.001	0.010 ± 0.001	0.011 ± 0.001	0.015 ± 0.001
A_1				
A_2				
	1150	1175	1200	1225
A_0	0.017 ± 0.002	0.020 ± 0.002	0.021 ± 0.002	0.020 ± 0.002
A_1	-0.000 ± 0.003	-0.000 ± 0.004	-0.003 ± 0.005	0.004 ± 0.005
A_2	0.003 ± 0.003	0.005 ± 0.003	0.005 ± 0.004	0.006 ± 0.005

Table D-1: Legendre coefficients for $\gamma p \to K^0\Sigma^+$.

A_n	E_γ (MeV)			
	1250	1275	1300	1325
A_0	0.022 ± 0.003	0.029 ± 0.002	0.031 ± 0.003	0.036 ± 0.004
A_1	0.002 ± 0.006	0.009 ± 0.004	0.009 ± 0.005	0.005 ± 0.006
A_2	0.003 ± 0.007	0.005 ± 0.003	-0.004 ± 0.005	-0.012 ± 0.007
	1350	1375		
A_0	0.037 ± 0.004	0.038 ± 0.004		
A_1	0.008 ± 0.008	0.005 ± 0.006		
A_2	-0.008 ± 0.008	-0.016 ± 0.008		

Table D-1: Continued.

Appendix E

Legendre fitting coefficients for $\gamma n \to K^0\Lambda$

A_n	E_γ (MeV)			
	925	950	975	1000
A_0	0.042 ± 0.004	0.042 ± 0.003	0.052 ± 0.005	0.074 ± 0.006
A_1				
A_2				
	1025	1050	1075	1100
A_0	0.109 ± 0.009	0.138 ± 0.009	0.141 ± 0.010	0.146 ± 0.013
A_1	-0.052 ± 0.015	-0.023 ± 0.018	-0.019 ± 0.019	0.005 ± 0.019
A_2	-0.043 ± 0.018	0.004 ± 0.021	-0.099 ± 0.029	-0.058 ± 0.024

Table E-1: Legendre coefficients for $\gamma n \to K^0\Lambda$.

A_n	E_γ (MeV)			
	1125	1150	1175	1200
A_0	0.157 ± 0.011	0.178 ± 0.012	0.188 ± 0.014	0.189 ± 0.016
A_1	-0.041 ± 0.021	0.043 ± 0.012	-0.079 ± 0.025	-0.031 ± 0.026
A_2	-0.069 ± 0.027	-0.122 ± 0.025	-0.097 ± 0.030	-0.069 ± 0.031
	1225	1250	1275	1300
A_0	0.182 ± 0.015	0.169 ± 0.015	0.181 ± 0.016	0.193 ± 0.022
A_1	-0.176 ± 0.027	-0.088 ± 0.027	-0.085 ± 0.037	-0.103 ± 0.037
A_2	-0.030 ± 0.022	0.012 ± 0.024	-0.080 ± 0.030	-0.025 ± 0.034
	1325	1350	1375	
A_0	0.205 ± 0.028	0.223 ± 0.026	0.218 ± 0.025	
A_1	-0.104 ± 0.056	-0.079 ± 0.049	-0.139 ± 0.045	
A_2	-0.062 ± 0.047	-0.107 ± 0.043	-0.053 ± 0.043	

Table E-1: Continued.

Appendix F

Background contributions to $\sigma_{\rm tot}(\gamma p \to K^0\Sigma^+)$

W (MeV)	Contribution (%)
1689.93	39.3 ± 5.1
1703.77	35.2 ± 4.9
1717.50	32.9 ± 4.1
1731.12	32.9 ± 3.8
1744.64	35.1 ± 4.3
1758.08	32.4 ± 3.8
1771.36	34.2 ± 5.4
1784.57	40.6 ± 4.5
1797.69	33.3 ± 4.8
1810.70	36.3 ± 3.4
1823.63	43.9 ± 4.2
1836.47	29.4 ± 4.4
1849.21	33.7 ± 5.1
1861.87	37.5 ± 4.2

Table F-1: Total contribution to $\sigma_{\rm tot}(\gamma p \to K^0\Sigma^+)$ from different background reactions and the empty target.

Appendix G

Background contributions to $\sigma_{\rm tot}(\gamma n \to K^0\Lambda)$

W (MeV)	Contributions (%)
1618.94	7.5 ± 0.9
1633.38	6.3 ± 0.8
1647.70	5.5 ± 0.9
1661.89	5.2 ± 0.7
1675.97	7.2 ± 0.8
1689.93	7.1 ± 0.5
1703.77	10.5 ± 0.9
1717.50	11.4 ± 1.3
1731.12	14.9 ± 1.2
1744.64	13.9 ± 1.1
1758.08	14.4 ± 1.3
1771.36	13.4 ± 1.4
1784.57	13.3 ± 1.4
1797.69	13.6 ± 1.4
1810.70	15.9 ± 1.6
1823.63	16.9 ± 2.2
1836.47	16.3 ± 2.8
1849.21	15.6 ± 3.7
1861.87	17.6 ± 2.3

Table G-1: Total contribution to $\sigma_{\rm tot}(\gamma n \to K^0\Lambda)$ from different background reactions and the empty target.